Localization and tracking of high-speed trains using compressed sensing based 5G localization algorithms

by

Meet Ameet Trivedi

Submitted in partial fulfillment of the requirements for the degree
Master of Engineering (Electronic Engineering)

in the

Department of Electrical, Electronic and Computer Engineering
Faculty of Engineering, Built Environment and Information Technology

UNIVERSITY OF PRETORIA

October 2021

SUMMARY

LOCALIZATION AND TRACKING OF HIGH-SPEED TRAINS USING COMPRESSED SENSING BASED 5G LOCALIZATION ALGORITHMS

by

Meet Ameet Trivedi

Supervisor:	Dr. J.H. van Wyk
Department:	Electrical, Electronic and Computer Engineering
University:	University of Pretoria
Degree:	Master of Engineering (Electronic Engineering)
Keywords:	5G, Compressed sensing, Distributed compressed sensing - simultaneous orthogonal matching pursuit, Extended Kalman filter, high-speed trains, line-of-sight tracking, localization, tracking

The fifth-generation (5G) cellular standard is set to contain several disruptive technologies. These technologies will enable accurate localization of Mobile Terminals (MT) and mobile Machine Type Communication (mMTC) devices in 5G networks. An application of this high-accuracy-localization capability in 5G networks, is the localization of High-Speed Trains (HST). Current state-of-the-art HST localization systems fuse readings from several sensors, such as RF tags on track, Doppler radar, accelerometers, gyroscopes, magnetometers, and Global Navigation Satellite System (GNSS) receiver data, which are further combined with digital track data. Although the localization algorithm using multiple sources of information, it performs poorly in urban and forest environments when the GNSS signal is obstructed and digital map data is not available. Thus, an alternative solution for this problem is required and 5G localization was identified as a possible solution.

In this dissertation the author proposes a novel way for making use of compressed sensing based 5G localization algorithms for the localization and tracking of HSTs. Compressed sensing based 5G localization algorithms decompose the received signal into its angular components in beamspace using the Distributed Compressed Sensing - Simultaneous Orthogonal Matching Pursuit (DCS-SOMP)

algorithm. The decomposed components in the beamspace domain can thereafter be used to accurately determine the MT location. For the HST scenario, where a LOS path between the train and track-side antennas is always available, this algorithm can be simplified by incorporating tracking data in the initial beamspace that is searched by the DCS-SOMP algorithm. This ensures that the first component found by the algorithm is the LOS component and it increases the estimation accuracy of the channel parameters for the LOS component.

The proposed algorithm was tested in two different scenarios. The first is a straight track scenario and the second is a part of a real-life track between Shanghai and Beijing using data from OpenStreetMaps (OSM) with the map points joined using cubic Bezier curves. The algorithm achieves sub-meter accuracy on the straight track scenario using just one Remote Radio Head (RRH). For the map trajectory generated using cubic Bezier curves, an accuracy of 1.05 m is achieved with a 99% availability using only one RRH, and sub-meter accuracy is achieved when using two RRH. The performance requirements set out by 3GPP for the use case of machine control and intelligent transportation are met with just one RRH. These results indicate that LOS tracking provides an improvement in performance in comparison to the original algorithm (without LOS tracking) proposed in literature. Furthermore, the performance observed in simulations is better than the performance of existing 5G localization-based HST tracking solutions and also meets the performance requirements set by the 3GPP for the use case of machine control and transportation.

LIST OF ABBREVIATIONS

1G	First generation
3G	Third Generation
3GPP	Third Generation Partnership Project
4G	Fourth Generation
5G	Fifth Generation
AOA	Angle-of-Arrival
AOD	Angle-of-Departure
AWGN	Additive White Gaussian Noise
BS	base station
BP	Belief Propagation
CLP	collaborative localization protocol
CRB	Cramér-Rao bound
CSI	channel state information
D2D	device-to-device
DCS-SOMP	Distributed Compressed Sensing - Simultaneous Orthogonal Matching Pursuit
DFT	Discrete Fourier Transform
DiSoul	Direct Source Localization
DOA	Direction of Arrival
DOD	Direction of Departure
ECGL	Enhanced Cooperative Group Localization
ECS	Eddy Current Sensors
EKF	Extended-Kalman-Filter
ELM	extreme learning machine
EHHT	Enhanced hybrid hypothesis test
FDOA	Frequency-difference-of-Arrival
FFT	Fast Fourier Transform
GNSS	Global Navigation Satellite System
GSM	Global System for Mobile Communication
HMM	Hidden Markov Model
HST	high speed train

LOB	line of bearing
LTE	Long Term Evolution
MT	mobile terminal
M2M	machine-to-machine
ML	maximum-likelihood-type
mMTC	mobile Machine Type Communication
mmWave	millimetre-wave
MIMO	multiple-input and multiple-output
NUMD	New Radio user equipment measurement data
OFDM	Orthogonal Frequency Division Multiplexing
OLOS	obstructed-line-of-sight
RF	Radio Frequency
RCC	Received Signal Strength
RLP	round-trip localization protocol
SDR	Software Defined Radio
SLAB	successive localization and beamforming
SLAM	simultaneous localization and mapping
TDOA	Time-Difference-of-Arrival
TOA	Time-of-Arrival
UL	uplink
ULA	Uniform Linear Array

TABLE OF CONTENTS

LIST OF FIGURES

CHAPTER 1 INTRODUCTION

1.1 PROBLEM STATEMENT

1.1.1 Context of the problem

In railways, complex systems are in place in order to allow for the safe management of trains. These systems ensure that trains are at the right place at the right time, and the available resources are used to maximize capacity, while preventing collisions between trains. This system includes a huge variety of sensors and actuators that work together to track and control trains. In state-of-the-art systems, the tracking of High-Speed Train (HST) is implemented using Radio Frequency (RF) tags installed on the track roughly 1 km apart. These measurements are paired with wheel angular speed sensor measurements to achieve a tracking accuracy of $\pm$(5 m + 5% of the distance travelled from the last RF tag [1]). The accuracy can be increased by fusing the readings from other sensors, such as the Doppler radar, accelerometers, gyroscopes and magnetometers [1]. These sensors are still prone to accumulation of error over time. Thus, the absolute positioning of the train is obtained using a Global Navigation Satellite System (GNSS) receiver. The accuracy of the GNSS receiver degrades in urban and forest environments due to multipath propagation and high signal attenuation of the signal between the receiver and the satellite. Regardless, the GNSS further increases the accuracy of the position estimate. Owing to the fact that the motion of the train is constrained to the track, the accuracy is further improved by incorporating track data through digital maps. After combining all this information, an accuracy (standard deviation of the estimation error) of 0.8-1.3 m is achieved. This degrades to 1.8 m when GNSS signal is obstructed and digital map data is not available [1]. Thus, a simple alternative method that can reliably and accurately estimate the HST location is required.

In addition to railway safety, the knowledge of the accurate location and velocity of a HST is critical for other applications as well. The fifth generation (5G) New Radio network operates in the mmWave

band and signals in the mmWave band encounter high atmospheric attenuation. Thus, location based beamforming is required to compensate for this high signal attenuation. Knowing the accurate location of the HST can have significant effect on the SNR attained by users on-board the train. Additionally, knowledge of the velocity of the train is also required for Doppler precompensation, to allow for better synchronization between the receiver and the transmitter.

1.1.2 Research gap

A simple yet more accurate alternative for the localization problem is the use of 5G localization services. As the 5G standard allows operation in the mmWave band, a large bandwidth is available and many antennas can be grouped together in a small space to allow for massive Multiple-Input Multiple-Output (massive-MIMO). These disruptive technologies combine to allow for 5G localization algorithms to achieve up to sub-meter localization accuracy. This capability of localizing a high-speed train using 5G infrastructure has been studied in [2–5]. It has been shown that localization using 5G infrastructure can achieve localization accuracy high enough for use in intelligent transportation. However, these studies have considered only two different localization algorithm; a Time Difference of Arrival (TDOA) based localization algorithm and a Time-of-Arrival (TOA) and Angle of Departure (AOD) based localization algorithm. While these localization technique take advantage of the large bandwidth available in 5G and massive-MIMO, there are a multitude of different localization techniques that take advantage of other disruptive technologies present in the 5G standardization.

One of the best performing algorithm for localization using 5G infrastructure is the compressed sensing based localization algorithm presented in [6–8]. This algorithm takes advantage of the fact that the mmWave channel is approximately sparse in the beamspace domain. Thus, the received signal can be decomposed in its angular components using the Distributed Compressed Sensing - Simultaneous Orthogonal Matching Pursuit (DCS-SOMP) algorithm. The decomposed components in the beamspace domain can thereafter be used to accurately determine the mobile terminal (MT) location. What makes this algorithm really attractive is the fact that it can obtain a very accurate estimate of the MT position in low SNR conditions. Sub-meter localization accuracy is achievable at SNR values as low as -20 dB. Furthermore, the localization estimate only requires the MT to be connected to one base-station (BS). This is desirable, since the mmWave band signals suffer from high attenuation. Thus, a reliable connection to multiple BS can be an impractical requirement. While this localization method has been studied in literature, it has not been applied to the problem of localization and tracking of high-speed trains.

1.2 RESEARCH OBJECTIVE AND QUESTIONS

This research project intends to investigate a compressed sensing based 5G localization algorithm, referred to as the DCS-SOMP algorithm, for the application of localization and tracking of HSTs. The primary objective is to design a localization algorithm that can achieve sub-meter localization accuracy and meet the standards set by 3GPP for the use case of machine control and intelligent transportation. The algorithm should also provides some improvement in performance compared to existing HST localization solutions. The secondary objective is to determine how the localization performance is affected by various different algorithm parameters.

The research questions are therefore:

- Can the proposed algorithm localize and track a HST with sub-meter localization accuracy?
- Can the proposed algorithm meet the performance requirements set by the 3GPP for the use case of machine control and intelligent transportation?
- Can the proposed algorithm perform better than the existing solutions for localization and tracking of a HST?
- How do the various algorithm parameters (number of Remote Radio Head (RRH) units used, number of antennas at the transmitter, number of antenna at the receiver, number of symbols used, number of carriers used, the localization interval and the tracking parameters) affect the performance of the algorithm?
- What are the minimum parameter values for which the algorithm can achieve satisfactory performance?

1.3 APPROACH

In order to answer the research questions, the HST tracking system using the proposed localization needs to be implemented, and the localization accuracy over a test trajectory needs to be verified, for various simulation settings. However, to actually design a train tracking system using the proposed localization method will have several challenges besides localization, such as finding the true exact location of the train. Thus, in order to limit the scope of the research to only answering the research questions, and taking into account the fact that a high-speed train is not readily available, the proposed system will be implemented in a simulation environment.

Several different simulation environments can be used to simulate the system such as Python, Matlab or C++. Python was chosen as the environment in which system simulations were performed. This is due to the fact that there are no special requirements for the simulation environment besides ease of use. This makes Python the better choice compared to Matlab and C++.

The research procedure is described as follows:

1. The compressed sensing based localization algorithm presented in [6–8] and the EKF based tracking presented in [2–5] will initially be studied thoroughly and understood.
2. These algorithms will thereafter be implemented in Python.
3. The implemented algorithm will be applied to localize a HST on a chosen simulated trajectory. The simulation scenario will be set up according to the the mmWave HST deployment scenario described by the 3GPP in [9]. An appropriate channel model based on this scenario will be used in system simulation. Furthermore, similar to existing studies the transmitter and receiver parameters (such as carrier frequency, bandwidth, etc.) used in simulation will be based on the 3GPP specified parameters for 5G deployment in the mmWave band [9].
4. From the simulation a set of actual and predicted states of the train throughout its simulated trajectory will be obtained. These will be subtracted from each other to obtain the Cumulative Distribution Function (CDF) of the estimation error.
5. Based on the obtained CDF of the estimation error for various simulation scenarios, the research questions will be answered.

1.4 RESEARCH GOALS

The primary goals of this research project are the following:

- To develop an algorithm that can accurately and reliably localize and track a HST.
- To develop an algorithm that is better than the existing methods for localization and tracking of HSTs.
- To determine how the performance of the algorithm is affected by various system parameters.
- To ensure that the number of resources, such as transmit antennas, receive antennas, carriers and symbols used by the algorithm, are minimal.

1.5 RESEARCH CONTRIBUTION

The research conducted here has two main contributions. Firstly, a contribution is made to the field of localization and tracking of HSTs, whereby a method that makes use of a compressed sensing based 5G localization algorithm, that has not been previously applied to the problem of localization and tracking of HSTs, is proposed. Secondly, a contribution is made to the field of 5G localization through compressed sensing. A novel method for incorporating tracking data into the localization algorithm, in order to simplify the algorithm and ensure that an accurate estimate of the Mobile Terminal (MT) being localized is found, is proposed. Besides the HST scenario, this method can be used for other scenarios where there is a high probability of the line-of-sight (LOS) path being available such as in ultra dense 5G networks.

1.6 RESEARCH OUTPUTS

The research conducted produced two articles. Firstly the following conference paper:

- M. A. Trivedi and J. H. van Wyk, "Localization and Tracking of High-Speed Trains Using Compressed Sensing Based 5G Localization Algorithms," in *Proc. IEEE 24th International Conference on Information Fusion (FUSION2021)*, Sun City, Rustenburg, North West Province, South Africa, 1-4 Nov 2021, pp. 1-7.

Secondly the following journal article currently in review:

- M. A. Trivedi and J. H. van Wyk, "Localization of high-speed trains using 5G localization algorithms through LOS tracking," in *IEEE Access* (under review), September 2021, pp. 1-12.

1.7 OVERVIEW OF STUDY

Chapter 2 provides a summary of the existing literature in fields of localization and tracking of HSTs and 5G localization. The state-of-the-art HST localization and tracking solutions proposed in literature, are discussed. Next the fundamentals of radio localization using telecommunications infrastructure are discussed. The various methods proposed in literature for localization using 5G infrastructure are discussed in the next section. Furthermore, studies in which 5G localization algorithms are applied to a problem such as tracking of HSTs, are also discussed.

In Chapter 3, the compressed sensing based 5G localization using the DCS-SOMP algorithm is discussed. The system model assumed by the localization algorithm is discussed first. The DCS-SOMP algorithm as proposed in [6–8] for localizing a stationery MT is discussed next - with emphasis on the performance achievable by the algorithm. This is followed by a discussion on the modified version of this algorithm to allow for more reliable and accurate localization. Here the proposed algorithm is compared to the original algorithm to ensure that desired improvement is achieved. At the end, the proposed algorithm is tested for various parameter values to determine how the performance is affected by each parameter.

Tracking the HST using the Extended Kalman Filter (EKF) is discussed in Chapter 4. The theory behind the EKF is discussed first, followed by the specifics of its implementation in the HST scenario.

The complete localization and tracking algorithm proposed for tracking a HST is discussed in Chapter 5. The way the localization and tracking algorithms interact with each other is discussed first. This is followed by a description of how the measurement limits for LOS tracking, beamforming and outlier detection are obtained.

In Chapter 6, the experimental setup is discussed. This consists of a discussion on the system model used in simulation, followed by a discussion on the channel model used in simulation. Finally, the parameters used in different simulation scenarios are discussed.

The results obtained from running the algorithm in the simulation scenarios (discussed in Chapter 6) are presented and discussed in Chapter 7. The estimation accuracy of the proposed algorithm is compared to the original algorithm for a straight track scenario and a real-life HST track scenario for various values of RRHs used for localization. This is followed by a series of simulations in which the parameters of the EKF and the localization algorithm are varied to investigate their effect on estimation performance. At the end, the algorithm is simulated with the lowest parameters values that are expected to achieve satisfactory performance.

Chapter 8 provides a summary of the work presented throughout the dissertation and recommendations for future work. Finally, Addendum A serves to define the method used to generate control points for the cubic Bezier curves used to model the real-life HST track.

CHAPTER 2 LITERATURE STUDY

2.1 INTRODUCTION

This chapter presents a summary of the existing literature in localization and tracking of HSTs and the current methods for 5G localization. In Section 2.2, the current state-of-the-art HST localization algorithms and the various algorithms proposed in literature for use in localization and tracking for HSTs are provided. This is followed by Section 2.3, where the fundamentals of localization using telecommunication infrastructure are discussed. Next, in Section 2.4, the various methods currently documented in literature for performing localization using 5G infrastructure are explored with emphasis on the performance achieved by each algorithm. Various different areas where 5G localization is applied to, are provided in Section 2.5. Lastly in Section 2.6, concluding remarks are made.

2.2 LOCALIZATION AND TRACKING OF HSTS

The architecture of a typical high-speed train localization system can be seen in Fig. 2.1. Firstly multiple sensors are used to measure the train state. The output of these sensors is thereafter combined and filtered using a sequential Bayesian filter. Some systems take advantage of the train's motion being constrained to the train track and also integrate map data in the sequential Bayesian filter, when digital maps are available. Lastly, the filtered estimate for the train's state is provided to the train control system for use in automation. Some systems also make use for this filtered state estimate of the train to update the digital track maps.

The current method for localization of HSTs specified by the European train control system (ETCS) uses a combination of radio frequency (RF) balises and odometer measurements. The balises are installed on the track at approximately every 1 km and provide the absolute location of the train. In between the balises odometer measurements are used for localization. Odometer measurements are

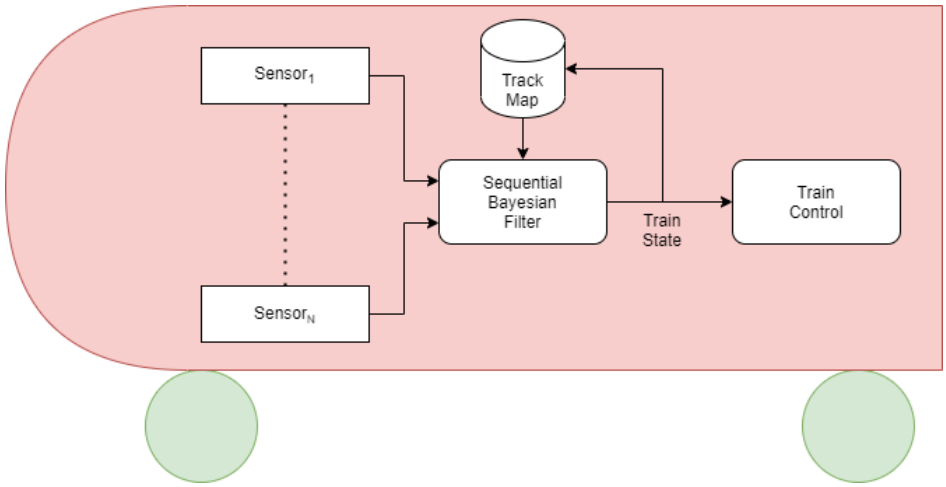

Figure 2.1. The architecture of a typical HST localization system.

based on wheel angular speed measurements which degrade due to wheel slippage. The resulting system can obtain ±(5 m + 5% of the distance from the last balise) [1]. Additional onboard sensors measurements such as accelometers, magnetometers, gyroscopes and Doppler radar can be used to further improve localization performance. Furthermore, measurements from the global navigation satellite systems (GNSS) receiver can also used. However, GNSS requires multiple satellites to be in line-of-sight (LOS) of the receiver; thus, the performance degrades in urban and forest areas. A prototype of the InteGRail system which makes use of balises, odometer and GNSS can achieve an accuracy (standard deviation of estimation error) between 0.8-1.3 m which further degrades to 1.8 m in non-ideal conditions (not enough satellites in LOS and/or unavailability of map data) [10].

Various different implementations of this system have been proposed in literature. Majority of these studies propose new types of sensors that can be used, while others propose different filtering techniques to be used. In [11], a specific GNSS system referred to as the BeiDou navigation satellite system (BDS) is used with inertial navigation system (INS), odometer and map matching. Similar to GNSS, BDS also suffers from outages. When the outages occur, the BDS measurements are simply omitted the rest of the sensors are used with map matching. Furthermore, the algorithm uses Federated Kalman filter (FKF) to filter the measurements. The proposed system shows an improvement in localization accuracy in comparison to balise and odometer based localization methods.

A general Bayesian filter for the localization and tracking of HST is derived in [12]. The method analyzes various causal dependencies in the HST tracking problem and takes into account the kinematic

restrictions forced by the train track. The particle filter implementation of the resulting Bayesian filter that tracks the train directly on the known topological track map instead of using map matching is also proposed. This idea is extended further in [13], incorporating 3D geometric measurements of the rail track from inertial sensors into the localization algorithms. Additionally in [14], a Rao-Blackwellized particle filter (RBPF) implementation of the Bayesian filter is proposed. The proposed algorithm achieves correct track selectivity 99.3% times for parallel track scenarios and it can correctly resolve switch ways 97.2% of the time in simulation.

A similar particle filter based approach is also applied in [15, 16]. However, [15] only uses measurements from Eddy Current Sensors (ECS) for localization, while in [16] magnetometer measurements are used. ECSs provide precise measurements for the speed of the HST that are unaffected by wheel slippage. Furthermore, ECS readings can also be used to uniquely identify the railroad switches in the network that the train is passing over and which track the train takes at the switch. Therefore, the proposed algorithm in [15] initially does speed estimation, followed by turnout classification using hidden Markov models (HMMs). At the end, a particle filter is used to combine the measurements and localize the train on the map. The proposed algorithm is proven to be capable of providing reliable localization in real time. The magnetometer on the other hand, takes measurements of the Earth's magnetic field. The large amount of ferromagnetic infrastructure in rail lines distorts the Earth's magnetic field. As these distortions are unique to different parts of the rail network, magnetometer measurements can be used to localize the train in the network. Thus, in [16], a prior map of magnetometer measurements taken at various locations throughout the rail network is used in combination with a particle filter to localize the train. The localization performance of this algorithm is not very good. However, in combination with additional measurements from other sensors the performance can be improved.

The probabilistic Bayesian localization approach used in previous studies is also used in [17]. However, an alternate Kalman filter based implementation is proposed. The focus is on interpreting the train location probabilities through statistical tests to ensure safe operation of the trains. Additionally, the idea of virtual balises is proposed. Virtual balises are points on the track map and when the train passes over these points the train control system is notified. The statistical tests used for train safety are also used to determine if the train has passed over a virtual balise. The proposed algorithm works well even in a parallel track scenario.

On the other hand in [18, 19], a Simultaneous localization and mapping (SLAM) algorithm is proposed. A particle filter based SLAM algorithm, referred to as RailSLAM is proposed in [18]. This algorithm builds on the RBPF implementation discussed previously from [14]. A probabilistic map consisting of equally spaced points over the train track is generated with intermediate points on the map being generated through linear interpolation. A simpler Kalman Filter based SLAM algorithm is proposed in [19]. Similar to [18], probabilistic maps are generated; however, here cubic splines are used to interpolate between generated track points. Both these methods have shown to be able to localize trains effectively with [19] showing an improvement in localization performance after every iteration as the map generated becomes more accurate. However, both these studies assume that it is already known which route the train is on and track selection is not considered.

Several localization algorithms have been proposed for localization of trains in specific scenarios such as tunnels and turnouts [20, 21]. In [20] a lidar based localization and mapping method is proposed for localization in underground tunnels. The algorithm initially uses lidar and odometer readings to creates a reference map of the tunnel. Once the reference map is created, localization is performed through matching the subsequent lidar scans and odometer readings to the generated map. The turnout detection algorithm proposed in [21] uses a monofocal camera with a digital map. The train tracks in the field of view of the camera are approximated using probabilistic spline curves. The curves are recursively estimated in each frame and used in combination with the map to determine which track is taken at the switch way. Both [20] and [21] shown to work in certain scenarios. However, additional work is needed to improve the reliability of these algorithms. Furthermore, these algorithms have to be paired with other sensor measurements in order to have a complete localization solution.

2.3 BASICS OF RADIOLOCATION USING TELECOMMUNICATION INFRASTRUCTURE

Radiolocation refers to the operation of localizing an object by using radio waves. This primarily refers to passive localization such as radar but here it used to refer to active localization of devices, more specifically Mobile Terminals (MT) in a telecommunications network. Typically the localization of a device is performed using GNSS. As mentioned previously, for the GNSS systems to localize with reasonable accuracy, it is required that enough satellites are in LOS of the GNSS receivers being localized. The performance of the GNSS systems therefore degrades in urban areas and indoor areas. Therefore, an alternate ground based localization method for RF devices is essential.

Cellular network infrastructure is deployed around the world and is optimized for communication; however, the infrastructure also provides a way for performing radio localization. There has been significant research from the first generation (1G) to the future fifth generation (5G) standards to make use of the existing telecommunication infrastructure for localization. When Third Generation (3G) was being deployed, the Third Generation Partnership Project (3GPP) was created, followed by the 3GPP2. Both of these bodies considered various localization methods in the standardization process with the main objective being to support emergency services. Even during the standardization of Fourth Generation (4G) Long Term Evolution (LTE) positioning services were considered. The support for positioning services is expected to further grow in the 5G standardization [22].

A key driver in the development of localization using telecommunication infrastructure is emergency services. However, it has several other applications. Firstly, location based services such as navigation, mapping, geo-marketing and advertising, asset tracking, social networking, augmented reality and location-sensitive billing. Localization of MTs will also make way for location-aware communication, network optimizations that take into account the location of the MT. Location-aware communication includes location based beamforming to combat the high atmospheric attenuation present at high frequencies used in 5G. This further allows for other optimizations such as frequency reusablity based on the the location of user and optimal hopping between Base Stations (BS) [22].

Many different algorithms have been proposed for radiolocation, each of these algorithms can be classified in one of more of the groups discussed in the sub-sections to follow [23].

2.3.1 Centralized or Distributed

In centralized localization the signal measurements taken by the MTs are transmitted back to the base station and fused together to obtain the user location. In distributed localization on the other hand each of the MT calculates its own location based on the measurements on nearby MTs and their locations [23]. Distributed localization algorithms are useful for large networks with limited number of BSs and they provide some tolerance against node failure. The price that is paid for these advantages is the sub-optimal localization accuracy and also longer processing time as information has to be exchanged iteratively until the algorithm converges to the MT location [24].

2.3.2 Cooperative or Non-Cooperative

Non-cooperative localization algorithms are algorithms where signal measurements are obtained only at the BSs or the MT when localizing the MT, meaning that multiple BSs are required to perform

localization. While cooperative localization algorithms calculate the user location by the measurement between the MT, BS and other MTs through Device-to-Device (D2D) communication. This means that each MT does not need to be connected to multiple BSs. Furthermore, for MTs that are far from the BS can improve the localization performance by incorporating measurements from nearby MTs [24].

2.3.3 Deterministic or Probabilistic

Deterministic localization algorithms are algorithms that do not make use of the statistical information available regarding the measurement or prior information regrading the location of the MT when calculating the location. Probabilistic localization algorithms on the other hand take this information into account. Popular probabilistic methods include the particle filter algorithm and belief propagation based algorithms. Generally probabilistic localization algorithms perform better than deterministic localization algorithms when prior information or the noise distribution for the measurements are available [23].

2.3.4 Range-Free or Range-Based

Range-based localization algorithms typically convert signal measurements to some positional characteristic like angle or distance, which can then be used to estimate the MT location. Range-free localization algorithms on the other hand, do not convert signal measurements to a range for localization, instead another metric is used. Range Free localization algorithms can be classified into two groups. The first is scene analysis, which is also called fingerprint matching, as shown in Fig. 2.2(a). Initially a database containing signal measurements from the BSs for various possible locations of the MT in area (referred to as fingerprints) is created. Thereafter, when a MT wants to perform localization, the same signal measurement is performed in order to obtain a "fingerprint" of the MT and compared to the "fingerprints" in the database in order to find the MT location. This process is typically performed using a machine learning algorithm such as neural networks or the K-nearest neighbours (KNN) algorithm. This algorithm can achieve very high localization accuracy even in multipath and non-line-of-sight (NLOS) environment. However, there are several drawbacks. Firstly, the algorithm is very sensitive to the measurement used as the fingerprint. Secondly, the database of fingerprints used for training will be very large for a realistic operating scenario. Lastly, the training database has to regularly be updated to reflect changes in the environment.

The second group of range-free localization algorithms are the hop count algorithms. These algorithms count the number of sensor hops required for the data to be transmitted from the BS to the MT and use

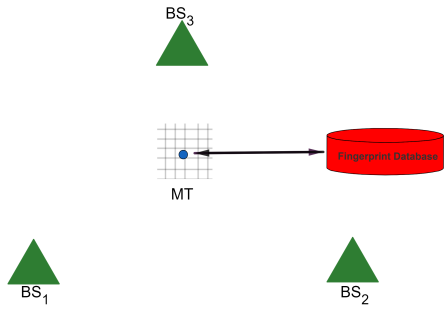

(a) Fingerprint matching

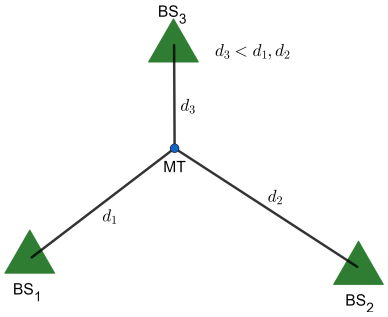

(b) Proximity

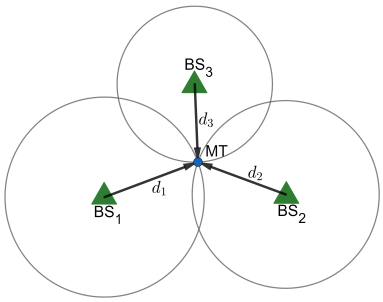

(c) Trilateration

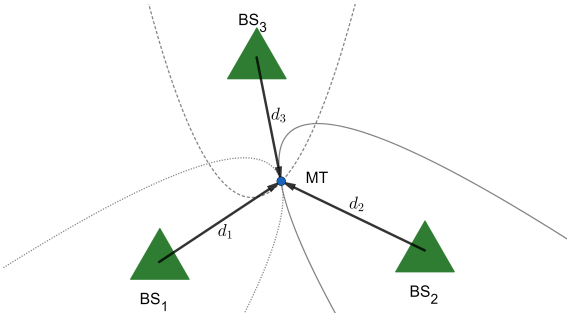

(d) TDOA

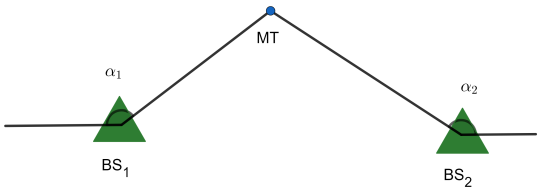

(e) Triangulation

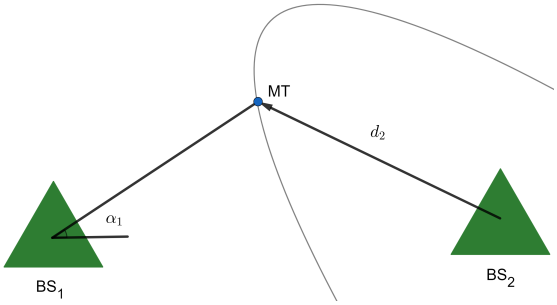

(f) Hybrid

Figure 2.2. Various range-free and range-based localization algorithms. Adapted from [23], ©2011 IEEE.

this information to calculate the location. For example, if the sensor range is R and it took 3 hops to go from the BS to the MT then the MT is in a circle of radius 3R away from the BS. While this technique is simple it provides a very poor accuracy [23].

Compared to range-free localization algorithms, range-based localization algorithms are much more diverse. One of the most widely used range based localization algorithm is localization through the

measurements of Received Signal Strength (RSS). Here firstly, the RSS of the signal from the MT is measured at several BSs. The RSS can be converted from power to distance using the appropriate path loss model as the transmission power is known. Based on the distance of the MT from the BSs, the MT location can be estimated through either proximity (Fig. 2.2(b)) or trilateration (Fig. 2.2(c)). When localizing through proximity, the MT location is decided as being that of the BS which is the closest to the MT, leading to a very poor localization accuracy. This techniques was widely used in Global System for Mobile Communication (GSM). In trilateration, circles with radius equivalent to the distance calculated by each BS from RSS measurements are drawn around the BSs. The location is calculated as the point at which these circles intersect. Trilateration provides superior accuracy compared to localizing through proximity but requires the MT to be connected to at least 3 BSs. The localization accuracy achieved from RSS based localization algorithms is not very high in general and the performance of these algorithms degrades severely in NLOS and shadowing conditions [23, 25].

Another group of range based localization algorithms are the Time-of-Arrival (TOA) based localization algorithms. Here firstly the BSs and the MT are required to be synchronized with each other. Thereafter, the MT transmits a signal at time T_0, which is know by all the BSs as they are synchronized with each other. The BSs calculate the TOA, τ, in reference to the known T_0 through correlation with the known transmitted signal. Based on the estimated TOA, the distance between the MT and the BS is calculated as

$$d = \tau.c, \tag{2.1}$$

where c is the speed of light, which is the velocity of propagation of the signal. The location can thereafter be calculated using either proximity or trilateration. The localization accuracy is directly related to the accuracy of the TOA estimate which is influenced by the bandwidth available. Similar to the RSS algorithm, the performance of the TOA algorithms also degrades in NLOS conditions. Another drawback of this algorithm is that it requires multiple BSs to be in synchronization with the MT being localized [23].

Time-difference-of-Arrival (TDOA) localization algorithms are very similar to TOA algorithms with the difference being that in TDOA algorithms, the BSs and the MT are not required to be synchronized, only the BSs have to be synchronized with each other. Here the TOA, τ_i, is measured at all the available BSs and the TDOA measurement is obtained as $\Delta\tau_i = \tau_i - \tau_1$ with BS with index $i = 1$ being chosen as the reference Remote Radio Head (RRH). This results in the unknown time of transmission term

being cancelled. The MT location can now be estimated by looking at the difference in the distance of the MT from pairs of BSs. With a single pair of BSs, the possible locations of the MT are given by a hyperbolic curve with the pair of BSs being the foci of the curve. The TDOA measurement from another BS is required, this can be paired with each of the two BSs from the previous pair to obtain two more hyperbolic curve and the MT location is estimated as the point of intersection of the three hyperbolic curves. The diagram shown in Fig. 2.2(d) illustrates this process. Similar to the TOA based localization algorithm the performance is directly related to the bandwidth available and the algorithm preforms poorly in NLOS scenarios [23].

Frequency-difference-of-Arrival (FDOA) localization techniques estimate MT location through measuring the shift in the frequency of the signal being transmitted by the MT caused by the movement of the MT. This frequency shift is proportional to its radial velocity. The instantaneous frequency of the signal transmitted by the MT is measured by multiple BSs and curves of constant differential Doppler shift are created; the point of intersection of these curves is determined to be the MT location. Similar to TDOA algorithms all the BSs need to be synchronized with each other. This method is not used often in practice as the receiver implementation is very costly [23].

In Angles-of-Arrival (AOA) localization algorithms; the angle of arrival of the signal transmitted by the MT is measured at multiple BSs and a Line of Bearing (LOB) is drawn by each BS based on the measured AOA; the point at which all the LOBs intersect is taken as the location of the MT (Fig. 2.2(e)). This method is also referred to as triangulation. Unlike localization using TOA and TDOA, AOA based localization only requires two BSs to obtain the MT location. The drawback of AOA based localization is that it require large complex antenna arrays to achieve reasonable spatial resolution. Furthermore, these arrays need to be regularly calibrated [23].

The algorithms mentioned here are often used in combination of one another to compensate for systems with limited measurement capabilities and to improve localization performance. The class of algorithms which makes use of the combination of the previously discussed algorithms is referred to as Hybrid localization algorithms [22]. An example of this type of localization algorithm can be seen in Fig. 2.2(f) where a AOA and TDOA measurements are used in combination.

In 2G technology the most common localization algorithm used was a proximity based algorithm referred to as the cell-ID method which was capable of achieving localization accuracy of up to 100 m.

While in 3G, the best performing localization techniques was a trilateration algorithm that reached an accuracy of up to 50 m. In 4G the TBS method which is a trilateration method achieved localization accuracy of less than 50 m. There are other methods for 2G-4G that incorporate information from GNSS sensors to achieve localization accuracy of up to 10 m [22].

2.4 5G LOCALIZATION

The 5G standardization is expected to provide 10-100x higher data rate, 1000x more user data volume per unit area, 10-100x higher number of connected devices, 10x longer battery life and 5x reduced end-to-end latency compared to the current 4G standard. These major boosts in communication are also expected to improve the localization capability of the infrastructure. This is primarily due the 5G standardisation employing several disruptive technologies such as: device-centric architectures, millimeter wave, massive multiple-in multiple-out (MIMO), smarter devices, and native support for machine-to-machine (M2M) communications. The device-centric architecture will result in an increase in the BS densities thus increasing the probability of having a LOS path between the BS and MT which makes localization much simpler. Millimeter wave allows the usage of higher carrier frequencies which provides more spectrum to use. This means the available bandwidth for communication also increases. Both of these lead to an increase in resolution of timing measurements leading to more accurate localization. Furthermore, the higher carrier frequencies allows for more compact antennas, i.e. a large number of antennas can be packed in a small space allowing for massive MIMO. Massive MIMO allows for directional beamforming between BSs and MTs further increasing the SNR and localization performance. Massive MIMO also leads to an increase in resolution of angular measurements further improving localization performance. Smarter devices lead to a higher probability of LOS of the MT to other MTs due to device-to-device (D2D) communications which can improve performance of cooperative localization algorithms. The native support for M2M communications expands the localization from MTs to a large variety of other devices [24].

The theoretical fundamental bounds for localization accuracy in 5G has been the focus of several studies [26–30]. All of these studies use the Cramér-Rao bound (CRB) to calculate theoretical bounds with the difference in the studies coming from the choice of the variables that are studied for their effect on the CRB. In [26] and [27] the CRB for localization with a single BS is evaluated. The primary focus of [26] is the effect on localization from the array structure, bandwidth and synchronization error. In [27] on the other hand, the trade-off between the diversity gain of using massive MIMO without beamforming and the high directivity guaranteed by the beamforming is investigated. The

CRB is evaluated for localization in both the uplink and downlink direction in [28, 29]. The effect of the number of antennas, the orientation of the MT and the effect of NLOS components is investigated in [28]. An investigation into the effect of beamforming and different localization protocol such as round-trip localization protocol (RLP) and collaborative localization protocol (CLP) is performed in [29]. In [30] the effect of inherent hardware faults in 5G systems, more specifically I/Q imbalances, on localization accuracy are investigated. All of these studies have indicated that in majority of the normal circumstances sub-meter localization accuracy can be achieved in 5G systems.

Owing to the various disruptive technologies in 5G and the promise of sub-meter localization error, several localization algorithms utilizing 5G have been developed. These are discussed in the sub-sections to follow.

2.4.1 Cooperative localization

The performance of cooperative localization is set to improve significantly in 5G networks due to the device-centric architecture, smarter devices and native support for M2M communication. Various different approaches to cooperative localization have therefore been studied in literature [31–33]. In [31], a distributed cooperative localization method is presented. The article presents a linear solution to the cooperative localization problem for both static and dynamic MTs that only requires local measurements. Furthermore, due to the linearization of the localization calculations, all the computation required for localization can be performed locally without any communication with a BS. This approach provides an advantage over the typical centralized localization algorithms as the computational load for localization becomes distributed. This will become especially useful as the number of devices in 5G networks increase in the near future.

An alternate distributed localization algorithm referred to as Enhanced Cooperative Group Localization (ECGL) is proposed in [33]. This algorithm takes advantage of both the high network density and massive MIMO available in 5G as it performs cooperative localization using RSS and AOA measurements. The resulting algorithm firstly uses the RSS and AOA measurements to identify two BSs which are in LOS through the Enhanced hybrid hypothesis test (EHHT). Using these two BSs, the ECGL algorithm thereafter localizes the group of MTs simultaneously. A completely different approach to cooperative localization is proposed in [32] using Belief Propagation (BP). The presented algorithm expands on existing belief propagation methods for cooperative localization by proposing a way for incorporating information about the connectivity between MTs and BSs to minimize the location

uncertainty propagation encountered in BP-based cooperative localization.

The only cooperative localization algorithm here that achieved sub-meter localization error is the BP based algorithm from [32]. This is followed by [31] which achieves localization performance in the range of less than 10 m. The lowest localization accuracy is achieved by the ECGL algorithm from [33] which can be between 10-100 m depending on the parameters used.

2.4.2 Fingerprint Matching

Fingerprint matching is another algorithm that has been widely studied for localization in 5G [34–36]. The variations in these studies are in the type of measurements used as the fingerprint and the model used to predict the MT location from the fingerprint measurement. In [34], a vector of RSS taken at a distributed massive MIMO BS is used for as the fingerprint. A Gaussian process regression model is then used to predict location of the MT. The algorithm proposed in [35], on the other hand uses sample spatial covariance matrix computed from the channel state information (CSI) as fingerprints with a single-layer random feed-forward neural network, referred to as an extreme learning machine (ELM), used to model the signal measurement to location function. A completely different approach is considered in [36]. Firstly, New radio user equipment measurement data (NUMD) is used and instead of taking a single measurement like in the previously discussed algorithms, multiple measurements are taken over a time period and stitched together to use as a fingerprint. The predication of location from this time series of measurements is performed using a Hidden Markov Model (HMM).

The localization performance achieved by the models proposed in [34–36] are very similar. A localization error of less than 10 m is achieved 80% of the time in NUMD based algorithm from [36] while both [34] and [35] achieve RMSE localization error values between 10-20 m depending on the the values of different variables.

2.4.3 Direct Localization

Direct localization algorithms are a type of range-free localization algorithms that have been studied extensively in literature for localization in 5G systems [37–40]. The Direct Source Localization (DiSoul) algorithm proposed in [37] is the most widely referenced direct localization algorithm. This algorithm takes advantage of the channel sparsity of the mm-wave band combined with the high angular resolution available with massive MIMO as localization is achieved through a compressed sensing framework making use of AOA measurements from multiple BSs. The algorithm jointly processes the signals received by several BSs to identify the LOS components by checking which components point

to the same location for all BSs. This location is then taken as the location of the MT. Additionally, the DiSoul algorithm also makes use of course TOA estimates to narrow down the search area for possible locations of the MT.

In [38], a very similar approach to the DiSoul algorithm is used with the difference being that this algorithm uses a Bayesian inference based compressed sensing framework to perform localization. Owing to the fact that Bayesian inference is used, this method allows for the incorporation of prior statistical location information which is not possible with [37]. Furthermore, this algorithm provides statistical information regarding the MT location instead of just the measurement.

A drastically different approach to direct localization is proposed in [39, 40]. Both [39] and [40] present algorithms for indoor localization in a LOS environment. The algorithm presented in [39] takes advantage of the massive MIMO beamforming capabilities in 5G whereby multiple BSs scan a grid of area through beam steering to get MT location. The localization occurs in multiple stages whereby initially the scanning grid is large and the MT and BSs are not synchronized. The search grid is thereafter iteratively refined till a satisfactory resolution is achieved. The estimated location at this state is taken as the MT location and any subsequent changes to the MT location are tracked using coherent localization methods. The authors in [40] on the other hand proposes three different coherent direct localization algorithms, two maximum-likelihood-type (ML) algorithms and one steered covariance matrix-based MUSIC-type (SCM-MUSIC). All three of these proposed algorithms look at various locations on a defined search grid with the MT location being chosen as the location that maximizes a criterion function. The criterion function used is different for all three algorithms.

The localization accuracy achieved by indoor localization algorithms from [39] and [40] is significantly higher compared to [37] and [38] and perhaps better than all existing 5G localization algorithms as a sub-millimeter localization error is achievable. The caveat here is that these algorithms are only well suited for an indoor environment where the MT is stationery. The DiSoul algorithm from [37] and Bayesian inference based algorithms from [38] have similar performances with sub-meter localization error being achieved in most of the scenarios. However, based on the comparison shown in [38] to the DiSoul algorithm, it is clear that for cases where the prior statistical location information regarding the MT is available [38] performs better than [37].

2.4.4 Localization through compressed sensing

Localization algorithms that take advantage of the channel sparsity in mm-wave band by localizing using compressed sensing algorithms were discussed previously under direct localization [37, 38]. There are alternate compressed sensing based localization methods proposed in literature [6–8] that perform range-based localization instead of performing direct localization. Furthermore, these methods are all hybrid algorithms requiring only one BS to perform localization instead of multiple BSs like the direct localization algorithms. This is possible because these hybrid algorithms are able to calculate all the channel parameters (AOA, TOA and AOD) thus the MT location can be completely specified by its bearing and its distance from the BS in 2D space. Additionally the AOA and the AOD measurements can also be used to approximate the orientation of the MT.

The work performed by [6] lays the foundation for [7] and [8] as all three of these studies use a very similar framework for calculating channel parameters. This framework consists of using the Distributed Compressed Sensing - Simultaneous Orthogonal Matching Pursuit (DCS-SOMP) method to decompose the received signal into LOS and NLOS components and estimating the AOA and AOD for each component. The TOA for each path is thereafter estimated by the QR factorisation of the sparse dictionary matrix obtained from the decomposition. Besides this, [6] uses the SAGE algorithm for the coarse estimation AOA and AOD while [7] and [8] use an iterative refinement method. The estimated channel parameters are then used to obtain the MT location. These algorithm allow for localization of the MT even in cases where no LOS path is present in between the BS and the MT using just the NLOS components. Furthermore, [7] and [8] offer statistical information regarding the MT location while [6] just provides a point estimate. The difference between [7] and [8] is the way the statistical information of the MT is calculated.

The localization performance achieved by algorithms proposed in all three of these studies is very similar as they build on each other. Comparing their performance for LOS environment, both [7] and [8] achieve a localization error of less than 10 cm at an SNR less than -20 dB while in [6] it is achieved at an SNR of -5 dB. Thus, [7] and [8] provide superior performance compared to [6].

2.4.5 Range-based algorithms

There has been some studies in non-hybrid range-based algorithms that use methods like triangulation [41, 42]. There is also a study [43] that propose new algorithms for getting user location from range measurements as an alternative to trilateration. In [43], a method based on analytical geometry referred

to as radical centers is proposed. While this method has been used in previous studies, [43] provides a way for improving its performance. In the proposed algorithm, distance measurements from four reference nodes are used to generate one radical center in 3D space. A filtering algorithm is proposed to fuse estimates and also remove unsuitable measurements. The filter radical centers are then averaged to obtain a final estimate for the MT location.

Both [41] and [42] on the other hand propose an AOA based localization algorithms that make use of triangulation. In [41], a multi-stage algorithm is proposed. Here initially the AOA at several BSs is measured to provide a coarse estimation of the user location and the hosting BS is identified. This is followed by a second stage where the hosting BS does multistage beamforming to find a coarse estimation of the MT location. This is similar to the previously discussed direct localization method from [39] but now for an outdoor scenario. The algorithm proposed by [42] takes advantage of the high angular resolution of massive MIMO by proposing a pure AOA based localization algorithm that estimates the AOA using the LOS component. What sets [42] apart from the other studies mentioned previously is that it is not merely a simulation study, but it actually creates the localization scenario in real life using Software Defined Radios (SDRs) 5G MIMO systems to verify if the proposed solution does provide satisfactory results.

The radical centers based algorithm from [43] cannot be directly compared to that of [41] and [42]. However, based on the simulations performed in [43], it is clear that the algorithm of radical centres does provide an improvement in localization accuracy compared to using trilateration. The simulation study performed in [41] and [42] indicate that both these algorithms can achieve sub-meter localization error. However, the method provided in [42] is superior as it can achieve sub-meter localization error with simpler array configuration and the method has also been verified outside of simulation.

2.5 APPLICATIONS OF 5G LOCALIZATION

The algorithms discussed in this section include algorithms that not only localize the MT but they also perform other functions such as tracking, mapping or synchronization using 5G infrastructure. These techniques allow for the use of localization in ways that can improve the communication performance through location based network optimizations and also cater for other location based services such as the tracking of vehicles for intelligent transportation.

2.5.1 Localization and Tracking

Localization and tracking using 5G infrastructure has been studied extensively in literature [44–49]. These studies typically use a unique localization method paired with the Extended-Kalman-Filter (EKF) for tracking channel parameters (AOA, AOD and TOA) or directly tracking the user location. In [44], an algorithm for indoor localization and tracking is proposed for use in assisted living scenarios. The proposed method is a maximum likelihood localization algorithm that initially estimates the delays for each of the multipath components observed by the receiver. These delays are corrected based on the map of the indoor environment generated from previous observations. The channel parameters are thereafter paired with an EKF to obtain user location and update the map of the indoor environment.

A method for beam selection combined with MT location and orientation tracking is proposed in [45]. Here initially the MT location is tracked by the BS using beam selection combined with TOA and AOA tracking. The MT thereafter uses this information and performs beam selection and tracking of the BS to estimate and track its own orientation. The tracking of the channel parameters is performed using an EKF with the beam selection performed using angular uncertainties provided by the EKF.

In [46], a very similar approach to [45] is used as TOA and Direction of Arrival (abbreviated DOA and defined as the complementary angle of AOA) measurements are used for localization. The estimation of these channel parameters is performed using uplink (UL) reference signals. What sets [46] apart is that it uses a cascaded EKF for the tracking the MT location and the algorithm considers an ultra dense 5G network scenario (maximum inter-site distance of 50 m). The first stage of the cascaded EKF tracks the TOA and the AOA at every access node. In the second stage the tracked AOA and TOA from each access node are fused together and the MT location is tracked. This methods also provides for a way for achieving clock synchronization using the tracked channel parameters. Similarly in [48, 49], a two stage cascaded EKF is used for tracking the MT location. However, here the channel parameter tracked and used for localization is the Direction of Departure (abbreviated DOD and defined as the complementary angle of the AOD) at the BSs. The DOD is estimated at the BS through estimated beam-pair gains between the BS and the MT. These beam-pair gains are estimated by the MT using the periodically transmitted downlink (DL) reference signals transmitted by the BS. The difference between the algorithm proposed in [48] and [49] is that [49] considers the effects of orientation uncertainties cause by installation errors in the antenna. The algorithm proposes for a way to estimate this uncertainty and accurately localize the MT in the presence of it.

A much simpler approach is considered in [47] with only a single stage EKF being used for tracking. The AOA and AOD values for the LOS path between the MT and the BS are tracked in [47]. The study considers a 5G ultra dense network with the primary aim of tracking AOA and AOD being to obtain the beamforming weight vectors for both the BS and the MT.

The studies mentioned here cannot all be directly compared as all the algorithms are not designed for the same scenario. For indoor environments, [44] achieves the best performance as sub-meter localization error is achieved for LOS, NLOS and obstructed-line-of-sight (OLOS) environment; however, this algorithm will be impractical for an outdoor scenario. While for outdoors [49] achieves sub-meter localization error 99% of the time, even under orientation uncertainties. In [46], similar performance is achieved but orientation uncertainties are not considered. Poorer performance is seen in [48] with sub-meter localization error being achieved only 80% of the time. Similarly the method proposed in [45] also achieves sub-meter accuracy for 80% of the tracked trajectory. For the algorithm proposed in [47], the localization error is not provided. However, a median error of less than 1.5° is achieved in the estimation both the azimuth and elevation angle at the BS and the MT.

2.5.2 Tracking of high-speed Trains (HST)

The algorithms for tracking HSTs are localization and tracking algorithms. These studies are discussed separately due the specific nature of the application. This is not a widely studied area and a few very similar studies exist in literature [2–5]. All these studies either use a TDOA based localization method or a TOA and AOD based localization method. The output of the localization algorithm is fed into an EKF which track the train's position. The first study [2] applies the proposed algorithm for beamforming. In [3], both TOA and AOD measurements are used for localization with these measurements being taken using signals specified for use in synchronization in the 5G standardization. The effects of using network slicing capabilities to minimize latency and the data rates achievable with the proposed TDOA based localization algorithm are investigated in [4]. An alternate tracking method using the same TDOA based localization is proposed in [5], whereby an EKF with a non-linear state model is considered.

The localization performance achieved in all these studies is very similar with the best performance being achieved in [4] when network slicing is used to perform localization at 10 ms intervals using 400 MHz of bandwidth and 5 track-side RRH units. Here sub-meter localization error is achieved more than 99% of the time. The next best performing algorithm is [2] with sub-meter localization

error being achieved 90% of the time. When using 5G synchronization signals to estimate AOD and TDOA values, [3] achieves sub-meter localization error over 80% of the simulated trajectory. Lastly, the performance achieved in [5] is the poorest. However, the simulation parameters were different compared to the previous studies as a real life track was considered. Furthermore, based on the new simulation parameters, the localization performance of the EKF with a non-linear state model is better, compared to when a linear state model is used.

2.5.3 Localization and Mapping

There have been several algorithms proposed [50, 51] that perform both localization and radio mapping of the propagation environment similar to [44] but without tracking. Both [50] and [51] are very similar algorithms that perform localization and mapping using BP based estimator. The AOA, AOD and the TOA of the LOS path and the multipath components are used for localization and mapping of the propagation environment. The algorithm can even localize in the absence of a LOS path using just the NLOS paths. The difference between the two studies is that [51] also provides a way to achieve synchronization between the BS and MT. Furthermore, [51] considers a scenario where the MT is moving while [50] considers a stationery scenario. The performance of both of these algorithms is relatively poor as sub-meter localization error is not achieved. However, in comparison [51] performs better than [50].

2.5.4 Localization and Beamforming

Localization algorithm can be used for beamforming as discussed previously in [47–49]. However, these algorithms make use of an EKF for tracking the MT location to use for beamforming. The algorithm presented in [52] does not consider tracking. Instead a successive localization and beamforming (SLAB) algorithm is proposed. In the SLAB process, the BS beamforming vector, the MT location and the instantaneous channel state are optimized one after the other. The result of this process is a sequence of location estimates and BF updates. The performance of this algorithm converges to the genie-aided beamforming strategy (the optimal beamforming with a known MT location) and sub-meter localization error is achieved.

2.6 CONCLUDING REMARKS

This chapter covers the existing literature in the area of localization and tracking of trains and 5G localization. From the discussion of the various exiting methods in literature in Section 2.2 it is clear that a simple algorithm that can accurately localize a HST is required. Furthermore, from Section 2.4 and Section 2.5 it is clear that there are various different 5G localization algorithms that can localize a

MT with sub-meter accuracy and can be applied to the problem of tracking of a HST. The next chapter discusses one such algorithm, the DCS-SOMP algorithm.

CHAPTER 3 LOCALIZATION THROUGH COMPRESSED SENSING

3.1 INTRODUCTION

As discussed in Chapter 2, there are multiple different 5G localization algorithms that can accurately localize a MT, which are capable of achieving sub-meter accuracy. However, all of these algorithms cannot be practically applied to the problem of localization of HSTs. Cooperative localization algorithms require a high density of MTs, which is usually not present in the HST scenario. Localization using fingerprint matching requires a database of signal measurements from around the BS that needs to be constantly updated. Range-based localization algorithms and direct localization algorithms can be used. However, these algorithms require multiple BSs to localize the MT, which can be an impractical requirement. Compressed sensing based localization algorithms [6–8] on the other hand can localize a MT using a single BS with high accuracy. Sub-meter accuracy can be achieved with SNR values as low as -20 dB. This makes it the ideal choice for use in the application of localization and tracking of HSTs.

The compressed sensing based localization algorithm proposed in [6–8] takes advantage of the fact that the mmWave channel is approximately sparse in the angular domain and thus permits angular decomposition using the DCS-SOMP algorithm. The decomposed components in the angular domain can thereafter be used to accurately determine the MT location. The rest of the chapter discusses how DCS-SOMP algorithm performs this localization. The first section discusses the system model assumed by the localization algorithm. Following this, the implementation of DCS-SOMP is discussed. In Section 3.4 the modified version of the DCS-SOMP algorithm that makes used of LOS tracking is discussed. This is followed by Section 3.5 which discusses the effect of various algorithm parameters on localization accuracy. Lastly, in Section 3.6 some concluding remarks are made.

3.2 SYSTEM MODEL

Similar to previous studies [2–5], the system model is based on the HST scenario specified by the 3GPP in [9] for carrier frequencies around 30 GHz. Fig. 3.1 illustrates the system model whereby RRH units are positioned on alternating sides of the tracks every 580 m. The RRH units are positioned 5 m away from the track. Each RRH unit contains two antenna panels each angled at 45° and 135° while the train has two antenna panels positioned at 0° and 180°.

The system model can further be divided into three parts: The transmitter model, the channel model and the receiver model. These are discussed in the sub-sections below.

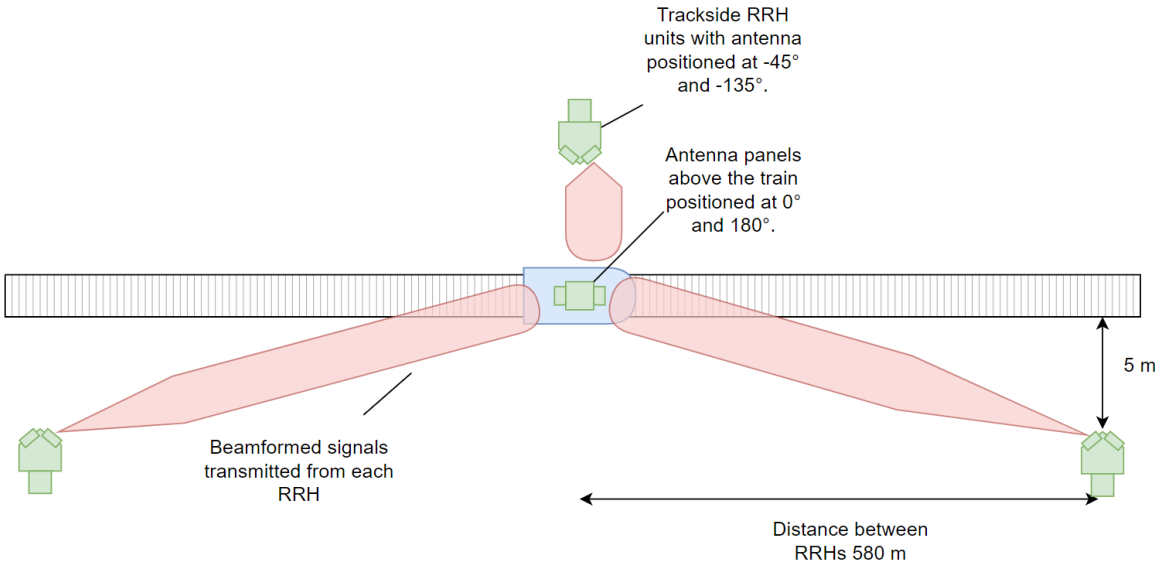

Figure 3.1. The system model for the HST scenario as specified by the 3GPP for carrier frequencies around 30 GHz in [9].

3.2.1 Transmitter model

The *rth* BS/RRH ($\mathbf{RRH}_r$) contains N_t antennas and transmits M beamformed Orthogonal Frequency Division Multiplexing (OFDM) symbols on N carriers. Thus,

$$\mathbf{RRH}_r[m,n] = \mathbf{F}_r[m,n]\mathbf{x}_r[m,n], \tag{3.1}$$

where $\mathbf{F}_r$ is the beamforming matrix, $\mathbf{x}_r$ is the transmitted signal, n is the carrier index and m is the symbol index.

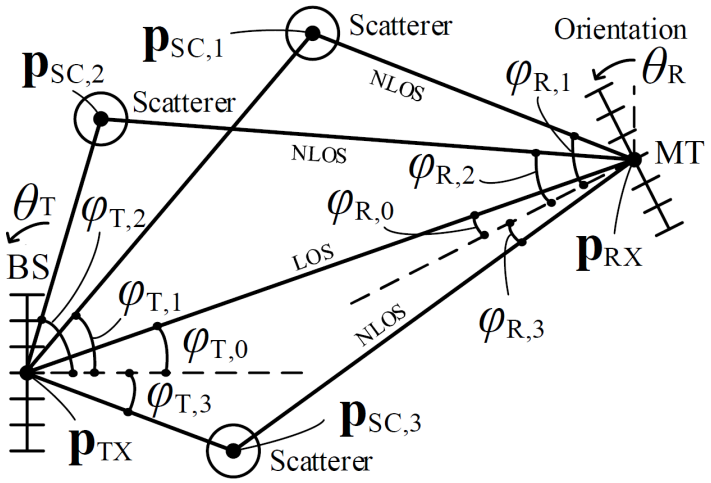

Figure 3.2. The positional parameter for the channel in a typical localization scenario. Taken from [8], ©2011 IEEE.

3.2.2 Channel model

The general MIMO mmWave channel model in 2D (presented in [53] and used in [6–8]), which also resembles the mmWave HST channel model $\mathbf{H}[n] \in \mathbb{C}^{N_r \times N_t}$ at a specific instant in time t [54], can be represented as follows:

$$\mathbf{H}[n] = \mathbf{A}_{\mathrm{Rx}}[n]\Gamma[n]\mathbf{A}_{\mathrm{Tx}}^{\mathrm{H}}[n], \tag{3.2}$$

where the response vectors are

$$\begin{aligned} \mathbf{A}_{\mathrm{Tx}}[n] &= \left[\mathbf{a}_{\mathrm{Tx},n}\left(\varphi_{\mathrm{T},0}\right), \ldots, \mathbf{a}_{\mathrm{Tx},n}\left(\varphi_{\mathrm{T},K}\right)\right], \\ \mathbf{A}_{\mathrm{Rx}}[n] &= \left[\mathbf{a}_{\mathrm{Rx},n}\left(\varphi_{\mathrm{R},0}\right), \ldots, \mathbf{a}_{\mathrm{Rx},n}\left(\varphi_{\mathrm{R},K}\right)\right], \end{aligned} \tag{3.3}$$

while $\Gamma[n]$ is given by

$$\Gamma[n] = \sqrt{N_t N_r} \times \mathrm{diag}\left\{ \frac{1}{\sqrt{\rho_0}} e^{\frac{-j2\pi n\tau_0}{NT_s}}, \ldots, \frac{1}{\sqrt{\rho_K}} e^{\frac{-j2\pi n\tau_K}{NT_s}} \right\}. \tag{3.4}$$

The subscript k specifies the index of the path whereby $k = 0$ is the LOS path and the rest are NLOS paths with K total paths; ρ_k is the path loss; τ_k is the time delay; N_r is the number of antennas at the receiver, N_t is the number of antennas at the transmitter and T_s is the sampling time. Furthermore, $\mathbf{a}_{\mathrm{Tx},n}\left(\varphi_{\mathrm{T},k}\right) \in \mathbb{C}^{N_t}$ and $\mathbf{a}_{\mathrm{Rx},n}\left(\varphi_{\mathrm{R},k}\right) \in \mathbb{C}^{N_r}$ in the response vectors are the frequency dependent steering vectors for the receiver and the transmitter respectively. The steering vectors specify the phase delay in radians experienced by each antenna in the array for the broadside AOD, $\varphi_{\mathrm{T},k}$, and AOA, $\varphi_{\mathrm{R},k}$, of the signal for the kth path. A more clearer definition of these angles for each path can be seen in Fig. 3.2. The steering vectors are specified based on the array structure used. Assuming a Uniform Linear Array

(ULA) structure, the steering vector is specified by the following formula:

$$\mathbf{a}_{\mathrm{Tx},n}(\varphi_{\mathrm{T},k}) = \frac{1}{\sqrt{N_t}}\left[e^{-j\frac{N_t-1}{2}\frac{2\pi}{\lambda_n}d\sin(\varphi_{\mathrm{T,k}})},\ldots,e^{j\frac{N_t-1}{2}\frac{2\pi}{\lambda_n}d\sin(\varphi_{\mathrm{T},k})}\right]^{\mathrm{T}}, \tag{3.5}$$

where λ_n is the signal wavelength at the nth sub-carrier and d is the distance between the antenna elements in the array [6]. The steering vector for the receiver, $\mathbf{a}_{\mathrm{Rx},n}(\varphi_{\mathrm{R},k})$, is specified in a similar way to (3.5).

3.2.3 Receiver Model

Using the channel model mentioned above, the Fast Fourier Transform (FFT) of the received signal, $\mathbf{y}$, from the rth RRH can be described as

$$\mathbf{y}_r[m,n] = \mathbf{H}_r[n]\mathbf{F}_r[m,n]\mathbf{x}[m,n] + \mathbf{n}_r[m,n], \tag{3.6}$$

where $\mathbf{n}_r[m,n] \in \mathbb{C}^{N_r}$ is zero-mean Additive White Gaussian Noise (AWGN). Furthermore, it is assumed that the transmitter and the receiver are in perfect synchronization with each other and the cyclic prefix is removed perfectly. The received signal can now be used to localize the train.

As mentioned before, the HST channel model at a specific instance in time can be described by the model mentioned above. The channel in fact changes with time as the train is moving. Hence, the position of the scatterers and reflectors change with time. Despite of this, the model discussed above is still applicable as long as the channel does not change during the transmission of M symbols. This assumption is in fact violated; however, not significantly. Based on typical parameter values (30 OFDM symbols, M, are transmitted and a bandwidth of 247.46 MHz is used with an FFT size of 2048), a HST train moves between 3-10 cm (depending on the size of the cyclic prefix used) during the transmission of 30 symbols when travelling at a maximum speed of 500 km/h. This movement during the transmission of M symbols is therefore small enough to be neglected.

3.3 THE DCS-SOMP ALGORITHM

The channel model $\mathbf{H}$ can be converted to the angular beamspace domain $\mathbf{H}_\varphi \in \mathbb{C}^{N_r \times N_t}$ as follows:

$$\mathbf{H}_\varphi[n] = \mathbf{U_R}^H \mathbf{H}[n]\mathbf{U_T}. \tag{3.7}$$

Here $\mathbf{U_R}$ and $\mathbf{U_T}$ are unitary Discrete Fourier Transform (DFT) matrices. For the ULA configuration, $\mathbf{U_T}$ and similarly $\mathbf{U_R}$ are defined as

$$\mathbf{U}_\mathrm{T} = \left[\mathbf{u}_\mathrm{T}\left(\nu_\mathrm{T}^{(0)}\right),\ldots,\mathbf{u}_\mathrm{T}\left(\nu_\mathrm{T}^{(N_t-1)}\right)\right], \tag{3.8}$$

where

$$\mathbf{u}_{\mathrm{T}}\left(\nu_{\mathrm{T}}^{(l)}\right)=\left[e^{-j2\pi\frac{N_t-1}{2}\nu_{\mathrm{T}}^{(l)}},\ldots,e^{j2\pi\frac{N_t-1}{2}\nu_{\mathrm{T}}^{(l)}}\right]^T, \tag{3.9}$$

and

$$\nu_{\mathrm{T}}^{(l)}=-\frac{N_t-1}{2N_t}+\frac{l}{N_t}. \tag{3.10}$$

This transformation matrix corresponds to a beamspace representation with uniformly spaced spatial angles ν_l that form an orthogonal basis. The angular resolution for the AOA and AOD is $1/N_r$ and $1/N_t$ respectively. It has been shown in [6] that $\mathbf{H}_\varphi[n]$ is approximately sparse as majority of the signal energy is concentrated in the direction of $\{\varphi_{R,k}\}$ and $\{\varphi_{T,k}\}$. Taking the beamspace representation of the channel and stacking the M received symbols, the received signal at the RRH can be represented as

$$\mathbf{y}_\varphi[n]=\mathbf{\Omega}[n]\mathbf{h}_\varphi[n]+\mathbf{n}_\varphi[n], \tag{3.11}$$

where

$$\mathbf{\Omega}[n]=\left[\mathbf{\Omega}_{0,n},\ldots,\mathbf{\Omega}_{M-1,n}\right]^T, \tag{3.12}$$

with

$$\mathbf{\Omega}_{m,n}=\left(\mathbf{U}_{\mathrm{T}}^H\mathbf{F}[m,n]\mathbf{x}[m,n]\right)^T\otimes\mathbf{U}_{\mathrm{R}}, \tag{3.13}$$

and

$$\mathbf{h}_\varphi[n]=\mathrm{vec}\left(\mathbf{H}_\varphi[n]\right). \tag{3.14}$$

Here $\otimes$ represents the operation of the Kronecker product and vec is the vectorization operator. As $\mathbf{h}_\varphi$ is an approximately sparse vector, solving for $\mathbf{h}_\varphi$ from (3.11) can be considered a compressed sensing problem. The column of $\mathbf{U_T}$ and $\mathbf{U_R}$ (which makes up the dictionary or sensing matrix $\mathbf{\Omega}[n]$) corresponding to each of the non-sparse entries provides the AOA/AOD for each path. The $\mathbf{h}_\varphi[n]$ entries provides the complex channel coefficient, which can be used to estimate the TOA for each path. As $\mathbf{h}_\varphi$ and $\mathbf{\Omega}[n]$ are jointly sparse across all sub-carriers, the DCS-SOMP algorithm can be used for channel estimation [6].

The DCS-SOMP algorithm, originally proposed in [55], has been applied to the problem of channel estimation for localization in [6–8]. The process can be broken up into four parts: coarse AOA/AOD estimation, fine AOA/AOD estimation, TOA estimation and position/orientation estimation. These are described in the sub-sections to follow.

3.3.1 Coarse AOA/AOD estimation

This part of the algorithm is common to all three studies [6–8]. Here the coarse estimates of the AOA and the AOD for each path between the transmitter and the receiver are estimated. The following steps are taken for coarse AOA and AOD estimation:

1. The residual vector, $\mathbf{r}$, is initialized by setting it to $\mathbf{r}_{-1} = \mathbf{y}_{\varphi}[n]$ and the iteration index s is set to 0.

2. The course estimates of the AOD and AOA for the sth path in beamspace are found as follows. Let

$$\tilde{q}_s = \arg\max_{i=0,\ldots,N_{\Omega}-1} \sum_{n=0}^{N-1} \frac{\left|\boldsymbol{\omega}_i^H[n]\mathbf{r}_{s-1}[n]\right|}{\|\boldsymbol{\omega}_i[n]\|}, \tag{3.15}$$

Here the superscript H is used to indicate that the Hermitian matrix of ω_i is used. Using this define

$$q_{\mathrm{T},s} = \left\lceil \frac{\tilde{q}_s}{N_r} \right\rceil \tag{3.16}$$

and

$$q_{\mathrm{R},s} = \mathrm{mod}\,(\tilde{q}_s, N_r)\,. \tag{3.17}$$

Here mod refers to the modulus operator. Using $q_{\mathrm{R},s}$ and $q_{\mathrm{T},s}$ we get $\hat{\nu}_{\mathrm{T},s}$ and $\hat{\nu}_{\mathrm{R},s}$ as

$$\begin{aligned} \hat{\nu}_{\mathrm{T},s} &= \nu_{\mathrm{T}}^{(q_{\mathrm{T},s})}, \\ \hat{\nu}_{\mathrm{R},s} &= \nu_{\mathrm{R}}^{(q_{\mathrm{R},s})}. \end{aligned} \tag{3.18}$$

In (3.15), $\boldsymbol{\omega}_i[n]$ is the ith column of the basis/dictionary $\boldsymbol{\Omega}[n]$, the numerator of the summation represents the Frobenius inner product between $\boldsymbol{\omega}_i[n]$ and $\mathbf{r}_{s-1}[n]$ and the denominator represents the Frobenius norm of $\boldsymbol{\omega}_i[n]$. In (3.15), the residual vector (the received signal) is projected onto each of the basis/entries of the dictionary matrix and the basis onto which the projection is the largest is chosen as one of the paths. The column index of the path found in the dictionary $\boldsymbol{\Omega}[n]$ is represented by $\tilde{q}_s$. Since the dictionary matrix is made from the the transformation matrices $\mathbf{U}_{\mathrm{T}}$ and $\mathbf{U}_{\mathrm{R}}$ which consists of beamspace angles $\nu_{\mathrm{T}}^{(l)}$ and $\nu_{\mathrm{R}}^{(l)}$, the coarse AOD and AOA estimates are taken as the angles corresponding to the chosen basis/dictionary entry. The indices for the AOD and AOA, $q_{\mathrm{T},s}$ and $q_{\mathrm{R},s}$, are calculated from $\tilde{q}_s$ based on the way the Kronecker product operates in (3.13).

3. The basis vector selected is orthogonalized against the set of previously selected basis vectors with $\boldsymbol{\psi}_{-1}[n] = 0$. Thus,

$$\boldsymbol{\psi}_s[n] = \boldsymbol{\omega}_{\tilde{q}_s}[n] - \sum_{\tilde{s}=-1}^{s-1} \frac{\boldsymbol{\omega}_{\tilde{q}_s}^H[n]\boldsymbol{\psi}_{\tilde{s}}[n]}{\|\boldsymbol{\psi}_{\tilde{s}}[n]\|} \boldsymbol{\psi}_{\tilde{s}}[n]. \tag{3.19}$$

4. The residual vector is updated to to remove the projection of the basis vector found in the current iteration. Thus,

$$\mathbf{r}_s[n] = \mathbf{r}_{s-1}[n] - \beta_s[n]\boldsymbol{\psi}_s[n], \tag{3.20}$$

where

$$\beta_s[n] = \frac{\boldsymbol{\psi}_s^H[n]\mathbf{r}_{s-1}[n]}{\|\boldsymbol{\psi}_s[n]\|^2}. \tag{3.21}$$

5. The convergence criterion, $\sum_{n=0}^{N-1} \|\mathbf{r}_s[n] - \mathbf{r}_{s-1}[n]\|^2 \leq \varepsilon$ is evaluated. Here ε is a threshold value based on the SNR of the received signal. If the convergence criterion is not met, it means that more paths are present. Thus, the algorithm repeats starting from step 2. Alternatively, the number of iterations for the algorithm can be fixed to a certain number of paths.

3.3.2 Fine AOA/AOD estimation

This part of the algorithm finds fine estimates for the AOA and AOD for each of the paths found in the coarse estimation. In [45], the space-alternating generalized expectation maximization (SAGE) algorithm is used for this. Whereas in [7, 8], an iterative refinement algorithm is used. We use the iterative refinement algorithm due to the algorithm achieving better performance. The following processing is performed for kth path found:

1. Set the iteration index s to 0. Set $\hat{\nu}_{\mathrm{T},k,s-1}$ to $\hat{\nu}_{\mathrm{T},k}$ and $\hat{\nu}_{\mathrm{R},k,s-1}$ to $\hat{\nu}_{\mathrm{R},k}$ from the coarse estimation. Furthermore, the AOA resolution, $\kappa_{\mathrm{T},k,s-1}$, and the AOD resolution, $\kappa_{\mathrm{R},k,s-1}$, is set to $1/N_r$ and $1/N_t$ respectively.
2. The beamspace transformation matrix $\mathbf{U}_{\mathrm{T}}$ is redefined so as to quadruple the resolution ($\kappa_{\mathrm{T,k,s}} = \kappa_{\mathrm{T,k,s-1}}/4$). Thus,
$$\mathbf{U}_{\mathrm{T},k,s} = \left[\mathbf{u}_{\mathrm{T}}\left(\nu_{\mathrm{T},k,s}^{(0)}\right), \ldots, \mathbf{u}_{\mathrm{T}}\left(\nu_{\mathrm{T},k,s}^{(4)}\right)\right], \tag{3.22}$$
where
$$\nu_{\mathrm{T},k,s}^{(l)} = \tilde{\varphi}_{\mathrm{T},k,s-1} - \frac{\kappa_{\mathrm{T,k,s-1}}}{2} + l\,\kappa_{\mathrm{T},k,s}. \tag{3.23}$$
The same operation is applied for $\mathbf{U}_{\mathrm{R},k,s}$.
3. A new dictionary matrix, $\mathbf{\Omega}_{k,s}[n]$, is constructed based (3.12) and (3.13) using the new $\mathbf{U}_{\mathrm{T},k,s}$ and $\mathbf{U}_{\mathrm{R},k,s}$.
4. The calculation of (3.15) is performed again using $\mathbf{\Omega}_{k,s}[n]$ and setting $\mathbf{r}_{s-1} = \mathbf{y}_{\varphi}[n]$. The new AOD and AOA estimates are obtained as follows,
$$\hat{\nu}_{\mathrm{T},k,s} = \nu_{\mathrm{T},k,s}^{(q_{\mathrm{T},k,s})}, \tag{3.24}$$
and
$$\hat{\nu}_{\mathrm{R},k,s} = \nu_{\mathrm{R},k,s}^{(q_{\mathrm{R},k,s})}, \tag{3.25}$$
where
$$q_{\mathrm{T},k,s} = \left\lceil \frac{q_{k,s}}{5} \right\rceil \tag{3.26}$$
and
$$q_{\mathrm{R},k,s} = \mathrm{mod}\left(q_{k,s}, 5\right). \tag{3.27}$$

The mod refers to the modulus operation. Furthermore, the $q_{k,s}$th column of $\mathbf{\Omega}_{k,s}[n]$ is saved as $\hat{\boldsymbol{\omega}}_k[n]$. This will be used when finding TOA estimate.

5. If the desired resolution for AOA and AOD has been achieved the actual value for AOA and AOD are calculated as

$$\begin{aligned}\hat{\varphi}_{\mathrm{T},k} &= \arcsin\left(\frac{\lambda_c}{d_{\mathrm{ant}}}\hat{v}_{\mathrm{T},k,s}\right),\\ \hat{\varphi}_{\mathrm{R},k} &= \arcsin\left(\frac{\lambda_c}{d_{\mathrm{ant}}}\hat{v}_{\mathrm{R},k,s}\right),\end{aligned} \tag{3.28}$$

where λ_c is the wavelength of the carrier and d_{ant} is the spacing between antennas in the array. If the desired resolution is not achieved, s is incremented and the algorithm is started again from step 2.

3.3.3 TOA estimation

Once the fine estimates for the AOA and AOD are found for each path, the TOA can be estimated. The dictionary entry for each path saved in step 4 of the angle refinement algorithm, $\hat{\mathbf{\Omega}}[n] = \left[\hat{\boldsymbol{\omega}}_0[n],\ldots,\hat{\boldsymbol{\omega}}_{\hat{K}-1}[n]\right]$, is used for this. The recovered sparse dictionary matrix is QR factorized first. Thus,

$$\hat{\mathbf{\Omega}}[n] = \mathbf{Q}[n]\mathbf{R}[n]. \tag{3.29}$$

Using this, the estimate of the channel vector is found as follows,

$$\hat{\mathbf{h}}[n] = \mathbf{R}^{-1}[n]\tilde{\boldsymbol{\beta}}[n], \tag{3.30}$$

with

$$\tilde{\boldsymbol{\beta}}[n] = \left[\tilde{\beta}_0[n],\ldots,\tilde{\beta}_{\hat{K}-1}[n]\right], \tag{3.31}$$

and

$$\tilde{\beta}_k[n] = \frac{\hat{\boldsymbol{\omega}}_k^H[n]\mathbf{y}_\varphi[n]}{\left\|\hat{\boldsymbol{\omega}}_k^{(s)}[n]\right\|^2}. \tag{3.32}$$

Based on the channel model used in (3.2), the TOA for the kth path can be estimated as follows:

$$\hat{\tau}_k = \arg\max_{\tau_k}\left|\zeta^H(\tau_k)\hat{\mathbf{h}}_k\right|^2, \tag{3.33}$$

where

$$\zeta^H(\tau_k) = \left[1,\ldots,e^{-j2\pi(N-1)\tau_k/(NT_s)}\right]^T, \tag{3.34}$$

and

$$\hat{\mathbf{h}}_k = \left[\hat{h}_k[0],\ldots,\hat{h}_k[N-1]\right]^T. \tag{3.35}$$

The τ_k value can now be obtained by testing different values for τ_k. The value which maximizes the objective function is chosen as the the value for τ_k. It has to be noted that the TOA estimation requires some prior information about the TOA for the path. This is due to the objective function being periodic as it can be seen in Fig. 3.3. Thus, if a large range of τ_k values are searched for, there is a good chance

that an incorrect estimate for the TOA will be obtained. This puts a limitation on the application of this algorithm in outdoor scenarios.

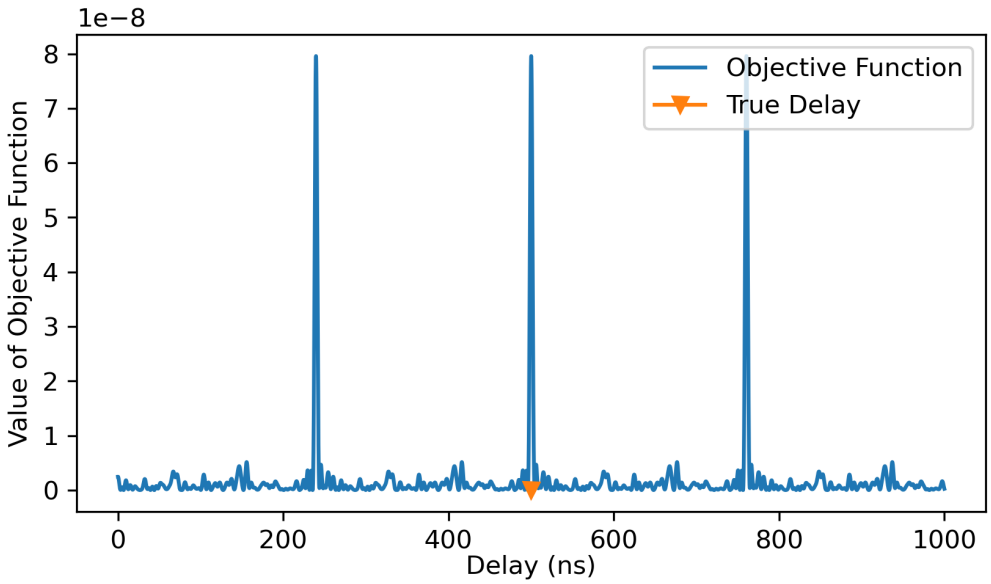

Figure 3.3. Plot showing the true value of the delay for a path and the value of the objective function for different values of time delay for use in TOA estimation.

3.3.4 Position/Orientation estimation

Due to the height of the antennas on the train, the RRHs and the limited curvature of the track to accommodate for the high-speeds of the train, there is always a LOS path between the train and the RRH. Thus, from the recovered paths, one is a LOS path and the rest are NLOS paths. In [6], the extended invariance principle (EXIP) algorithm is proposed for localization of the MT and to get the location of all the scatterers in such a scenario. Whereas in [7, 8], a Gibbs sampling based localization method is proposed. Both of these methods perform additional computations for getting the scatterer locations, which are not required for HST localization. Furthermore in [7, 8], samples from the distribution of the MT location and orientation are generated which is also additional computations which are not required. Part of the proposed algorithm in [6] could be used, whereby the path with the smallest TOA is taken as the LOS path and then used to obtain the location of the MT and the scatterers. The problem with this method is that in an outdoor environment, there can be ambiguities with the estimated TOA for each of the scatterers, leading to a scatterer being misclassified as a LOS path.

A much simpler method based on [56] can be used. Typically the LOS component will have a higher energy compared to NLOS components as the NLOS paths experience higher signal attenuation. This is especially the case in the HST scenario when the transmitted signals are beamformed towards the train. Thus, the component with the highest energy in beamspace will most likely be a LOS component. Based on this the very first component found by the algorithm, the component with the highest energy in beamspace, can be taken as the LOS component. This significantly reduces the number of computations that need to performed, as only the first component is processed. The position estimate for the train can be calculated as

$$\hat{\mathbf{p}} = \mathbf{q} + \hat{\tau}_0[\cos(\hat{\varphi}_{\mathrm{T},0}), \sin(\hat{\varphi}_{\mathrm{T},0})], \tag{3.36}$$

with $\mathbf{q}$ being the location of the RRH which is performing the localization. The orientation estimation depends whether the train is ahead of the RRH or behind the RRH. These two scenarios can be seen in Fig. 3.4. If the train is ahead of the RRH, the AOD in reference to the global axis is calculated as

$$\breve{\varphi}_{\mathrm{T}} = \hat{\varphi}_{\mathrm{T}} + \theta_{\mathrm{T}}. \tag{3.37}$$

It has to be noted that θ_{T} is defined as positive in the anti-clockwise direction. Using this, the orientation on the antenna array on the train is estimated as

$$\hat{\theta}_{\mathrm{R}} = \breve{\varphi}_{\mathrm{T}} + \hat{\varphi}_{\mathrm{R}}. \tag{3.38}$$

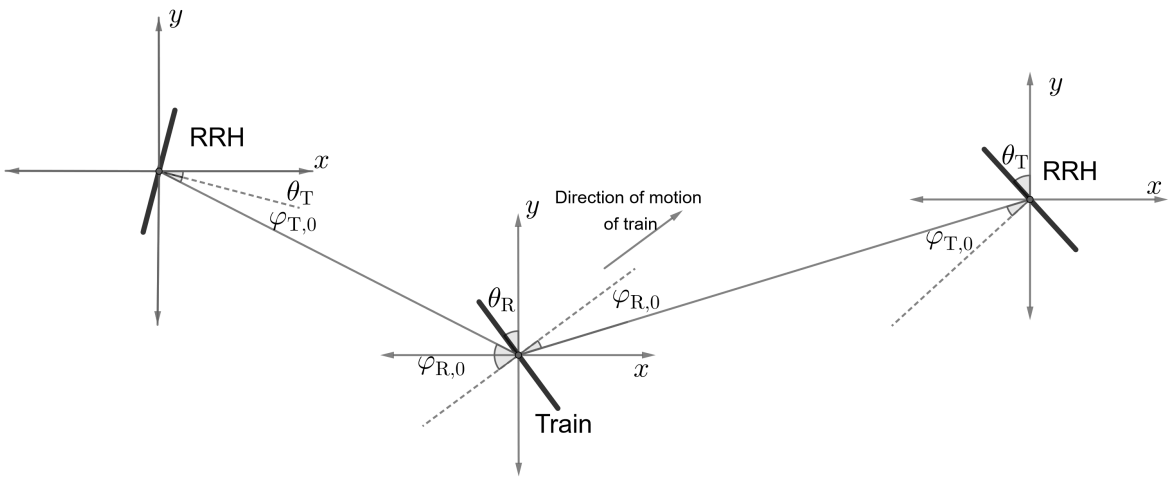

Figure 3.4. Diagram illustrating the two scenarios with the RRH being ahead or behind the train.

Similarly for the case of the train being behind the RRH, the AOD in terms of the global axis, with 0° being in the broadside direction, the orientation estimate are specified as

$$\breve{\varphi}_{\mathrm{T}} = \hat{\varphi}_{\mathrm{T}} - \theta_{\mathrm{T}}, \tag{3.39}$$

$$\hat{\theta}_{\mathrm{R}} = -\breve{\varphi}_{\mathrm{T}} - \hat{\varphi}_{\mathrm{R}}. \tag{3.40}$$

The proposed algorithm was tested in a stationery scenario to ensure that the algorithm can achieve the performance promised in [6–8]. The following simulation settings are used: $N_t = 32$, $N_r = 8$, $M = 32$ and $N = 64$. The M symbols are beamformed to uniformly spaced angles between $\pm\frac{\pi}{2}$. The BS is located at $(0,0)$ and the MT locations are picked from a uniformly random distribution between $(30,-50)$ and $(40,50)$. The MT orientation values are picked from a uniform random distribution between -0.35 and 0.35 rad. Three scatterers positioned at $(23,16)$, $(14,-21)$ and $(10,10)$ with a scattering loss of 6 dB. Furthermore, free space path loss is assumed. The simulation is run for a thousand different MT locations for SNR values between -26 to 34 dB in increments of 2 dB. Additionally outlier detection is performed on the estimates obtained in simulation, whereby AOA and AOD estimates that are more than 0.1 rad away from the true values for AOA and AOD are flagged as outliers and removed. This is also performed for TOA estimates, with estimates that are more than 10 ns further from the true TOA value are flagged as outliers and removed.

The results obtained from the simulation can be seen in Fig. 3.5. It is clear from localization error plot and the orientation error plot (Fig. 3.5(d) and Fig. 3.5(e)) that the proposed method can achieve sub-meter and sub-degree accuracy for SNR values as low as -10 dB. Furthermore, it can be seen that the AOD estimation error (Fig. 3.5(a)) affects the localization accuracy and the orientation estimation accuracy as well, as a similar trend is seen in all three. This is expected as the AOD is used in both the location estimation and also the orientation estimation. It can also be seen that the RMSE for the orientation estimate is approximately the sum of the error for AOA and the AOD estimates. This is expected as the orientation estimate combines the AOD and AOA estimates.

The localization and orientation estimation performance observed is much poorer compared to [7,8], as in [8] a localization accuracy of less than 10 cm is achieved for an SNR of -20 dB. The primary reason for the poor localization performance is that for many simulation runs, the first component extracted by the algorithm is not the LOS component leading to incorrect localization. Out of the 1000 MT locations, for 320 locations the estimates were flagged as outliers and removed. While the LOS component has a higher signal power compared to the NLOS components, in the initially defined

discrete beamspace the NLOS components could end up having a higher signal power due to grid mismatch. Grid mismatch refers to the phenomenon whereby when one of the components does not fall exactly onto one of the discrete points in the initially defined beamspace grid ((3.7) and (3.8)) and it spills into all the points on the grid. This is also referred to as power leakage [56] which is similar to the phenomenon of spectrum leakage in the frequency domain.

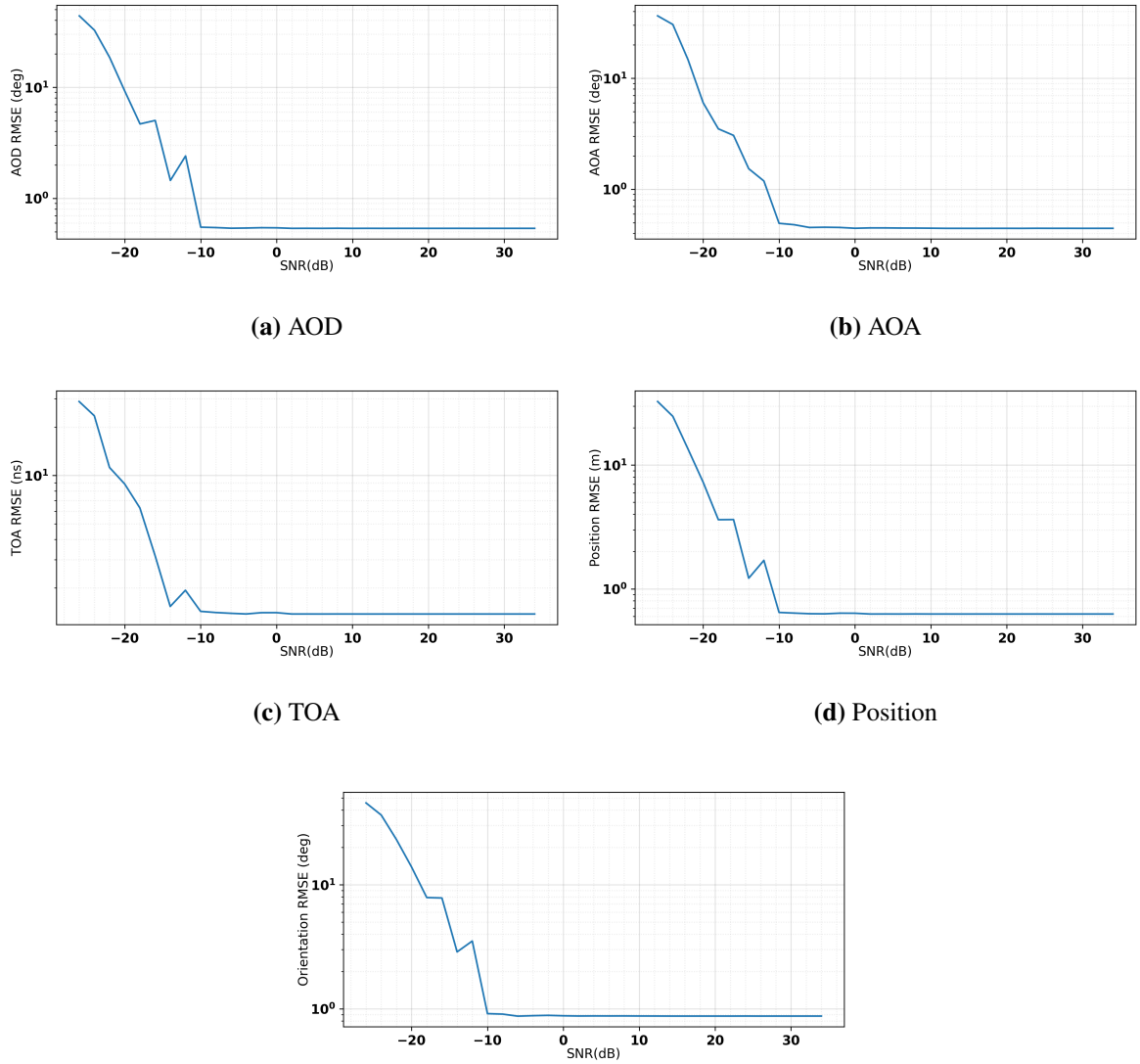

(a) AOD

(b) AOA

(c) TOA

(d) Position

(e) Orientation

Figure 3.5. The RMSE plots for the estimated parameters for various values of the SNR.

This effect of grid mismatch can be seen more clearly in Fig. 3.6. Here the BS location is fixed at (0,0) and the MT location is fixed at a distance of 100 m with its bearing varied from -1.396 rad to

1.396 rad in a 1000 uniformly spaced steps. Furthermore, no scatterers are present, meaning only a LOS path is present in the beamspace. The magnitude in (3.15) of the largest component found in the beamspace (which is the LOS component as there are no other components) is plotted for all the angles. It is expected that the magnitude will be constant for all angle values. However, it varies significantly as a result of grid mismatch. Beamforming in the direction of the MT can partly mitigate the misclassification of NLOS paths. However, this problem cannot completely be fixed unless all the components are recovered and the LOS path is selected.

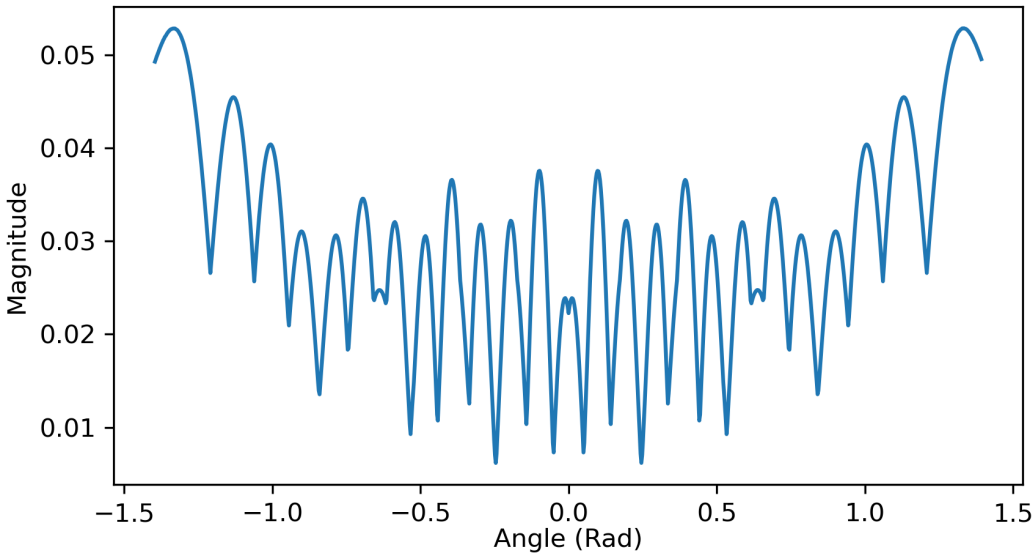

Figure 3.6. Plot showing how the magnitude of the recovered LOS component varies as the bearing of the MT changes.

3.4 THE DCS-SOMP ALGORITHM WITH LOS TRACKING

A way to solve the problem of the misclassification of the LOS path is through LOS tracking. As the HST is being tracked, there is some prior information available regarding where the train will be in each time step. Thus, prior information regrading where the LOS path is expected to be is available. This information can be incorporated into the measurement algorithm to ensure that the first component found by the algorithm is the LOS component. This is achieved by simply restricting the initial beam space to angles where the LOS path is expected to be. The lower and the upper bound for the AOA ($\hat{\varphi}_{\mathrm{R}}^{\mathrm{L}}$-$\hat{\varphi}_{\mathrm{R}}^{\mathrm{U}}$) and AOD ($\hat{\varphi}_{\mathrm{T}}^{\mathrm{L}}$-$\hat{\varphi}_{\mathrm{T}}^{\mathrm{U}}$) where the LOS is expected to be needs to first be converted to beamspace angles $\hat{\nu}_{\mathrm{R}}^{\mathrm{L}}$-$\hat{\nu}_{\mathrm{R}}^{\mathrm{U}}$ and $\hat{\nu}_{\mathrm{T}}^{\mathrm{L}}$-$\hat{\nu}_{\mathrm{T}}^{\mathrm{U}}$. The beamspace angles are calculated using the inverse of (3.28).

Thus,

$$\hat{v} = \frac{d_{ant}}{\lambda_c} \sin \hat{\varphi}. \tag{3.41}$$

Using these limits, the transformation matrices are defined with Q equally spaced angles between the limits for both AOA and AOD. Thus the new $\mathbf{U}_{\mathrm{T}}$, and similarly the new $\mathbf{U}_{\mathrm{R}}$, is defined as

$$\mathbf{U}_{\mathrm{T}} = \left[\mathbf{u}_{\mathrm{T}} \left(v_{\mathrm{T},1}^{(1)} \right), \ldots, \mathbf{u}_{\mathrm{T}} \left(v_{\mathrm{T},1}^{(Q)} \right) \right], \tag{3.42}$$

with

$$v_{\mathrm{T},1}^{(l)} = \hat{v}_{\mathrm{T}}^{\mathrm{L}} + l * \Delta v_{\mathrm{T}}. \tag{3.43}$$

The beamspace resolution is now Δv_{R} for the AOA and Δv_{T} for the AOD. These are defined as

$$\Delta v_{\mathrm{R}} = \frac{\hat{v}_{\mathrm{R}}^{\mathrm{U}} - \hat{v}_{\mathrm{R}}^{\mathrm{L}}}{Q}, \tag{3.44}$$

and

$$\Delta v_{\mathrm{T}} = \frac{\hat{v}_{\mathrm{T}}^{\mathrm{U}} - \hat{v}_{\mathrm{T}}^{\mathrm{L}}}{Q}. \tag{3.45}$$

The transformation matrices are used to define the sensing/dictionary matrix using (3.13). The algorithm from the previous section can now be modified to get fine estimates for the AOD and AOA for the LOS path from the defined dictionary as follows:

1. Set the iteration index s to 1. Set the AOA resolution, $\kappa_{\mathrm{T},0}$, and the AOD resolution, $\kappa_{\mathrm{R},0}$, to Δv_{T} and Δv_{R} respectively. Furthermore, the dictionary length variable p is set to Q.
2. The basis created by AOA/AOD pair in the dictionary onto which the projection of $\mathbf{y}_{\varphi}$ is the largest is chosen as AOA and AOD for the LOS path. Equation 3.15 is used for this.
3. The dictionary matrix column index, q_s, is used to obtain the corresponding AOA and AOD in the transformation matrix as follows:

   $$q_{\mathrm{T},s} = \left\lceil \frac{q_s}{p} \right\rceil \tag{3.46}$$

   and

   $$q_{\mathrm{R},s} = \mathrm{mod}\left(q_s, p\right). \tag{3.47}$$

   The AOD and AOA estimate in beamspace domain is thus

   $$\hat{v}_{\mathrm{T},s} = v_{\mathrm{T},s}^{(q_{\mathrm{T},s})}, \tag{3.48}$$

   and

   $$\hat{v}_{\mathrm{R},s} = v_{\mathrm{R},s}^{(q_{\mathrm{R},s})}. \tag{3.49}$$

   The column of $\mathbf{\Omega}[n]$ that corresponds to index q_s is saved as $\hat{\boldsymbol{\omega}}_0[n]$ for use in the TOA estimation process.

4. If the desired resolution for the AOA and the AOD has been achieved, the algorithm is concluded and the AOD and AOA obtained are converted from beamspace angles to real angles in radians using (3.28). If the desired resolution is not met, the iteration index s is incremented and the transformation matrices are redefined around the AOA and AOD of the current iteration but now the beamspace resolution is doubled ($\kappa_{\mathrm{T},s} = \kappa_{\mathrm{T},s-1}/2$). Thus $\mathbf{U}_{\mathrm{T},s}$ and similarly $\mathbf{U}_{\mathrm{R},s}$, is defined as

$$\mathbf{U}_{\mathrm{T},s} = \left[\mathbf{u}_{\mathrm{T}}\left(\nu_{\mathrm{T},s}^{(0)}\right), \ldots, \mathbf{u}_{\mathrm{T}}\left(\nu_{\mathrm{T},s}^{(10)}\right)\right], \tag{3.50}$$

whereby

$$\nu_{\mathrm{T},s}^{(l)} = \hat{\nu}_{\mathrm{T},s-1} - 2\kappa_{\mathrm{T},s-1} + l\kappa_{\mathrm{T},s} \tag{3.51}$$

and p is set to ten. The new transformation matrices are then used to define the sensing matrix $\mathbf{\Omega}[n]$ using (3.13) and the algorithm is restarted from Step 2.

This is followed by TOA estimation using the method discussed in the previous section.

The proposed algorithm was tested in the same simulation scenario as described in the previous section in order to compare it to the original algorithm. As a stationery scenario is considered, the MT location is not tracked, so prior information regarding the MT location is not available. The initial beamspace for both AOA and AOD is therefore restricted to ± 0.1 rad around the true value AOA and AOD of the LOS component. The estimation error for the channel parameters can be seen in Fig. 3.7. With the restricted beamspace, the estimation performance improves for TOA estimation and position estimation. Similar performance as the original method is seen in the AOD estimation, whereas the AOD estimation and the orientation estimation performance degrades. An important thing to remember when looking at these plots is that for the original method out of the 1000 MT location 320 locations were flagged as outliers removed from the RMSE calculation, whereas with the LOS tracking there were no outliers. Thus, with the LOS tracking similar performance as the original algorithm but with a reduced chance of LOS misclassification. Furthermore, the LOS tracking performs better for low SNR values compared to the original algorithm.

3.5 LOCALIZATION PERFORMANCE FOR VARIOUS PARAMETER VALUES

In order to determine the effect of various system parameters (N_t, N_r, M and N) on the localization performance, the algorithm is tested in the simulation scenario mentioned in the previous section with each system parameter varied. The system parameters are varied from 4 to 64 in powers of 2. The

parameters not being varied are all set to 32. The error plots for these are shown in the sub-sections below.

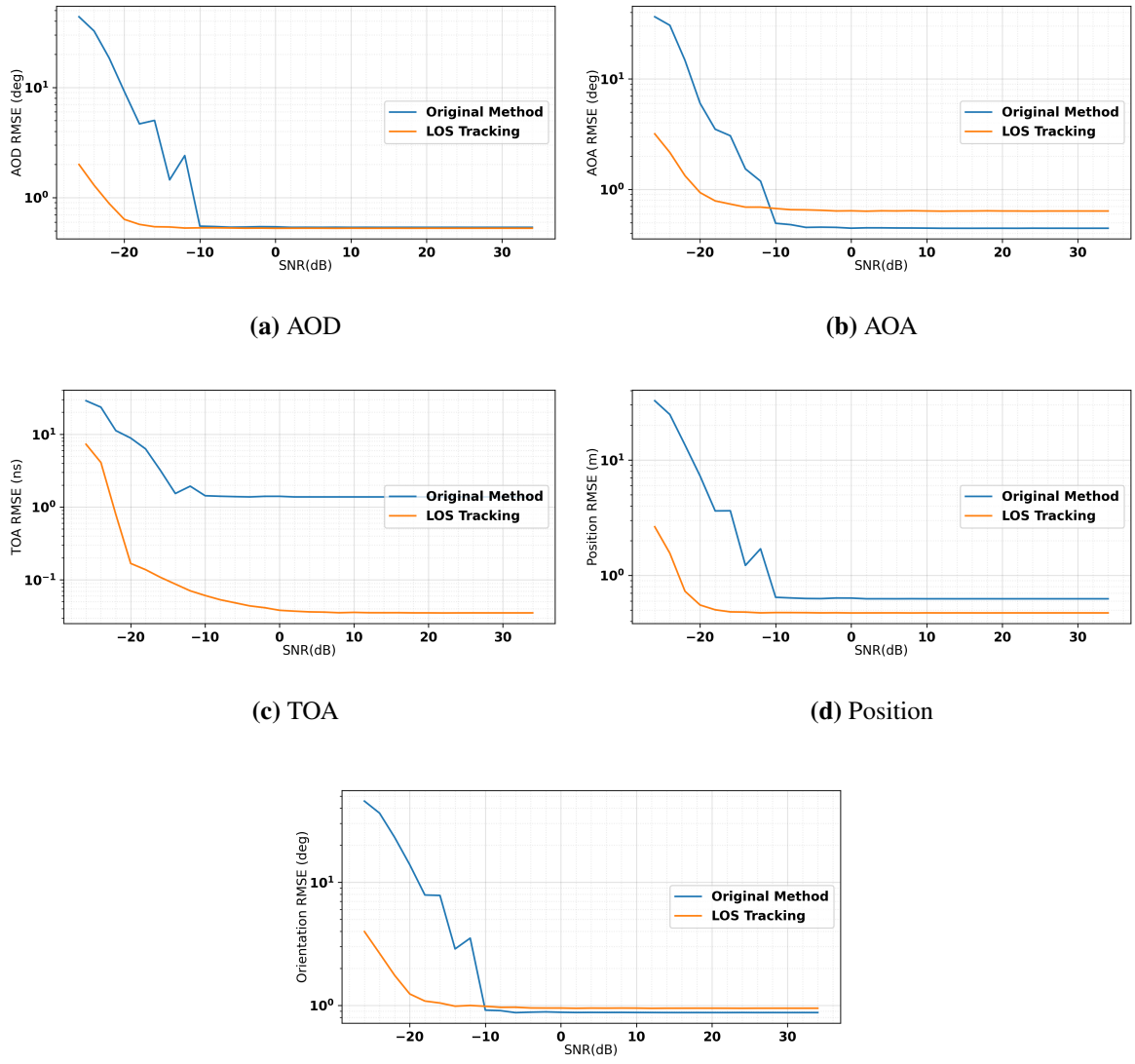

(a) AOD

(b) AOA

(c) TOA

(d) Position

(e) Orientation

Figure 3.7. The RMSE plots for the estimated parameters for various values of the SNR when using the original method and the LOS tracking method.

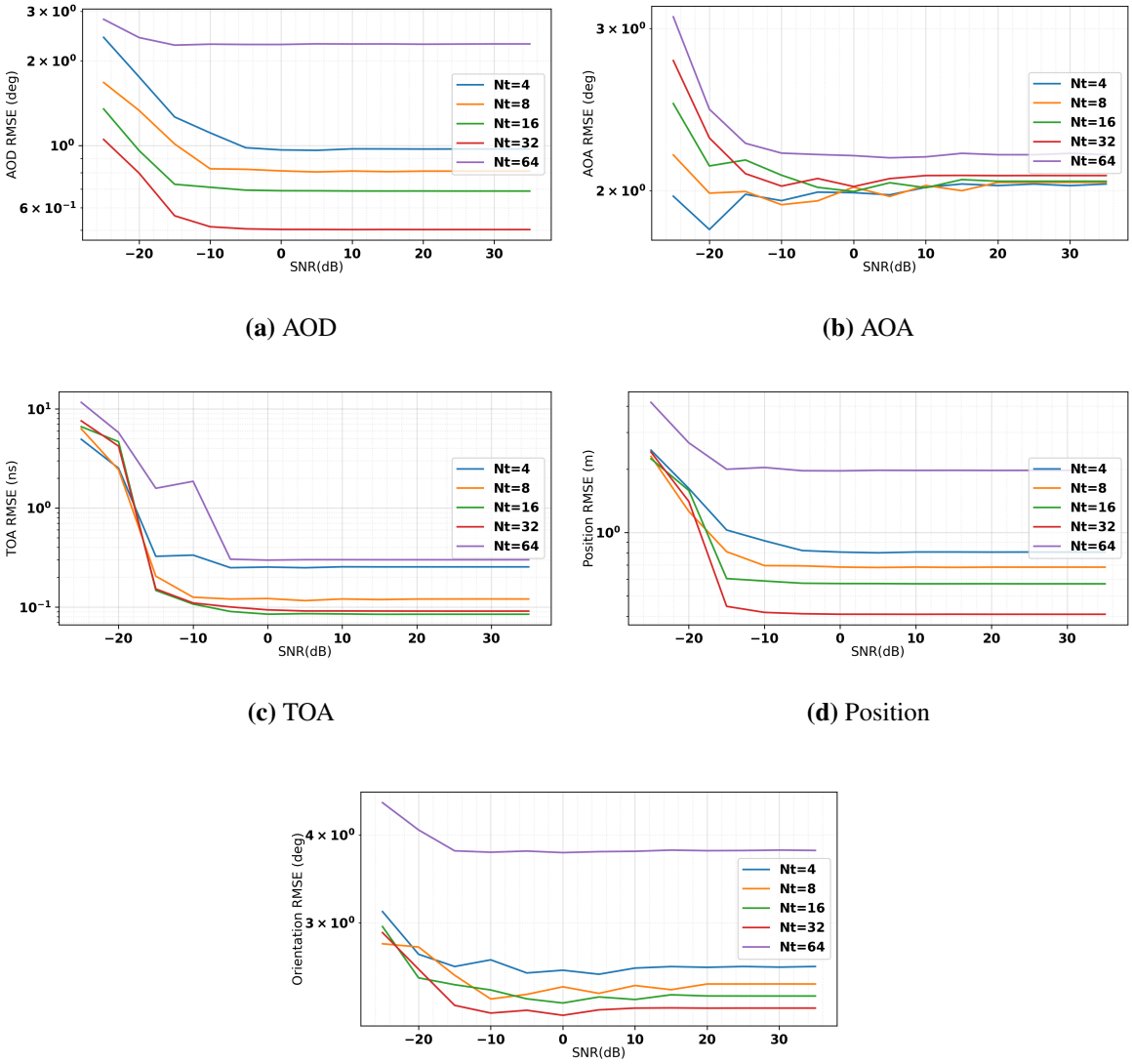

(a) AOD

(b) AOA

(c) TOA

(d) Position

(e) Orientation

Figure 3.8. The RMSE plots for the estimated parameters for various values of transmit antennas used for SNR values from -25 dB to 35 dB.

3.5.1 Varying the Transmit antennas

The error plots for various values of N_t can be seen in Fig. 3.8 below. It can be seen that the number of transmit antennas used primarily affect the AOD estimation and the TOA estimation. Consequently, the position estimation is also affected. The AOA estimation and the orientation estimation are not significantly affected by the number of transmit antennas used. The general trend here is an improvement in estimation accuracy from $N_t = 4$ to $N_t = 32$, which is followed by a significant

degradation in performance at $N_t = 64$. Increasing the number of antennas leads to narrower beams. Thus, the spatial correlation between different beams is reduced [6] and the AOD estimation improves. The narrower beams do have a drawback as the chances of the MT receiving coverage decreases. This leads to performance degradation as seen in $N_t = 64$. Overall the algorithm can achieve sub-meter localization accuracy using the 4 transmit antennas. However, sub-degree orientation estimation accuracy is not achieved.

3.5.2 Varying the Receive antennas

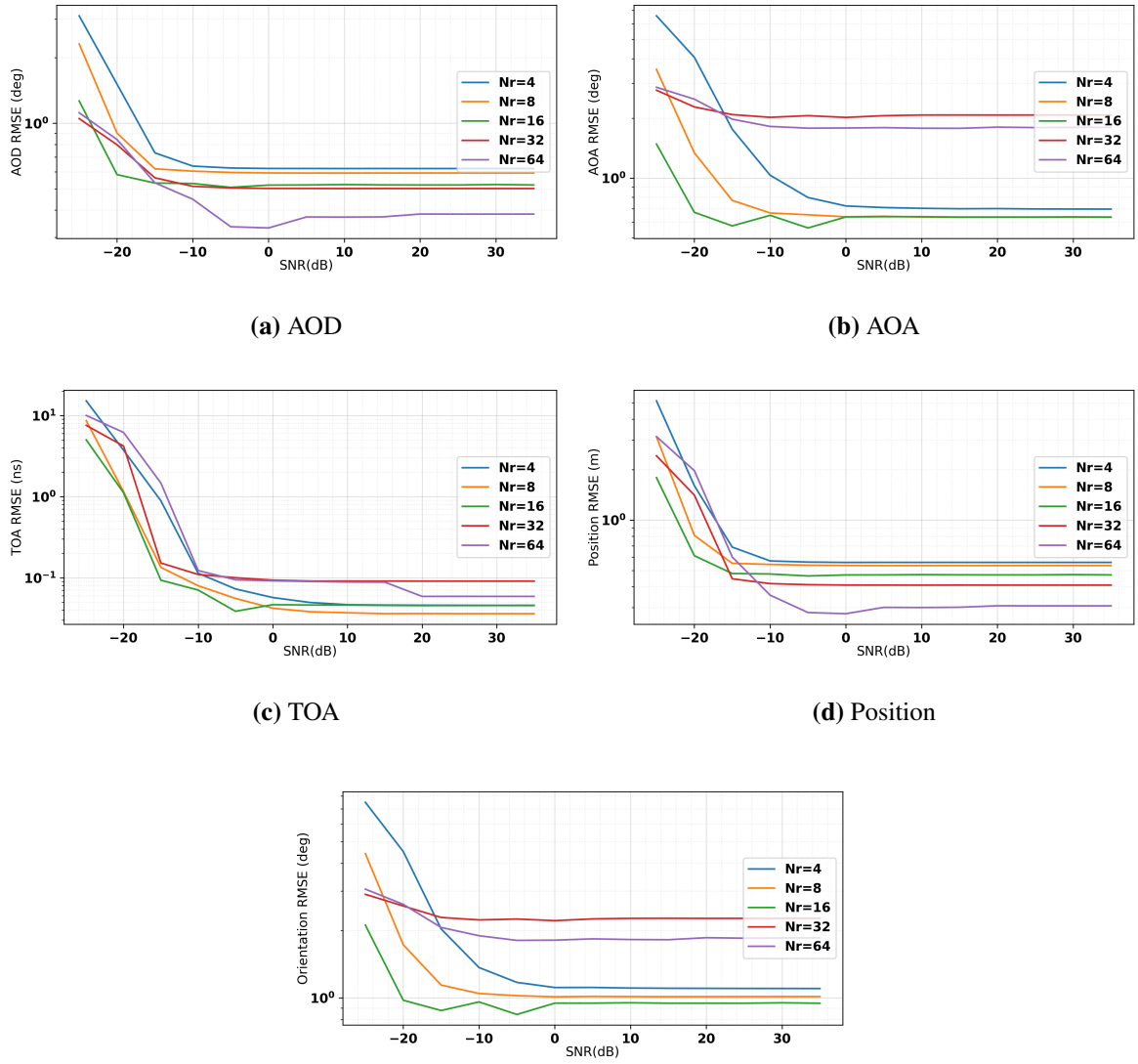

(a) AOD

(b) AOA

(c) TOA

(d) Position

(e) Orientation

Figure 3.9. The RMSE plots for the estimated parameters for various values of receive antennas used for SNR values from -25 dB to 35 dB.

Fig. 3.9 shows the estimation error for the algorithm for different number of antennas used at the MT. The number of antennas at the receiver marginally affect the AOD, TOA and localization estimation whereas the AOA and the orientation estimation are more significantly affected. The AOD and the location estimation improve marginally as the number of receive antennas increase. For the AOA, TOA and the orientation estimation the performance increased for $N_r = 4$ to $N_r = 16$. At $N_r = 32$ the

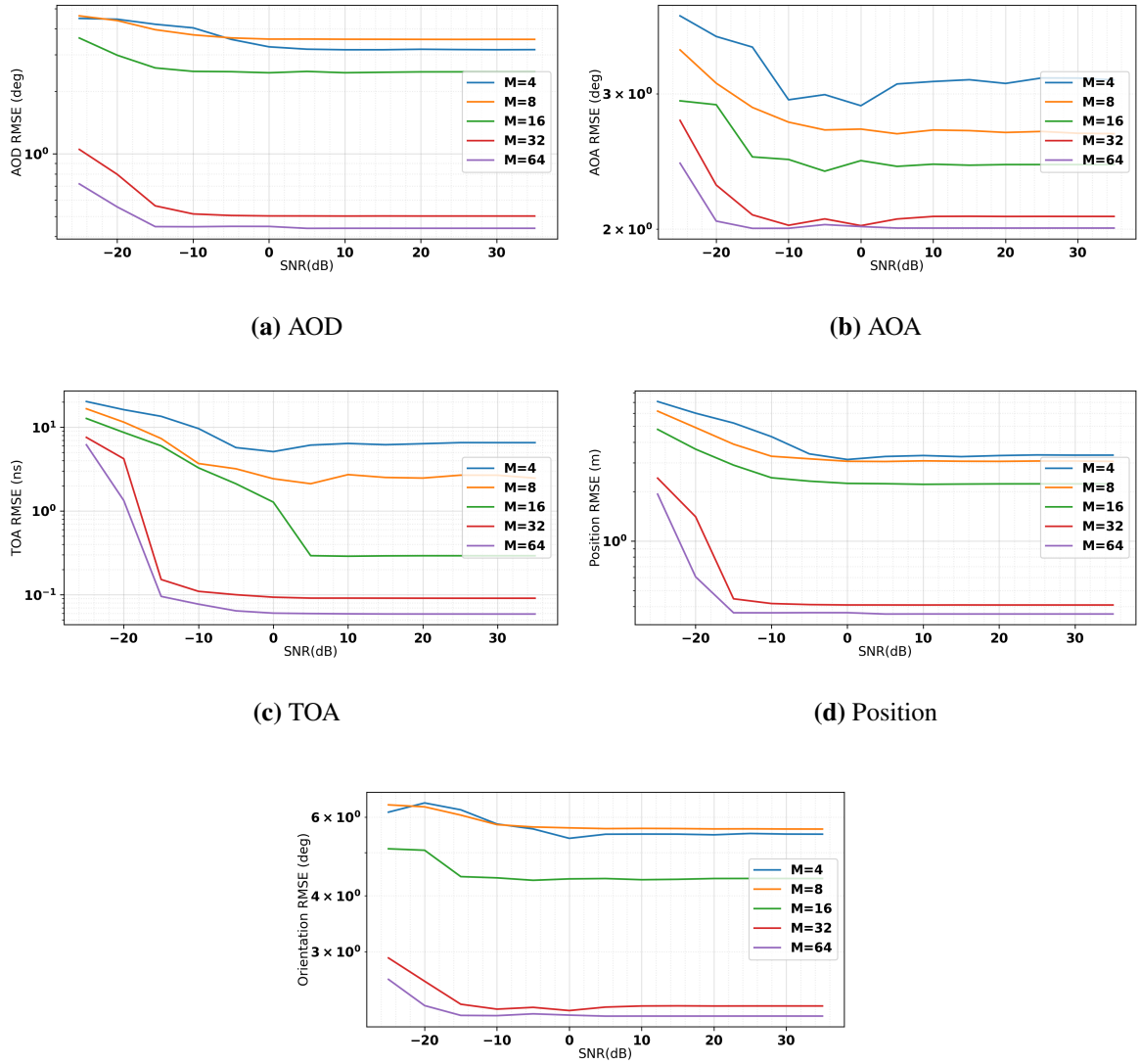

(a) AOD

(b) AOA

(c) TOA

(d) Position

(e) Orientation

Figure 3.10. The RMSE plots for the estimated parameters for various values of symbol (M) used in localization for SNR values from -25 dB to 35 dB.

performance degrades with slight improvement for $N_r = 64$. Increasing the number of antennas leads

to the scalar product between the steering vectors for different directions diminishing, which leads to a higher resolution in beamspace. This results in an improvement in estimation accuracy for all parameters. However, with a higher resolution, multipath components are more distinguishable. Thus there is a higher chance that in the restricted beamspace, the channel parameters for a NLOS component are computed instead of the LOS component. This results in poorer performance as seen for $N_r = 32$ and $N_r = 64$. Regardless, sub-meter localization accuracy is achievable with just 4 antennas at the receiver, whereas sub-degree orientation estimation accuracy is achievable with $N_r = 8$ and $N_r = 16$.

3.5.3 Varying the number of symbols

The estimation error plots for different number of symbols used can be seen in Fig. 3.10. Varying the number of symbols used by the algorithm has a significant effect on the estimation accuracy for all parameters. The general trend is that increasing the number of symbols used leads to an increase in estimation performance. The reason for this is that with more symbols transmitted there is a higher chance that the MT will get coverage. The estimation performance is poor for $M < 32$. However, for $M \geq 32$ sub-meter localization accuracy is achieved. Sub-degree accuracy for orientation estimation is not achieved regardless of the number of symbols used. This is primarily due to the algorithm using 32 receive antennas.

3.5.4 Varying the number of carriers

Fig. 3.11 shows the estimation error plots for varying values for the sub-carriers used by the algorithm. The number of carriers used primarily affect the TOA estimation. Consequently, the location estimation is affected. The other parameters are not significantly affected. This occurs due to the resolution of the objective function in (3.33) increasing as the number of carriers used increase, leading to more accurate TOA estimation. Sub-meter localization accuracy is achievable using only 16 carriers. However, sub-degree estimation accuracy is not achieved. Similar to the test for M, this is attributed to 32 receive antennas being used.

3.6 CONCLUDING REMARKS

This chapter discusses a compressed sensing based 5G localization algorithm. The algorithm makes use of the DCS-SOMP algorithm to decompose the sparse mmWave channel into LOS components and NLOS components. The measurements from LOS component can be used to localize the MT and estimate its orientation. It is shown that this algorithm incorrectly classifies the NLOS components as a LOS component frequently, leading to inaccurate localization. A way to avoid this problem is

by restricting the initial beamspace to limits where the LOS path is expected to be, this fixes the misclassification problem. It is also shown that the algorithm can achieve sub-meter localization accuracy for various system parameters. The next chapter discusses the tracking algorithm.

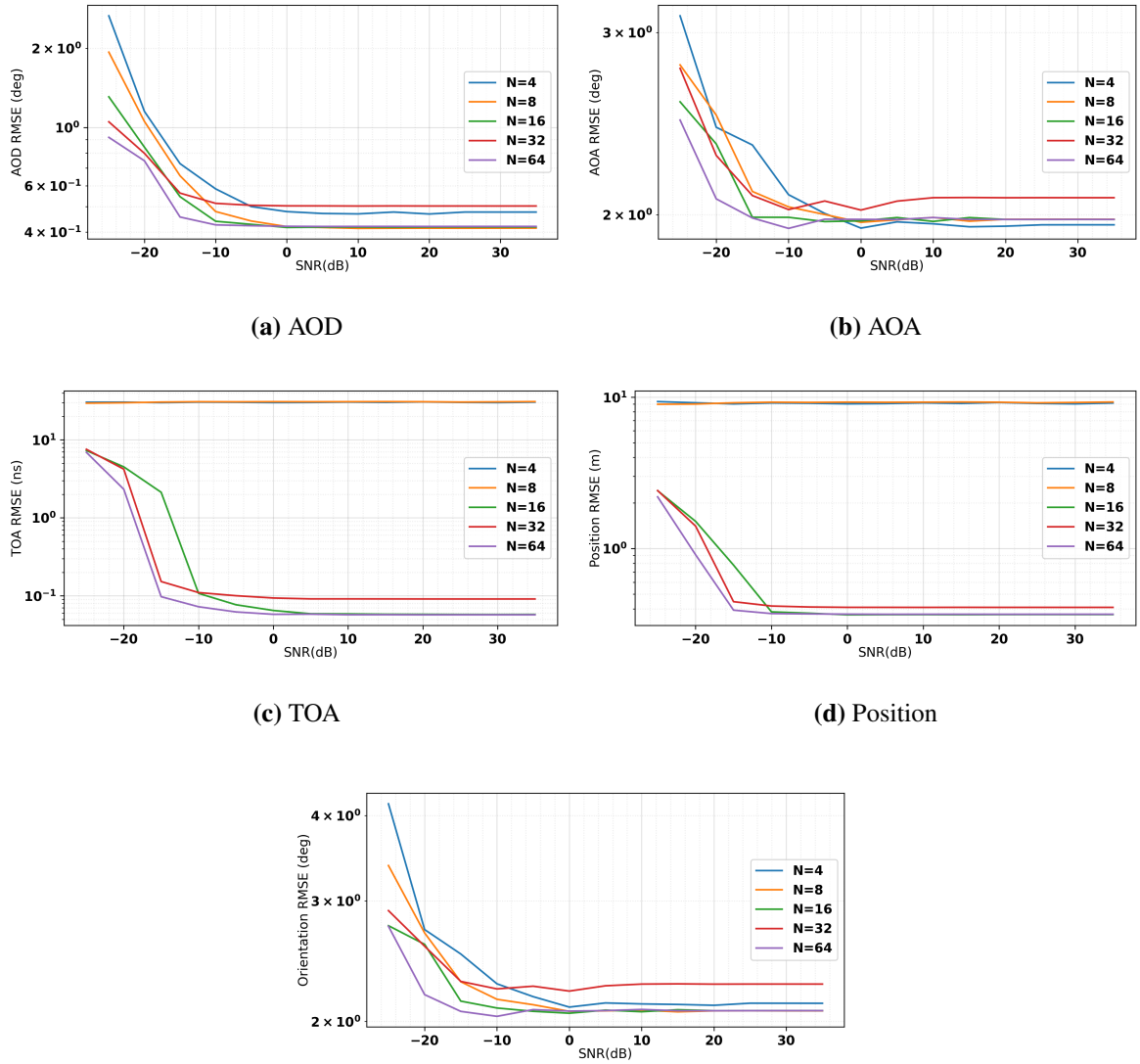

(a) AOD

(b) AOA

(c) TOA

(d) Position

(e) Orientation

Figure 3.11. The RMSE plots for the estimated parameters for a range of carriers (N) used in localization for SNR values from -25 dB to 35 dB.

CHAPTER 4 THE EXTENDED KALMAN FILTER

4.1 INTRODUCTION

Several different tracking algorithms have been used for tracking HST in literature, as discussed in Section 2.2. The following algorithms are most widely used: the EKF, the FKF, particle filter, RBPF, SLAM RBPF and simple map matching. In 5G localization and tracking systems on the other hand, an EKF is typically used, due to it being computationally cheaper.

The particle filter undoubtedly offers the best performance as it is flexible enough to accommodate for any arbitrary distribution. Furthermore, particle filter implementations typically allow for the incorporation of map data, which greatly improves tracking performance as the kinematics of the train are restricted by the tracks. There are some caveats to this algorithm. Map data is not always available and maps are often not very accurate. The SLAM RBPF algorithm addresses this problem by using probabilistic map data which is updated every time the train uses a particular part of the map or uses a route that is not mapped. However, for any map based tracking to work with 5G localization, 5G infrastructure has to interface with rail infrastructure. Thus, making it impractical to use. Another disadvantage of this algorithm is that it is computationally expensive. This is partly addressed by the RBPF. However, it is still too computationally expensive to use with low latency 5G localization.

Map matching performs very poorly and suffers the same drawbacks as map based particle filter algorithms. The EKF and FKF are therefore the most viable solution for this application. From the two algorithms, the EKF is more widely used compared to the FKF in both tracking HSTs and for general 5G localization and tracking. Thus, making it the preferred option for this use case.

The rest of this chapter is structured as follows: In Section 4.2, the theory behind the EKF is discussed.

This is followed by a discussion of the EKF implementation for use with the compressed sensing based 5G localization algorithm in Section 4.3. Lastly, in Section 4.4, concluding remarks are made.

It has to be noted that some symbols used in the previous chapter are reused in this chapter; however, they do not represent the same quantities and are redefined in this chapter.

4.2 THEORETICAL BACKGROUND

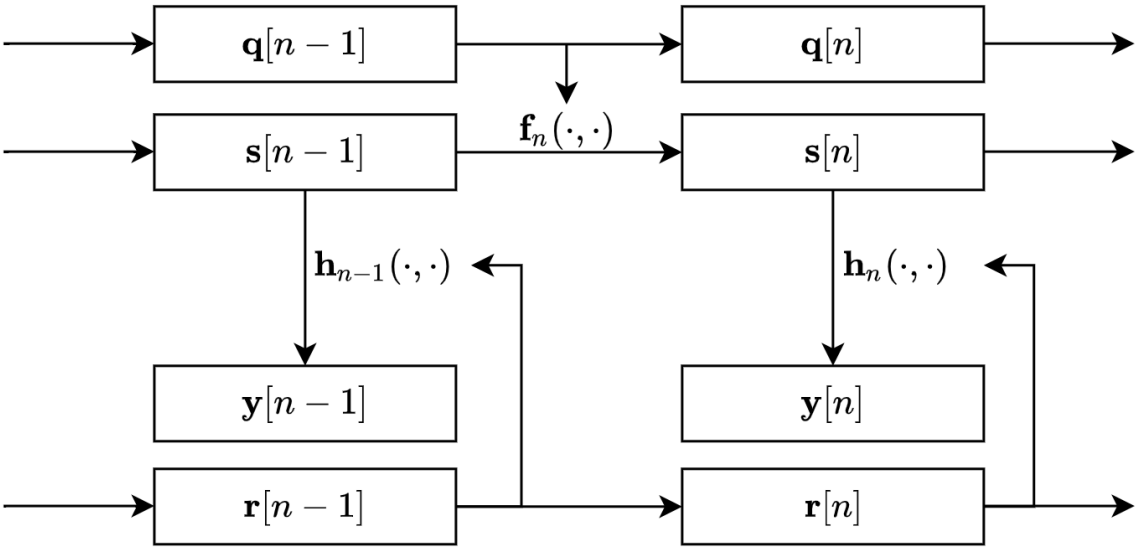

Figure 4.1. Diagram illustrating a typical system in which recursive Bayesian estimation is used.

The Kalman filter is special case of a recursive Bayesian Filter. The typical system in which recursive Bayesian filtering is applied can be seen in Fig. 4.1. Here the state evolution is specified by

$$\mathbf{s}[n] = \mathbf{f}_n(\mathbf{s}[n-1], \mathbf{q}[n-1]), \tag{4.1}$$

where $\mathbf{f}_n(\cdot,\cdot)$ is the linear or non-linear state transition function and $\mathbf{q}$ is an i.i.d process noise sequence [57]. The aim of the filtering is to recursively estimate $\mathbf{s}[n]$ from measurements

$$\mathbf{y}[n] = \mathbf{h}_n(\mathbf{s}[n], \mathbf{r}[n]), \tag{4.2}$$

where $\mathbf{h}_n(\cdot,\cdot)$ is the linear or non-linear measurement function and $\mathbf{r}$ is an i.i.d measurement noise sequence. In a Bayesian sense, the probability distribution of $\mathbf{s}[n]$ being some value, given observations $\mathbf{y}[1:n]$, needs to be estimated. Assuming the prior distribution $p(\mathbf{s}[0])$ is known, the posterior distribution, $p(\mathbf{s}[n] \mid \mathbf{y}[1:n])$, can be estimated recursively through a prediction and a update stage. Assuming $p(\mathbf{s}[n] \mid \mathbf{s}[n-1], \mathbf{y}[0:n-1]) = p(\mathbf{s}[n] \mid \mathbf{s}[n-1])$ from (4.1) and that $p(\mathbf{s}[n-1] \mid \mathbf{y}[1:n-1])$

is available from the previous time step, the prior distribution for $\mathbf{s}$ for the nth step is specified as

$$p(\mathbf{s}[n] \mid \mathbf{y}[1:n-1]) = \int p(\mathbf{s}[n] \mid \mathbf{s}[n-1])\, p(\mathbf{s}[n-1] \mid \mathbf{y}[1:n-1])\, d\mathbf{s}[n-1]. \tag{4.3}$$

This is the prediction step. Here, $p(\mathbf{s}[n] \mid \mathbf{s}[n-1])$ is specified by the system model and the known distribution of the process noise. As the measurement for the nth time step becomes available, the prior can be updated using Bayes rule as

$$p(\mathbf{s}[n] \mid \mathbf{y}[1:n]) = \frac{p(\mathbf{y}[n] \mid \mathbf{s}[n])\, p(\mathbf{s}[n] \mid \mathbf{y}[1:n-1])}{p(\mathbf{y}[n] \mid \mathbf{y}[1:n-1])} \propto p(\mathbf{y}[n] \mid \mathbf{s}[n])\, p(\mathbf{s}[n] \mid \mathbf{y}[1:n-1]). \tag{4.4}$$

The denominator is constant relative to $\mathbf{s}$ thus it can be ignored, and the numerator can be normalized as is should sum to unity. The calculated posterior distribution can now be used to compute the prediction for the next step [57]. In the case of the process noise and the measurement noise being zero mean additive white Gaussian noise where and $\mathbf{f}(.)$ and $\mathbf{h}(.)$ are linear functions, the recursive Bayesian filter reduces to a Kalman filter. The system model and the measurement model can be rewritten as

$$\mathbf{s}[n] = F[n]\mathbf{s}[n-1] + \mathbf{q}[n-1], \tag{4.5}$$

$$\mathbf{y}[n] = H[n]\mathbf{s}[n] + \mathbf{r}[n], \tag{4.6}$$

where $F[k]$ is the state transition matrix, $H[n]$ is the measurement matrix and $\mathbf{q}[n-1]$ and $\mathbf{r}[n]$ are zero mean Gaussian noise with a covariance of $Q[n-1]$ and $R[n]$ respectively. The probability densities discussed previously in the recursive Bayesian computation are all Gaussian and are specified as

$$p(\mathbf{s}[n-1] \mid \mathbf{y}[1:n-1]) = \mathcal{N}\left(\mathbf{s}[n-1]; \bar{\mathbf{s}}^{+}[n-1], P^{+}[n-1]\right), \tag{4.7}$$

$$p(\mathbf{s}[n] \mid \mathbf{y}[1:n-1]) = \mathcal{N}\left(\mathbf{s}[n]; \bar{\mathbf{s}}^{-}[n], P^{-}[n]\right), \tag{4.8}$$

$$p(\mathbf{s}[n] \mid \mathbf{y}[1:n]) = \mathcal{N}\left(\mathbf{s}[n]; \bar{\mathbf{s}}^{+}[n], P^{+}[n]\right). \tag{4.9}$$

The means, $\bar{s}$, and the covariance matrices, P, are specified as

$$\bar{\mathbf{s}}^{-}[n] = F[n]\bar{\mathbf{s}}^{+}[n-1], \tag{4.10}$$

$$P^{-}[n] = F[n]P^{+}[n-1]F[n]^{T} + Q[n-1], \tag{4.11}$$

$$\bar{\mathbf{s}}^{+}[n] = \bar{\mathbf{s}}^{-}[n] + K[n]\left(\mathbf{y}[n] - H[n]\bar{\mathbf{s}}^{-}[n]\right), \tag{4.12}$$

$$P^{+}[n] = P^{-}[n] - K[n]H[n]P^{-}[n]. \tag{4.13}$$

Here $K[n]$ refers to the Kalman gain which is defined by

$$K[n] = P^{-}[n]H[n]^{T}S[n]^{-1}, \tag{4.14}$$

with

$$S[n] = H[n]P^{-}[n]H[n]^{T} + R[n]. \tag{4.15}$$

This is the optimal solution for the estimation of the posterior probability. The simplification of the calculation in (4.3) and (4.4) is possible due the simple rules that dictate how the mean and the covariance of the Gaussian distribution are effected by linear operations. However, it is often the case

that the system model or the measurement function is non-linear. In such a case an optimal solution is not possible. However, a sub-optimal solution, referred to as the Extended Kalman Filter (EKF), can be used. Thus,

$$p\left(\mathbf{s}[n-1] \mid \mathbf{y}[1:n-1]\right) \approx \mathcal{N}\left(\mathbf{s}[n-1]; \bar{\mathbf{s}}^{+}[n-1], P^{+}[n-1]\right), \tag{4.16}$$

$$p\left(\mathbf{s}[n] \mid \mathbf{y}[1:n-1]\right) \approx \mathcal{N}\left(\mathbf{s}[n]; \bar{\mathbf{s}}^{-}[n], P^{-}[n]\right), \tag{4.17}$$

$$p\left(\mathbf{s}[n] \mid \mathbf{y}[1:n]\right) \approx \mathcal{N}\left(\mathbf{s}[n]; \bar{\mathbf{s}}^{+}[n], P^{+}[n]\right). \tag{4.18}$$

The mean and the covariance matrices are specified similar to the Kalman filter with minor differences

$$\bar{\mathbf{s}}^{-}[n] = \mathbf{f}_n(\bar{\mathbf{s}}^{+}[n-1]), \tag{4.19}$$

$$P^{-}[n] = \hat{F}[n]P^{+}[n-1]\hat{F}[n]^{T} + Q[n-1], \tag{4.20}$$

$$\bar{\mathbf{s}}^{+}[n] = \bar{\mathbf{s}}^{-}[n] + K[n]\left(\mathbf{y}[n] - \mathbf{h}_n(\bar{\mathbf{s}}^{-}[n])\right), \tag{4.21}$$

$$P^{+}[n] = P^{-}[n] - K[n]\hat{H}[n]P^{-}[n]. \tag{4.22}$$

The Kalman gain is given by

$$K[n] = P^{-}[n]\hat{H}[n]^{T}S[n]^{-1}, \tag{4.23}$$

with

$$S[n] = \hat{H}[n]P^{-}[n]\hat{H}[n]^{T} + R[n]. \tag{4.24}$$

Furthermore, $\hat{H}[n]$ and $\hat{F}[n]$ are the linearizations of the non-linear functions $\mathbf{h}_n(.)$ and $\mathbf{f}_n(.)$ around the mean values using a first-order Taylor series expansion. Thus they are defined as

$$\hat{F}[n] = \left.\frac{d\mathbf{f}_n(x)}{dx}\right|_{x=\bar{s}^{+}[n-1]}, \tag{4.25}$$

$$\hat{H}[n] = \left.\frac{d\mathbf{h}_n(x)}{dx}\right|_{x=\bar{s}^{-}[n]}. \tag{4.26}$$

4.3 IMPLEMENTATION

In majority of the existing 5G localization based HST tracking systems in literature [2–4], a linear state transition model based EKF is used. However, in [5], a non-linear state transition model is proposed and shown to provide an improvement in performance compared to a linear state transition model. Thus, a non-linear state transition based EKF is used.

EKF based on the coordinated turn model from [58] using polar velocity is proposed in [5]. The proposed algorithm uses AOA and TDOA measurements from each RRH. It is modified here to use AOD, TOA and train orientation measurements instead. The state space is defined as

$$\mathbf{s}[n] = [x[n], y[n], v[n], h[n]]^{\mathrm{T}} \in \mathbb{R}^{4\times 1}, \tag{4.27}$$

whereby n refers to the time-step, (x,y) refers to the coordinates of the train, v is the polar velocity of the train and h is the heading direction. Based on this, the system model is given by

$$\mathbf{s}[n] = \mathbf{f}(\mathbf{s}[n-1]) + \mathbf{q}[n], \tag{4.28}$$

where $\mathbf{f}(.)$ is the non-linear state transition function and $\mathbf{q}[n] \sim \mathcal{N}(0, \mathbf{Q}[n])$ is the zero mean Gaussian process noise. The non-linear state transition function is defined as

$$\mathbf{f}(\mathbf{s}[n-1]) = \begin{bmatrix} x[n-1] + \Delta t v[n-1]\cos(h[n-1]) \\ y[n-1] + \Delta t v[n-1]\sin(h[n-1]) \\ v[n-1] \\ h[n-1] \end{bmatrix}, \tag{4.29}$$

with Δt being the difference between time steps. Based on the system model, the equations to obtain a prediction of the mean ($\hat{\mathbf{s}}^-[n]$) and the covariance ($\hat{\mathbf{P}}^-[n]$) for the current time step based on the values from the previous time step are

$$\hat{\mathbf{s}}^-[n] = \mathbf{f}\left(\hat{\mathbf{s}}^+[n-1]\right), \tag{4.30}$$

$$\hat{\mathbf{P}}^-[n] = \mathbf{F}[n]\hat{\mathbf{P}}^+[n-1]\mathbf{F}[n]^{\mathrm{T}} + \mathbf{Q}[n], \tag{4.31}$$

where $\mathbf{Q}[n]$ is the covariance matrix of the process noise and $\mathbf{F}[n]$ refers to the Jacobian matrix of the function $\mathbf{f}(.)$. The Jacobian matrix $\mathbf{F}[n]$ is defined as

$$\mathbf{F}[n] = \begin{bmatrix} \mathbf{I}_{2\times 2} & \Delta t \cdot \tilde{\mathbf{F}}[n] \\ \mathbf{0}_{2\times 2} & \mathbf{I}_{2\times 2} \end{bmatrix}, \tag{4.32}$$

where $\tilde{\mathbf{F}}[n] \in \mathbb{R}^{2\times 2}$ is given by

$$\tilde{\mathbf{F}}[n] = \begin{bmatrix} \cos\left(\hat{h}^+[n-1]\right) & -\hat{v}^+[n-1]\sin\left(\hat{h}^+[n-1]\right) \\ \sin\left(\hat{h}^+[n-1]\right) & \hat{v}^+[n-1]\cos\left(\hat{h}^+[n-1]\right) \end{bmatrix}. \tag{4.33}$$

The process noise is used to model the unknown polar acceleration α and the turn velocity ω. Thus, $\tilde{\mathbf{Q}}[n] = \mathrm{diag}\left(\sigma_a^2, \sigma_\omega^2\right)$ with the covariance matrix $\mathbf{Q}[n]$ specified as

$$\mathbf{Q}[n] = \mathbf{G}\left(\hat{\mathbf{s}}^+[n-1]\right)\tilde{\mathbf{Q}}[n]\mathbf{G}\left(\hat{\mathbf{s}}^+[n-1]\right)^{\mathrm{T}}. \tag{4.34}$$

Here the matrix $\mathbf{G}\left(\hat{\mathbf{s}}^+[n-1]\right) \in \mathbb{R}^{4\times 2}$ is based on how the state variables are affected by α and ω. Thus,

$$\mathbf{G}[n] = \begin{bmatrix} \frac{\Delta t^2}{2}\cos\left(\hat{h}^+[n-1]\right) & 0 \\ \frac{\Delta t^2}{2}\sin\left(\hat{h}^+[n-1]\right) & 0 \\ \Delta t \cdot \mathbf{I}_2 \end{bmatrix}. \tag{4.35}$$

The measurement model relating the state variables to measurements is defined as

$$\mathbf{y}[n] = \mathbf{h}(\mathbf{s}[n]) + \mathbf{r}[n], \tag{4.36}$$

with the non-linear measurement function being specified by $\mathbf{h}(.)$ whereas $\mathbf{r}[n]$ is the zero mean Gaussian measurement noise with a covariance of $\mathbf{R}[n]$. As AOD ($\hat{\varphi}_{\mathrm{T}}$), TOA ($\hat{\tau}$) and orientation ($\hat{\theta}$) measurements from N_{RRH} different RRHs are used, the measurement vector is specified as

$$\mathbf{y}[n] = \left[\hat{\boldsymbol{\varphi}}_{\mathrm{T}}[n]^{\mathrm{T}}, \hat{\boldsymbol{\tau}}[n]^{\mathrm{T}}, \hat{\boldsymbol{\theta}}_{\mathrm{T}}[n]^{\mathrm{T}}\right]^{\mathrm{T}} \tag{4.37}$$

$$= [\hat{\varphi}_{\mathrm{T},1}[n], \ldots, \hat{\varphi}_{\mathrm{T},N_{\mathrm{RRH}}}[n], \hat{\tau}_1[n], \ldots, \hat{\tau}_{N_{\mathrm{RRH}}}[n], \tag{4.38}$$

$$\hat{\theta}_1[n], \ldots, \hat{\theta}_{N_{\mathrm{RRH}}}[n]]^{\mathrm{T}}. \tag{4.39}$$

Thus, the non-linear measurement function $\mathbf{h}(.)$ is similarly defined as $\mathbf{h}(\mathbf{s}[n]) = \left[\mathbf{h}_{\varphi}(\mathbf{s}[n])^{\mathrm{T}}, \mathbf{h}_{\tau}(\mathbf{s}[n])^{\mathrm{T}}, \mathbf{h}_{\theta}(\mathbf{s}[n])^{\mathrm{T}}\right]^{\mathrm{T}}$ with

$$\begin{aligned}
\mathbf{h}_{\varphi}(\mathbf{s}[n]) &= \left[h_{\varphi,1}(\mathbf{s}[n]), \ldots, h_{\varphi,N_{\mathrm{RRH}}}(\mathbf{s}[n])\right]^{\mathrm{T}}, \\
\mathbf{h}_{\tau}(\mathbf{s}[n]) &= \left[h_{\tau,1}(\mathbf{s}[n]), \ldots, h_{\tau,N_{\mathrm{RRH}}}(\mathbf{s}[n])\right]^{\mathrm{T}}, \\
\mathbf{h}_{\theta}(\mathbf{s}[n]) &= \left[h_{\theta,1}(\mathbf{s}[n]), \ldots, h_{\theta,N_{\mathrm{RRH}}}(\mathbf{s}[n])\right]^{\mathrm{T}}.
\end{aligned} \tag{4.40}$$

The measurement functions for the AOD, TOA, and the orientation for the ith RRH are specified as

$$\begin{aligned}
h_{\varphi,i}(\mathbf{s}[n]) &= \arctan\left(\frac{y[n]-y_i}{x[n]-x_i}\right), \\
h_{\tau,i}(\mathbf{s}[n]) &= \frac{||\mathbf{p}_i - \mathbf{p}[n]||}{c}, \\
h_{\theta,i}(\mathbf{s}[n]) &= h(n),
\end{aligned} \tag{4.41}$$

where $\mathbf{p}_i$ refers to he position of the ith RRH, x_i and y_i are its individual (x, y) coordinates and c is the speed of light. Based on this measurement model the measurements obtained from each RRH are used calculate the posterior mean ($\hat{\mathbf{s}}^{+}[n]$) and covariance ($\hat{\mathbf{P}}^{+}[n]$) of the state variables using the following equations:

$$\mathbf{K}[n] = \hat{\mathbf{P}}^{-}[n]\mathbf{H}[n]^{\mathrm{T}}\left(\mathbf{H}[n]\hat{\mathbf{P}}^{-}[n]\mathbf{H}[n]^{\mathrm{T}} + \mathbf{R}[n]\right)^{-1}, \tag{4.42}$$

$$\hat{\mathbf{s}}^{+}[n] = \hat{\mathbf{s}}^{-}[n] + \mathbf{K}[n]\left(\mathbf{y}[n] - \mathbf{h}\left(\hat{\mathbf{s}}^{-}[n]\right)\right), \tag{4.43}$$

$$\hat{\mathbf{P}}^{+}[n] = (\mathbf{I} - \mathbf{K}[n]\mathbf{H}[n])\hat{\mathbf{P}}^{-}[n]. \tag{4.44}$$

Here $\mathbf{H}[n]$ is the Jacobian matrix for the measurement function $\mathbf{h}(.)$ consisting of the concatenation of the Jacobian matrices of each of the functions in (4.41). Thus,

$$\mathbf{H}[n] = \left[\mathbf{H}_{\varphi}[n], \mathbf{H}_{\tau}[n], \mathbf{H}_{\theta}[n]\right]^{\mathrm{T}} \in \mathbb{R}^{(3N_{\mathrm{RRH}})\times 4}, \tag{4.45}$$

where

$$\mathbf{H}_{\varphi}[n] = \begin{bmatrix} -\frac{\hat{y}^{-}[n]-y_1}{\|\hat{\mathbf{p}}^{-}[n]-\mathbf{p}_1\|^2} & \frac{\hat{x}^{-}[n]-x_1}{\|\hat{\mathbf{p}}^{-}[n]-\mathbf{p}_1\|^2} & \mathbf{0} \\ \vdots & \vdots & \vdots \\ -\frac{\hat{y}^{-}[n]-y_{N_{\text{RRH}}}}{\left\|\hat{\mathbf{p}}^{-}[n]-\mathbf{p}_{N_{\text{RRH}}}\right\|^2} & \frac{\hat{x}^{-}[n]-x_{\text{RRH}}}{\left\|\hat{\mathbf{p}}^{-}[n]-\mathbf{p}_{N_{\text{RRH}}}\right\|^2} & \mathbf{0} \end{bmatrix}, \tag{4.46}$$

$$\mathbf{H}_{\tau}[n] = \begin{bmatrix} \frac{\hat{x}^{-}[n]-x_1}{\|\hat{\mathbf{p}}^{-}[n]-\mathbf{p}_1\|} & \frac{\hat{y}^{-}[n]-y_1}{\|\hat{\mathbf{p}}^{-}[n]-\mathbf{p}_1\|} & \mathbf{0} \\ \vdots & \vdots & \vdots \\ \frac{\hat{x}^{-}[n]-x_{N_{\text{RRH}}}}{\left\|\hat{\mathbf{p}}^{-}[n]-\mathbf{p}_{N_{\text{RRH}}}\right\|} & \frac{\hat{y}^{-}[n]-y_{\text{RRH}}}{\left\|\hat{\mathbf{p}}^{-}[n]-\mathbf{p}_{N_{\text{RRH}}}\right\|} & \mathbf{0} \end{bmatrix}, \tag{4.47}$$

$$\mathbf{H}_{\theta}[n] = \begin{bmatrix} \mathbf{0} & 1 \\ \vdots & \vdots \\ \mathbf{0} & 1 \end{bmatrix}. \tag{4.48}$$

The measurement noise covariance matrix is defined as

$$\mathbf{R}[n] = \text{diag}(\hat{\sigma}[n]^2_{\varphi,1}, \ldots, \hat{\sigma}[n]^2_{\varphi,N_{\text{RRH}}}, \hat{\sigma}[n]^2_{\tau,1}, \ldots, \hat{\sigma}[n]^2_{\tau,N_{\text{RRH}}}, \hat{\sigma}[n]^2_{\theta,1}, \ldots, \hat{\sigma}[n]^2_{\theta,N_{\text{RRH}}}). \tag{4.49}$$

The measurement variances for each RRH are estimated by estimating the SNR of the received signal in the current time step and comparing it with the measurement variance obtained by the algorithm for different SNR values.

4.4 CONCLUDING REMARKS

This chapter discusses the EKF algorithm for use in the tracking of HSTs. The theory behind the EKF is initially discussed followed by a discussion on how the EKF algorithm is implemented in the HST tracking scenario. The next chapter discusses the complete HST localization and tracking system structure.

CHAPTER 5 SYSTEM ARCHITECTURE

5.1 INTRODUCTION

In Chapter 3, the compressed sensing based 5G localization algorithm was discussed. In Chapter 4, the EKF algorithm used to track the HST was discussed. The information from the tracking algorithm is used by localization algorithm. Furthermore, information from the tracking algorithm is also used for beamforming and outlier detection. This chapter serves to describe the full localization and tracking solution, showing how exactly this exchange of information occurs.

The rest of the chapter is organized as follows. In Section 5.2, the complete algorithm is discussed. This is followed by Section 5.3 where the process of obtaining the measurement limits for use in LOS tracking, beamforming and outlier detection is discussed. At the end in Section 5.4, concluding remarks are made.

5.2 OVERALL ALGORITHM

The flow diagram in Fig. 5.1 illustrates the complete proposed localization algorithm. Initially the two RRHs, nearest to the HST, transmit M beamformed symbols at uniformly spaced angles between $-\pi/2$ and $\pi/2$ and the full DCS-SOMP based localization algorithm, from [7, 8], proposed for use in localization of stationery MTs is used to obtain the location and orientation of the train. The algorithm finds the AOA, AOD and TOA for each of the paths between the train and the RRH. All of these paths are assumed to be LOS paths and the location and the orientation of the train are calculated based on this assumption. The way the true LOS is identified is by comparing the location and orientation estimates for each path from both the RRHs. The paths for which the location and the orientation estimates are the closest to each other for both the RRHs are taken as the LOS paths for each RRH. Additionally, as the algorithm can achieve sub-meter accuracy for location estimation and sub-degree

accuracy for orientation estimation for low SNR values, the initial estimate is only accepted if the difference between the location estimate and the orientation estimate for each RRH is less than 2 m and 2°. The initial estimation process is repeated till this condition is met.

Once an initial estimate for the train's location is obtained, it is used by the EKF to predict the state of the train in the next time step. The prediction is used for beamforming and to obtain the beamspace limits for the LOS tracking. The AOA, TOA, and orientation are estimated at each RRH using the algorithm from Chapter 3 are thereafter passed through the outlier detection, ensuring that the extracted component is indeed the LOS component. The remaining measurements are then used for the update step of the EKF. This process is thereafter repeated from the prediction step of the EKF for the next time step.

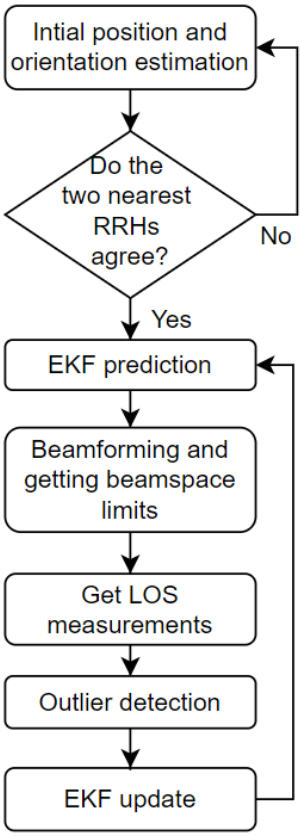

Figure 5.1. Flow diagram illustrating the complete proposed localization and tracking algorithm.

5.3 OBTAINING MEASUREMENT LIMITS

As mentioned in Chapter 3, the mean and the covariance from the prediction step of the EKF are used to limit the beamspace and TOA search in the DCS-SOMP algorithm for LOS tracking. The same limits are used for beamforming and outlier detection. These limits are based on the covariance $\hat{\mathbf{P}}^{-}[n]$ and they are centered around the mean $\hat{\mathbf{s}}^{-}[n]$. Thus, the mean is first converted to the measurement domain as

$$\mathbf{y}^{-}[n] = \mathbf{h}(\hat{\mathbf{s}}^{-}[n]), \tag{5.1}$$

while the Jacobian matrix of $\mathbf{h}(.)$ is used to obtain the covariance in the measurement domain. Thus,

$$\mathbf{Y}^{-}[n] = \mathbf{H}[n]\hat{\mathbf{P}}^{-}[n]\mathbf{H}[n]^{\mathrm{T}} + \mathbf{R}[n-1]. \tag{5.2}$$

The covariance of the measurement noise from the previous time step is added to account for additional measurement noise. The diagonal elements of the matrix $\mathbf{Y}^{-}[n]$ are then taken as the variances for the prediction in the measurement domain. Based on this, limits of $\pm 3.3\sigma$ around the mean in the measurement domain are used, so as to capture 99.9% of the samples in the distribution.

5.4 CONCLUDING REMARKS

This chapter discusses how the compressed sensing based localization algorithm interacts with the EKF based tracking algorithm for localization and tracking of HSTs. The next chapter discusses the experimental setup used to determine whether the proposed algorithm can achieve satisfactory performance.

CHAPTER 6 EXPERIMENTAL SETUP

6.1 INTRODUCTION

This chapter discusses the experimental setup used in order to determine whether the proposed algorithm can achieve satisfactory performance. The assumed system model in the simulation scenario is specified in Section 6.2. The next section describes the channel model used in simulation. The entire simulation model implemented in Python is described in Section 6.4. Section 6.5 describes the aim and the parameter settings for the various experiments that will be performed in order to test the algorithm. Lastly, in Section 6.6, some concluding remarks are made.

6.2 SYSTEM MODEL

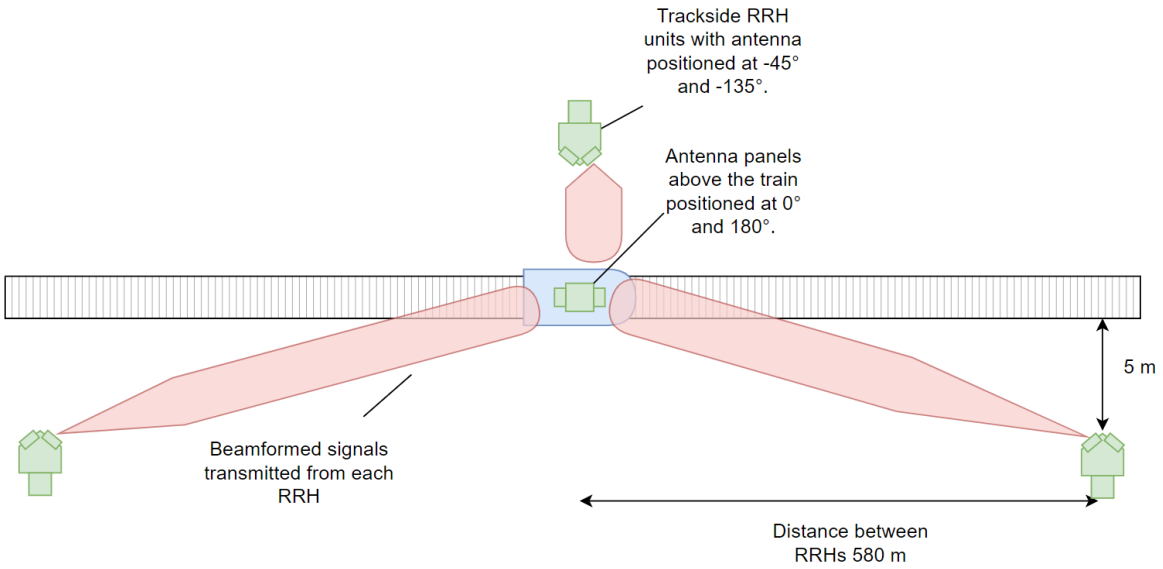

Figure 6.1. The system model for the HST scenario as specified by the 3GPP for carrier frequencies around 30 GHz in [9].

The system model used is based on the HST scenario specified by the 3rd Generation Partnership Project (3GPP) in [9]. Fig. 6.1 illustrates this scenario. The train has two antenna panels at 0° and 180°. RRH units are placed on alternating sides of the track with a distance of 580 m between the tracks. Each RRH is placed 5 m away from the tracks and has two antenna panels positioned at -45° and -135°.

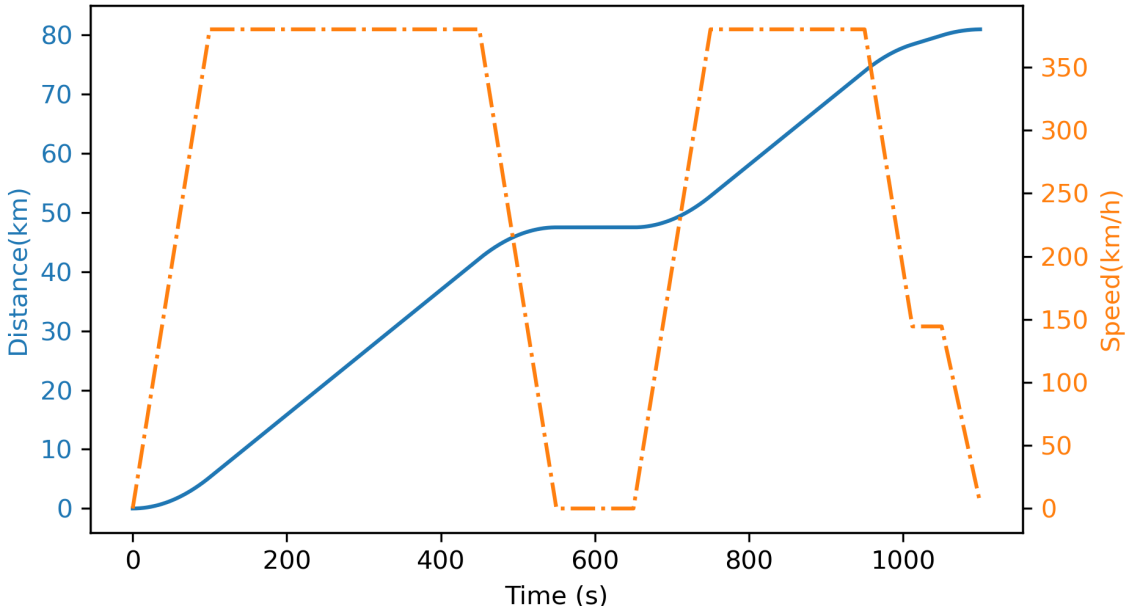

Figure 6.2. Plot showing the velocity of the train and the distance travelled by the train throughout the simulated trajectory.

In previous studies [2–5], two scenarios are typically used. In [2–4], a straight track scenario is used, as generally due to high-speeds the train tracks have limited curvature. In [5] on the other hand, a real-life track scenario is considered using data from OpenStreetMap (OSM) [59]. Both these scenarios are considered here. The plot in Fig. 6.2 shows the distance travelled by the train and the velocity of the train throughout the simulated trajectory for the straight track scenario. A 1100 s long trajectory is simulated. The velocity increases linearly from 0 m/s to 370 m/s for the first 100 s, for the next 350 s it stays constant. This is followed by the velocity linearly decreasing from 370 m/s to 0 m/s in the next 100 s and stays at 0 m/s in the following 100 s. Thereafter, it again increases linearly from 0 m/s to 370 m/s over the next 100 s, staying constant at 370 m/s for the next 200 s. Over the next 75 s it linearly decreases from 370 m/s to 150 m/s. It thereafter stay constant at 150 m/s for the next 25 s, followed by another period of deceleration from 150 m/s to 0 m/s. This velocity profile is based of the description provided in [5] and it also used in the simulation with real-life HST track.

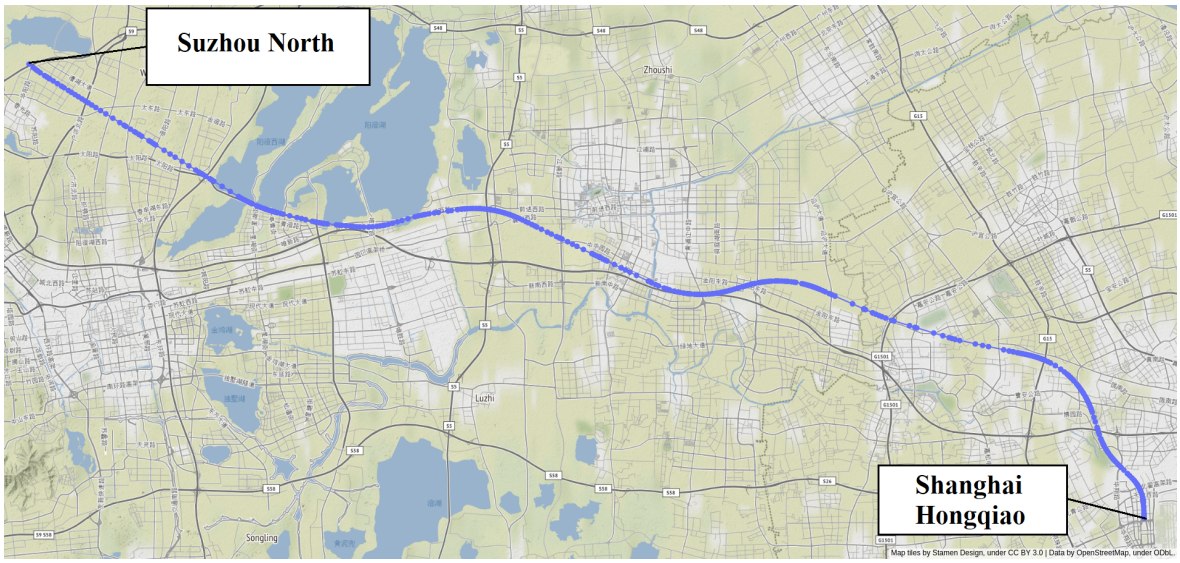

Figure 6.3. Map showing the real-life HST track from Shanghai Hongqiao station to the Suzhou North station used in simulation. Plotted using data obtained from OSM [59].

The real-life HST train track used by [5] from OSM data [59] can be seen in Fig. 6.3. The track is part of the high-speed rail line between Shanghai and Beijing in China. It starts at Shanghai Hongqiao station and ends at the Suzhou North station. The 100 s period for which the the train has a velocity of 0 m/s is a stop at the Kushan South station between the two stations.

The track data is obtained from OSM [59]. OSM provides the latitude and longitude coordinates of points on the track. These points can be converted to (x,y) coordinates and joined using straight lines to obtain the track. The resulting track is not an accurate representation of a real-life train track, as at the intersection of these lines joining the points on the track the heading direction of the train changes abruptly.

This problem of abrupt jumps in heading direction is solved using cubic Bezier curves to join map points instead of straight lines [60]. The process for generating control points for the cubic Bezier curves can be found in Addendum A. Fig. 6.4 shows part of the generated track when cubic Bezier curves are used. The cubic Bezier curve generated track is much smoother compared to the track joined using straight lines, especially at the intersections.

The carrier frequency f_c is set to 38 GHz with a bandwidth of 245.76 MHz and a FFT size of 2048 is used. Furthermore, the transmit power is set to 30 dBm while the noise power at the receiver is set to -174 dBm/Hz with each antenna having a noise figure of 5 dB.

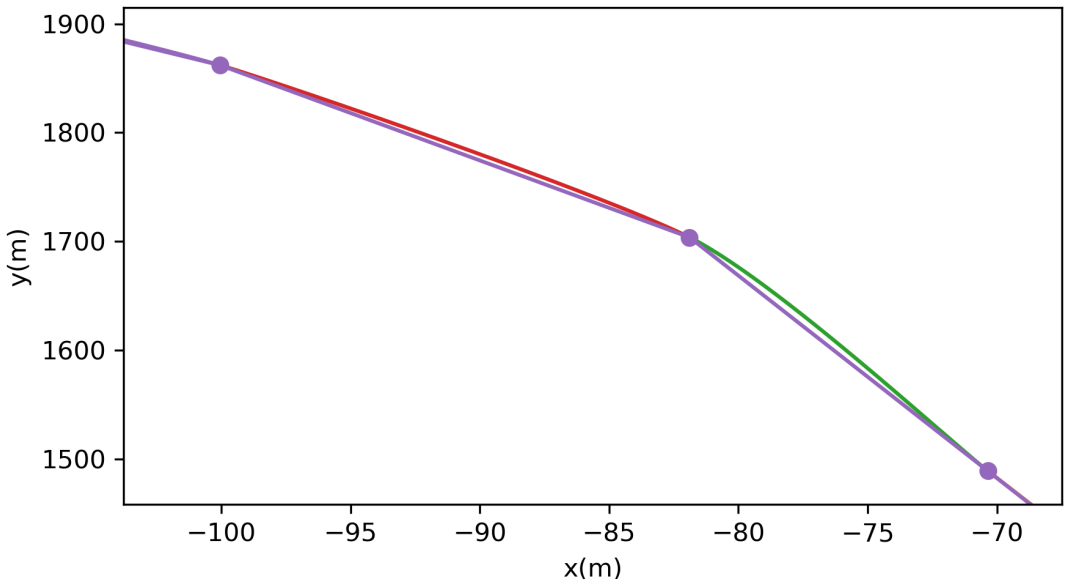

Figure 6.4. Plot showing map points joined using straight lines and using cubic Bezier Curves.

6.3 CHANNEL MODEL

6.3.1 General channel model

The channel model described in Chapter 2 is used. The model is defined as follows:

$$\mathbf{H}[n] = \mathbf{A}_{\mathrm{Rx}}[n]\Gamma[n]\mathbf{A}_{\mathrm{Tx}}^{\mathrm{H}}[n], \tag{6.1}$$

where the response vectors are

$$\begin{aligned} \mathbf{A}_{\mathrm{Tx}}[n] &= \left[\mathbf{a}_{\mathrm{Tx},n}\left(\varphi_{\mathrm{T},0}\right), \ldots, \mathbf{a}_{\mathrm{Tx},n}\left(\varphi_{\mathrm{T},K}\right)\right], \\ \mathbf{A}_{\mathrm{Rx}}[n] &= \left[\mathbf{a}_{\mathrm{Rx},n}\left(\varphi_{\mathrm{R},0}\right), \ldots, \mathbf{a}_{\mathrm{Rx},n}\left(\varphi_{\mathrm{R},K}\right)\right], \end{aligned} \tag{6.2}$$

while $\Gamma[n]$ is given by

$$\Gamma[n] = \sqrt{N_t N_r} \times \mathrm{diag}\left\{\frac{1}{\sqrt{\rho_0}} e^{\frac{-j2\pi n\tau_0}{NT_s}}, \ldots, \frac{1}{\sqrt{\rho_K}} e^{\frac{-j2\pi n\tau_K}{NT_s}}\right\}. \tag{6.3}$$

The subscript k specifies the index of the path whereby $k = 0$ is the LOS path and the rest are NLOS paths with K total paths; ρ_k is the path loss; τ_k is the time delay; N_r is the number of antennas at the receiver, N_t is the number of antennas at the transmitter and T_s is the sampling time. Furthermore, $\varphi_{\mathrm{T},k}$ refers to the the broadside AOD and $\varphi_{\mathrm{R},k}$ refers to the broadside AOA for the kth path. The definition

of the steering vectors $\mathbf{a}_{\mathrm{Tx},n}(\varphi_{\mathrm{T},k})$ and $\mathbf{a}_{\mathrm{Rx},n}(\varphi_{\mathrm{T},k})$ assuming a Uniform Linear Array (ULA) can be found in Chapter 2. To simulate the HST scenario ρ_k, τ_k, $\varphi_{\mathrm{T},k}$ and $\varphi_{\mathrm{R},k}$ need to be generated for each path.

6.3.2 HST channel model

The HST scenario channel model has not been studied extensively in literature [54, 61, 62]. The model proposed in [54] is made specifically for a straight track scenario and thus cannot be used on the real-life track scenario. The model proposed in [61, 62] is more general making it the better choice for use here. These studies provide a description of the small-scale fading. The parameters for the large scale fading are obtained from the urban micro (uMI) model specified by the 3GPP for carrier frequencies above 6 GHz in [63].

6.3.2.1 Large-Scale Fading

The path loss for the LOS path and the NLOS path in dB are specified as

$$PL_{LOS} = 32.4 + 21\log_{10}(d) + 20\log_{10}(f_c), \tag{6.4}$$

$$PL_{NLOS} = 32.4 + 31.9\log_{10}(d) + 20\log_{10}(f_c). \tag{6.5}$$

Here d is the distance for the path and f_c is the carrier frequency. The standard deviation for the shadowing, σ_{SF}, for the LOS path and the NLOS paths is 4 dB and 8.2 dB respectively. The mean, μ_k, and the standard deviation, σ_k, of the Ricean K-factor are specified as 9 dB and 5 dB respectively [63].

6.3.2.2 Small scale fading

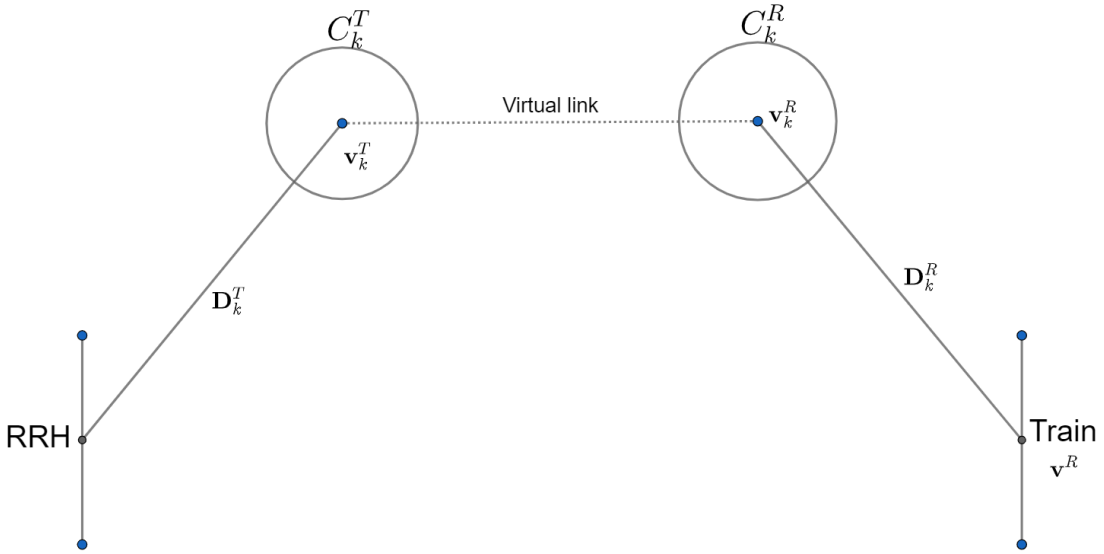

Figure 6.5. Diagram illustrating how the NLOS paths are modelled as clusters.

The NLOS paths are modeled using clusters, with their evolution in time due to the motion of the train, being modelled using a birth-death process [61, 62]. This modelling is based of the WINNER II channel model. Fig. 6.5 illustrates the cluster modeling scenario. The cluster C_k^T is $\mathbf{D}_k^T$ away from the transmitter/RRH and moves with a velocity of $\mathbf{v}_k^T$. Furthermore, it shares a virtual link with C_k^R, which is $\mathbf{D}_k^R$ away from the receiver/train and moves with a velocity of $\mathbf{v}_k^R$. The velocity of the train is defined as $\mathbf{v}^R$.

The flow diagram for the NLOS cluster modelling can be seen in Fig. 6.6. Here firstly $N_{cluster}$ clusters are generated. The value of $N_{cluster}$ is picked from a Poisson distribution with the mean λ_G/λ_R. λ_G is the birth rate, which is set to 20/m, and λ_R is the death rate, which is set to 4/m, for the birth-death process. Thus, on average there are 5 NLOS paths. It has to be noted that [61, 62] suggests λ_G and λ_R as 80/m and 4/m respectively, thus on average there are 20 paths. However, the mmWave channel is extremely sparse with up to 3-4 NLOS paths available [64]. In order to reflect this, the birth and the death rate are set accordingly.

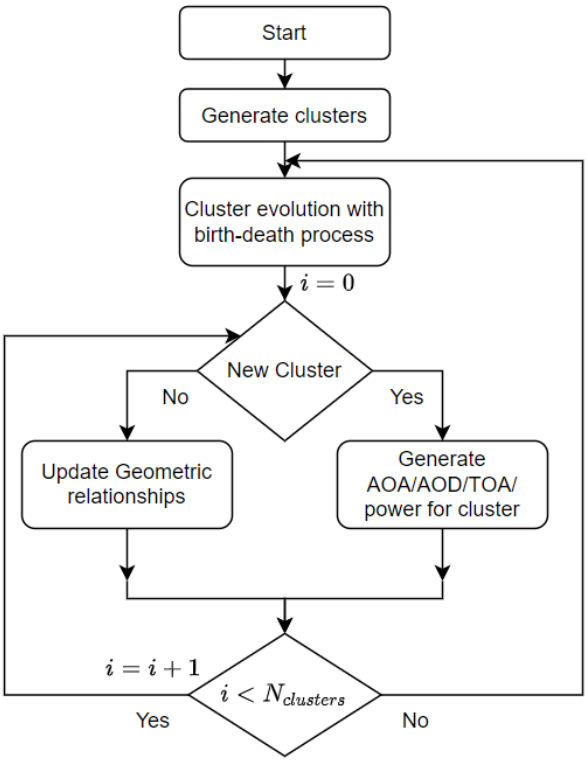

Figure 6.6. Flow diagram illustrating how the clusters are modeled for NLOS paths.

In the next time step, these clusters are evolved based on the birth-death process. Here the clusters are assigned a survival probability that determines if the clusters survive, which is specified as

$$P_{\mathrm{T}}(\Delta t) = e^{-\lambda_R \frac{P_F\left(\Delta v^R + \Delta v^T\right)\Delta t}{D_c^s}}, \tag{6.6}$$

with $P_F = 0.3$ being the percentage of moving clusters, $D_c^s = 100$ is a constant, Δv^R and Δv^T are the mean relative velocities. They are specified as $\Delta v^R = \mathrm{E}\left[\left\|\mathbf{v}^R - \mathbf{v}_k^R\right\|\right]$ and $\Delta v^T = \mathrm{E}\left[\left\|\mathbf{v}_k^T\right\|\right]$. Furthermore, a random number of new clusters are also generated. The number of new clusters generated follows a Poisson distribution with mean

$$\mathrm{E}\left[N_{\mathrm{new}}(t+\Delta t)\right] = \frac{\lambda_G}{\lambda_R}\left(1 - P_{\mathrm{T}}(\Delta t)\right). \tag{6.7}$$

Thereafter, for each of the clusters either new parameters are generated or the previous parameters are evolved based on geometric relationships. For each cluster, pair the path loss for the virtual link, the delay for the virtual link (τ_k), the velocity of the clusters ($\mathbf{v}_k^T - \mathbf{v}_k^R$), the initial distance of the pair ($D_k^T - D_k^R$), the AOD ($\varphi_{\mathrm{T},k}$) and AOA ($\varphi_{\mathrm{R},k}$) need to be generated. The delay is generated from an exponential distribution with a mean of $2.3 \times \sigma_\tau$, where σ_τ is a randomly generated delay spread with $\mathrm{E}\left[\log_{10}\sigma_\tau\right] = -6.63$ and $\mathrm{std}\left[\log_{10}\sigma_\tau\right] = -7.6$. The velocities are set to 30 m/s in a random direction between 0 and 2π. The initial distances, D_k^T and D_k^R, of the clusters are generated from an exponential distribution with a mean of 25 m and 30 m respectively. The AOD and AOA are generated from a wrapped Gaussian distribution with means 0.78 rad and 1.04 rad and standard deviations 0.91 rad and 0.53 rad respectively. The power of the cluster is generated as

$$\tilde{P}_k = \exp\left(-\tau_k \frac{1.3}{2.3 \times \sigma_\tau}\right) 10^{-\frac{Z_k}{10}}, \tag{6.8}$$

with $Z_k \sim \mathcal{N}(0,3)$ [62].

For the evolution of the existing clusters, the distance vectors, the power and the delay of the virtual link need to be updated. The distance vectors are updated as

$$\begin{aligned} \mathbf{D}_k^R(t+\Delta t) &= \mathbf{D}_k^R(t) + \mathbf{v}_k^R \Delta t + \mathbf{v}^R \Delta t, \\ \mathbf{D}_k^T(t+\Delta t) &= \mathbf{D}_k^T(t) + \mathbf{v}_k^T \Delta t. \end{aligned} \tag{6.9}$$

The virtual link delay is updated as

$$\tau_k(t+\Delta t) = \left[\|\mathbf{D}_k^R(t+\Delta t)\| + \|\mathbf{D}_k^T(t+\Delta t)\|\right]/c + \tilde{\tau}_k(t+\Delta t), \tag{6.10}$$

where $\tilde{\tau}_k(t+\Delta t) = e^{-\frac{\Delta t}{\varsigma}}\tau_k(t) + \left(1 - e^{-\frac{\Delta t}{\varsigma}}\right)X$ with $\varsigma = 7$ and X is a random number generated from same distribution as τ_k. Lastly, the power is updated as [62]

$$\tilde{P}_k(t+\Delta t) = \tilde{P}_k(t)\frac{3\tau_k(t) - 2\tau_k(t+\Delta t)}{\tau_k(t)}. \tag{6.11}$$

6.4 FULL SIMULATION SETUP

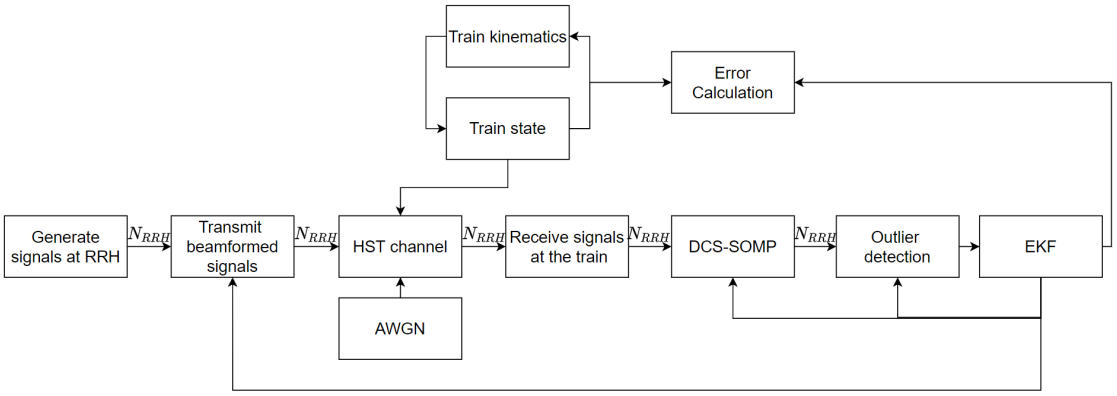

Figure 6.7. Diagram illustrating how the simulation model is set in Python.

Fig. 6.7 illustrates the implementation of the entire simulation setup in Python. At first the signals to be transmitted at each RRH are generated. These are beamformed in the direction of the train using the prediction from the EKF from the previous time step. The beamformed signals from each RRH are passed through the HST channel with Additive white Gaussian noise (AWGN) added at each time step. The HST channel is updated at every time step based on the motion of the train as described in the previous sub-section. Furthermore, the train state is evolved based on the map and acceleration profile discussed in the previous sub-section. The train thereafter receives the signals from each RRH. These signals are then processed with the DCS-SOMP algorithm, as described in Chapter 3, to obtain estimates for the AOD and TOA of the LOS path and the orientation of the train. Outlier detection is performed on these measurements as described in Chapter 5. The estimates that were not classified as outliers are combined with the EKF as described in Chapter 4 to obtain an estimate for the train's state. The resulting estimate is subtracted from the true state of the train to compute the estimation error. This process is repeated for every time step.

6.5 EXPERIMENT DESCRIPTION

The algorithm is tested in the simulation setup described in the previous sections. Several different experiments are performed to test how the algorithm performs for various parameter values. The parameters used in each of these tests are described in the sub-sections below.

6.5.1 Straight track Scenario

This simulation is run on a straight track scenario using LOS tracking and without using LOS tracking in order to compare the two algorithms. The RRHs used (N_{RRH}) for localization are varied from one to

six. Furthermore, the following settings are made: number of transmit antennas on the RRH, $N_t = 32$, the number of receive antennas on the train, $N_r = 8$, carriers $N = 64$ and symbols transmitted each time, $M = 32$. For the EKF the localization intervals, Δt, is set to 0.1 s, whereas σ_α and σ_ω are set to 3.5 and 0.0001 respectively (these are based on the expected change in velocity and direction throughout the trajectory).

6.5.2 Real-life HST track Scenario

The simulation parameters are identical to the straight track scenario, except that the real-life HST track is used instead of a straight track. Furthermore, for the EKF σ_ω is set to 0.03.

6.5.3 Varying the process noise

In this simulation, the values of σ_α and σ_ω are varied for the LOS tracking algorithm. The real-life HST track is used with 2 RRHs being used for localization. The rest of the parameters are the same as the real-life HST track simulation.

6.5.4 Varying the interval of localization

In this simulation, the values of Δt are varied for the LOS tracking algorithm on the real-life HST track, using 2 RRHs for localization. The rest of the parameters are the same as real-life HST track simulation.

6.5.5 Varying system parameters

The localization parameters (N_t, N_r, N and M) are varied for the LOS tracking algorithm on the real-life HST track, using 2 RRHs for localization. The parameter being tested is varied from 2 to 64 in powers of 2, whereas the parameters not being varied are all set to 32. The parameters used for the EKF are identical to the real-life HST track simulation.

6.5.6 Minimum parameter values

Based on the results obtained in the previous simulation, the lowest parameter settings that are expected to meet the requirements are simulated for the LOS tracking algorithm on the real-life HST track scenario.

6.6 CONCLUDING REMARKS

This chapter discusses the experimental setup used to check whether the proposed algorithm can achieve satisfactory performance. The next chapter discusses the results obtained from running the algorithm in the simulation scenario discussed in this chapter.

CHAPTER 7 RESULTS AND DISCUSSION

7.1 INTRODUCTION

As discussed in Chapter 1, the primary goal of the proposed localization algorithm is to achieve sub-meter localization accuracy, with estimation accuracy of less than 1 m/s for velocity estimation and 1° for heading estimation. The lower end of the performance requirements are an estimation accuracy of 3 m, 2 m/s and 2° with 95% availability as specified by the 3GPP in [65] for the use case of machine control and transportation. Furthermore, the lowest system parameter settings for which the performance requirements can be met needs to be determined.

Additionally the algorithm should preform better compared to existing 5G based HST localization and tracking algorithms [2–5]. The TDOA based algorithm can achieve an estimation accuracy of less than 1 m, 1 m/s and 1° for the train position, velocity and heading direction for 99.9% of the simulated trajectory for a straight track scenario using five RRHs [2]. On a real-life HST track on the other hand, the estimation error for the location, velocity and heading direction is 2.3 m, 0.47 m/s, and 1.6° for 95% of the simulated trajectory when five RRHs are used [5]. These are the benchmarks to beat.

In order to answer these questions, the experimental setup proposed in Chapter 6 was implemented on Python. The Cumulative Distribution Function (CDF) of estimation error obtain in simulation from the various scenarios discussed in Chapter 6 are presented in this chapter.

The rest of this chapter is organized as follows. In Section 7.2, the results from the straight track scenario are presented. Section 7.3 presents the results for the real-life HST track Scenario. Next in Section 7.4, the results obtained when the process noise for the EKF is varied are presented. This is followed by Section 7.5, where the effect of varying the localization interval is investigated. Section 7.6

- 7.9 presents the results for varying the system parameters (N_t, N_r, N and M). The lowest parameter settings that achieved satisfactory performance in the previous simulation scenarios are combine to determine the achievable performance in Section 7.10. Finally, in Section 7.11, concluding remarks are made.

7.2 STRAIGHT TRACK SCENARIO

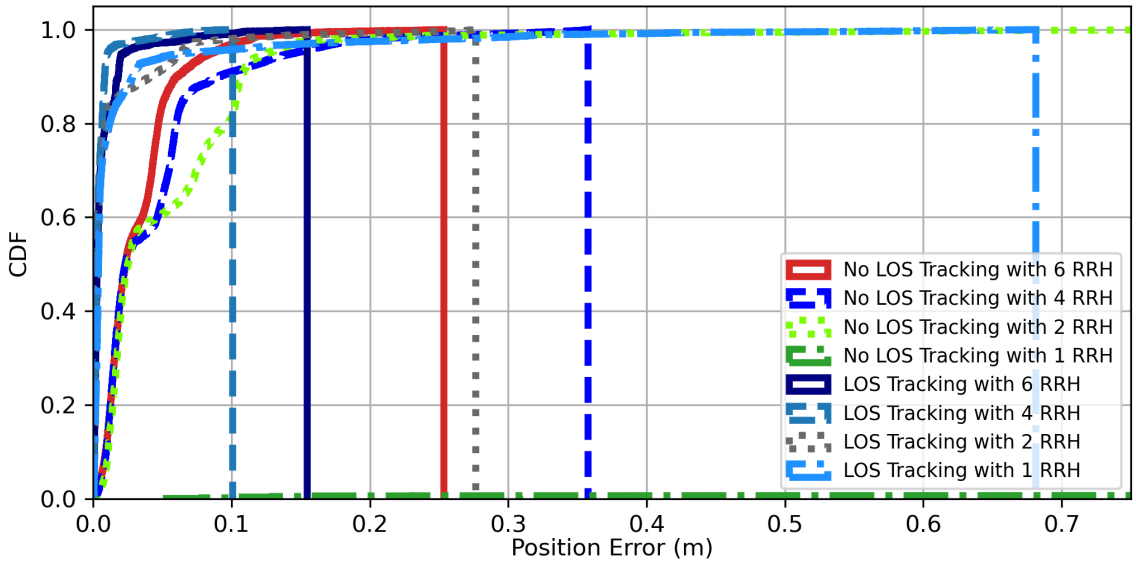

Figure 7.1. Plot showing the CDF for location estimation error when LOS tracking is used and when it is not used, on a straight track scenario for various values of RRHs used.

Table 7.1. Table showing the number of measurements flagged as outliers in simulation.

NRRH	LOS Tracking	No LOS Tracking
6	167	7611
4	85	7327
2	40	7089
1	18	8117

Fig. 7.1 and Fig. 7.2 show the CDF plots for the location estimation and velocity estimation error. In the CDF plots the x-axis indicates the estimation error while the y-axis indicates the portion of the trajectory for which the estimation error was a certain value. It is clear that when using LOS tracking, a

localization accuracy of less than 1 m and a velocity estimation accuracy of less than 1 m/s is achieved throughout the trajectory using just one RRH. The estimation accuracy only improves as the number of RRHs used increase. Furthermore, it is clear that the estimation accuracy improves when LOS tracking is used, compared to when LOS tracking is not used, as the performance observed using 2 RRHs with LOS tracking is similar to the performance observed when 6 RRHs are used without LOS tracking. Furthermore, with LOS tracking sub-meter localization accuracy is achieved with just one RRH whereas without LOS tracking the localization performance is poor due to the EKF diverging. This improvement in performance can be explained by looking at the number of measurements that each algorithm flags as outliers in Table 7.1. For LOS tracking, significantly fewer measurements are flagged as outliers compared to when LOS tracking is not used. Thus more measurements are available for localization, leading to more accurate localization. Lastly, the proposed algorithm clearly performs better than TDOA based localization algorithm as the performance with just one RRH is similar to the performance achieved with 5 RRHs in [2].

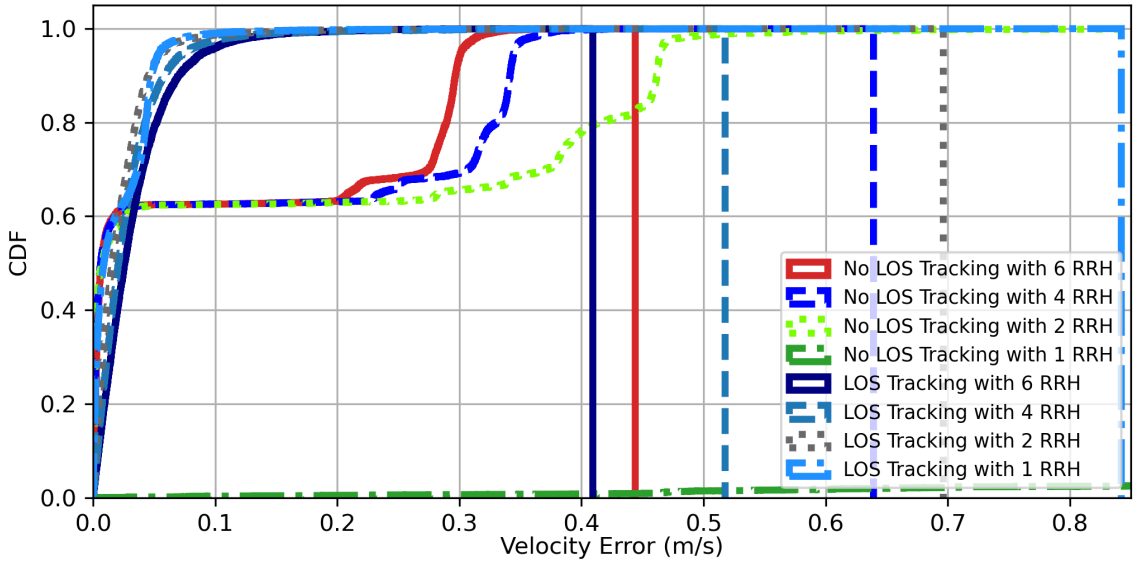

Figure 7.2. Plot showing the CDF for velocity estimation error when LOS tracking is used and when it is not used on a straight track scenario for a range of RRHs used for localization.

7.3 REAL-LIFE HST TRACK SCENARIO

Fig. 7.3 - 7.5 show the CDF plots for the location, velocity and heading estimation error. The proposed algorithm achieves location and velocity estimation accuracy of less than 1 m and 1 m/s respectively using 2 RRHs. Furthermore, sub-degree heading estimation accuracy is achieved for 99.9% of the

simulated trajectory. When one RRH is used the estimation error for location, velocity and heading is 1.46 m, 0.18 m/s and 1° for 99% of the trajectory. This meets the performance requirements set by 3GPP for the used case of machine control and transportation. As seen for the straight track scenario, the performance improves as the number of RRHs used increase and the LOS tracking shows an improvement in performance compared to when LOS tracking is not used. This can once again be attributed to the large number measurements that are flagged as outliers as seen in Table 7.2. Furthermore, the proposed algorithm clearly performs better than TDOA based localization algorithm as the performance with just one RRH is better than the performance achieved with 5 RRHs in [5]. Overall, the performance observed on the real-life track is worse compared to the straight track scenario. This is expected, as there are more unmodelled changes on a real-life track.

Table 7.2. Table showing the number of measurements flagged as outliers in simulation.

NRRH	LOS Tracking	No LOS Tracking
6	659	13074
4	309	11951
2	75	6959
1	64	453

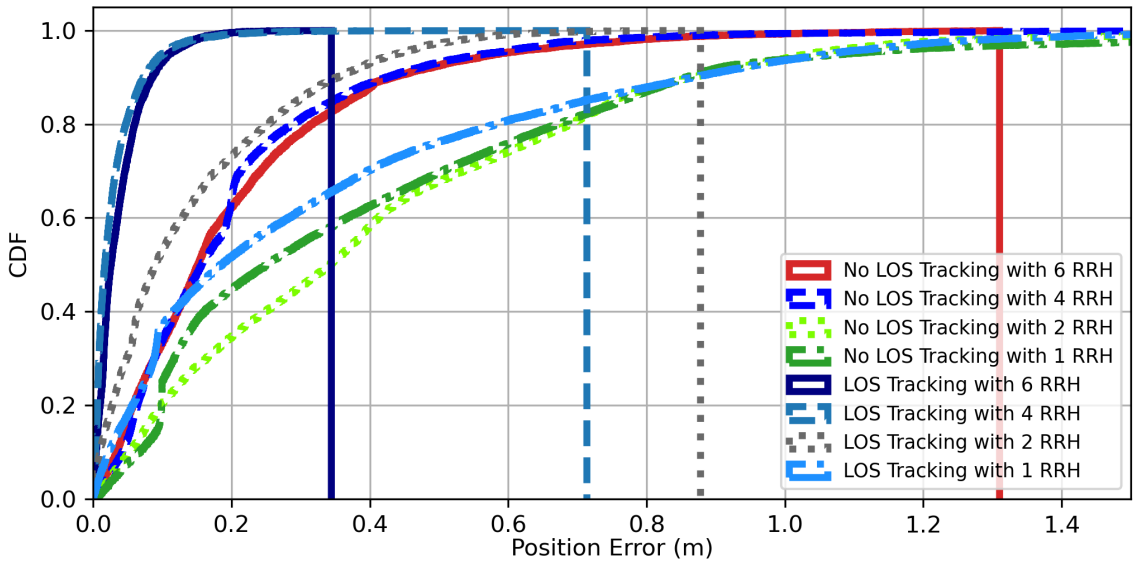

Figure 7.3. Plot showing the CDF for location estimation error when LOS tracking is used and when it is not used on a real-life HST track scenario for various values of RRHs used for localization.

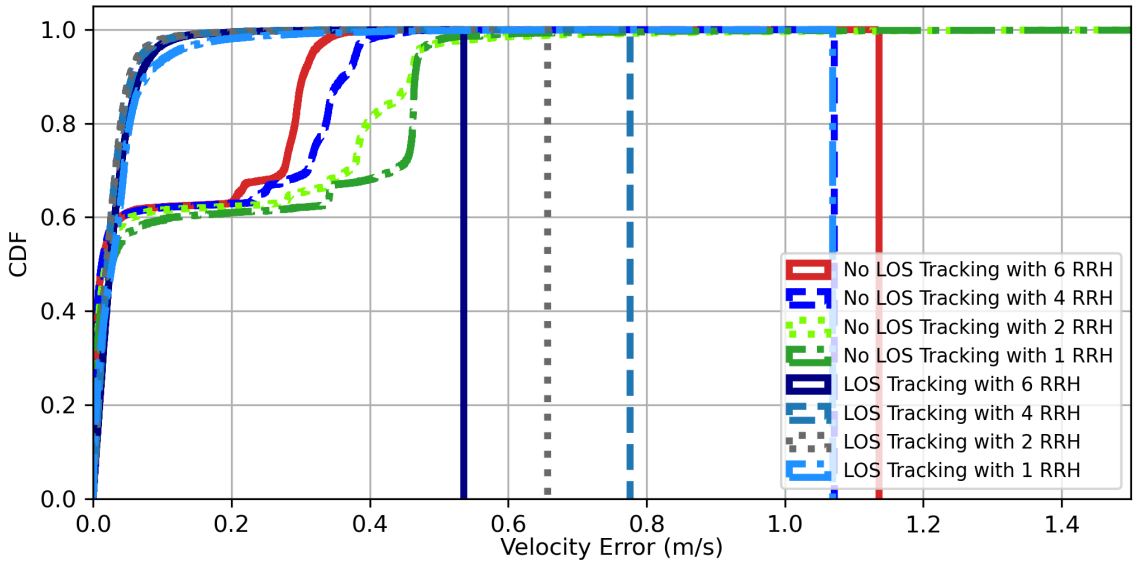

Figure 7.4. Plot showing the CDF for velocity estimation error when LOS tracking is used and when it is not used on a real-life HST track scenario for various values of RRHs used for localization.

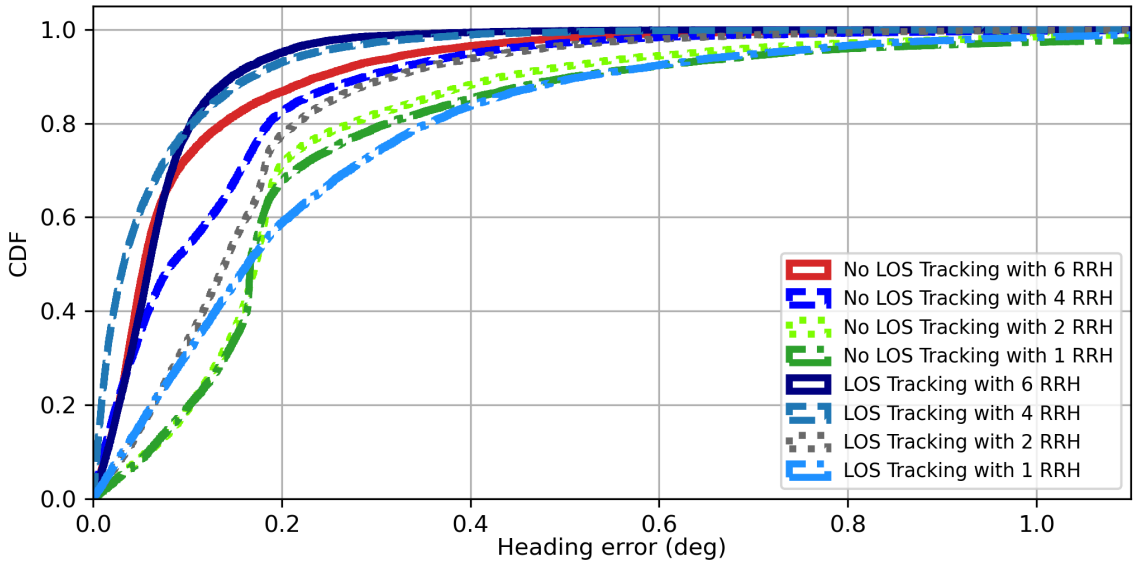

Figure 7.5. Plot showing the CDF for heading estimation error when LOS tracking is used and when it is not used on a real-life HST track scenario for various values of RRHs used for localization.

7.4 VARYING THE PROCESS NOISE

7.4.1 Varying σ_α

The CDF of the estimation error for the location, velocity and heading direction for various values of σ_α can be seen in Fig. 7.6 - 7.8. It is clear that varying σ_α does not effect the heading estimation at all. This is expected as σ_α represent the noise injected into the system to account for the unknown linear acceleration and linear acceleration does not influence the heading direction ((4.34) and (4.35)).

The position estimation is not significantly affected by varying σ_α. This is expected as in the process noise definition ((4.34) and (4.35)), σ_α is multiplied by Δt^2 twice for the (x, y) coordinates of the train. Thus, the additional noise injected into the EKF prediction of (x, y) coordinates of the train is not significant enough to be affected by it. The velocity estimation is affected by σ_α slightly more compared to position estimation as when injecting process noise σ_α is multiplied by Δt twice in (4.34) and (4.35). For larger values of σ_α, the velocity estimation degrades. Overall changing σ_α from 3.5 (the value determined by the maximum change in acceleration in simulation) to other values does significantly improve or degrade localization performance.

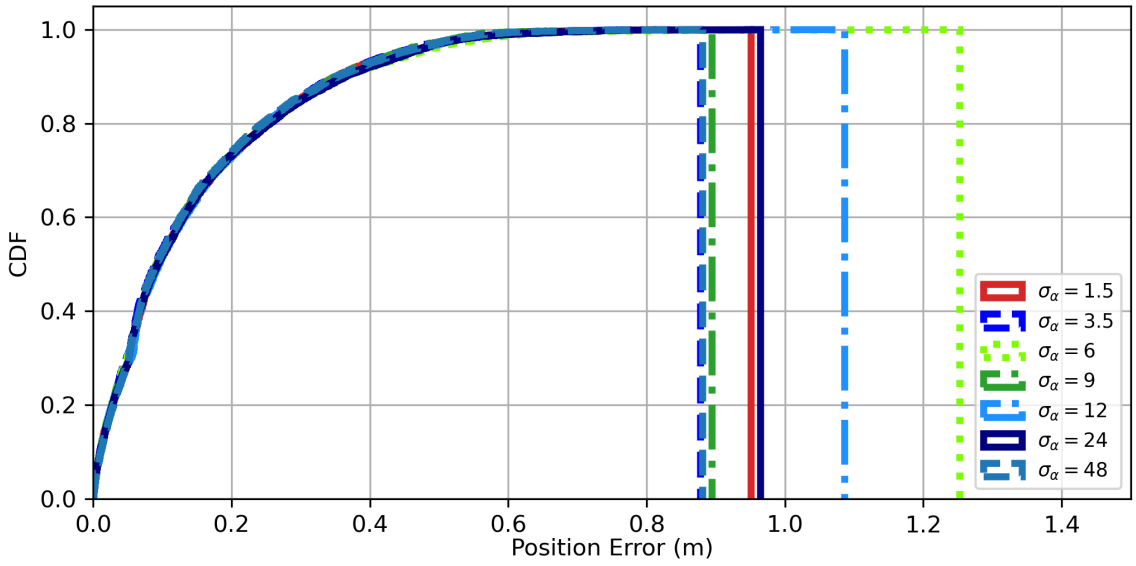

Figure 7.6. Plot showing the CDF for location estimation error when LOS tracking is used with 2 RRHs on a real-life HST track scenario for various values of σ_α.

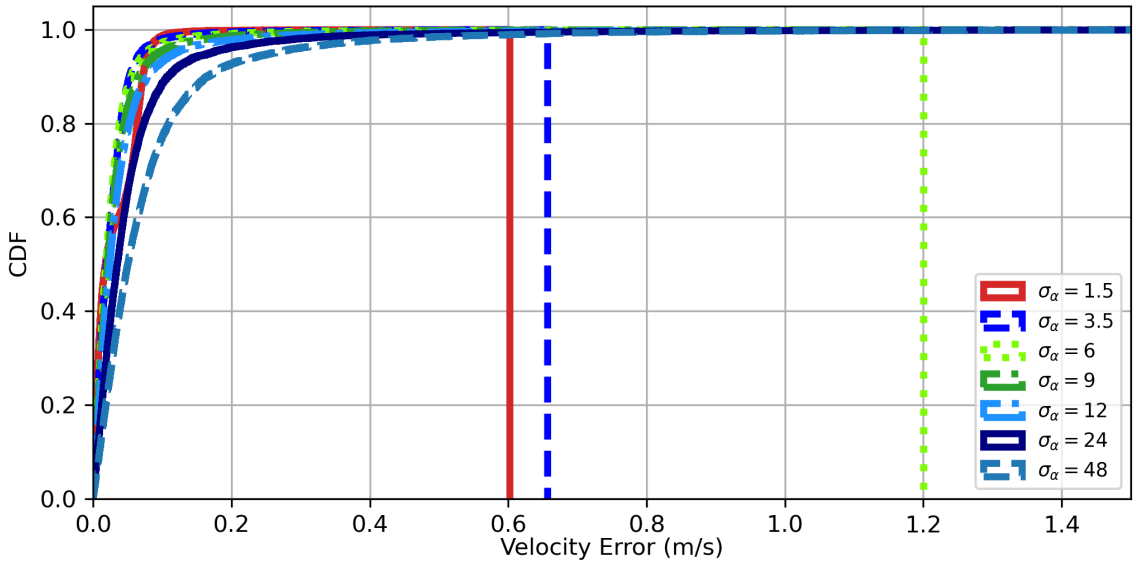

Figure 7.7. Plot showing the CDF for velocity estimation error when LOS tracking is used with 2 RRHs on a real-life HST track scenario for various values of σ_α.

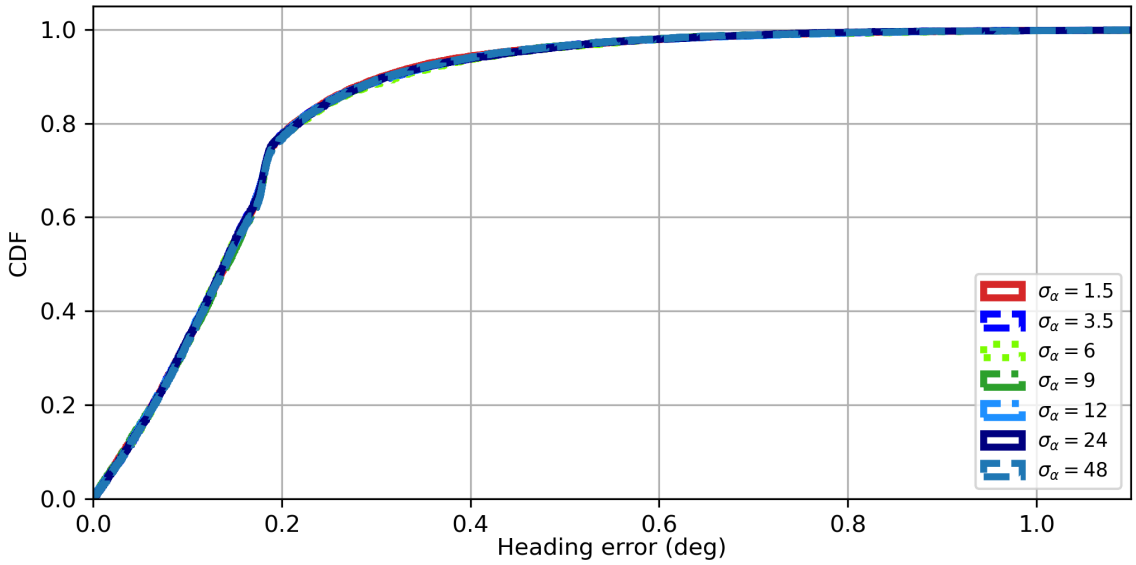

Figure 7.8. Plot showing the CDF for heading estimation error when LOS tracking is used with 2 RRHs on a real-life HST track scenario for various values of σ_α.

7.4.2 Varying σ_ω

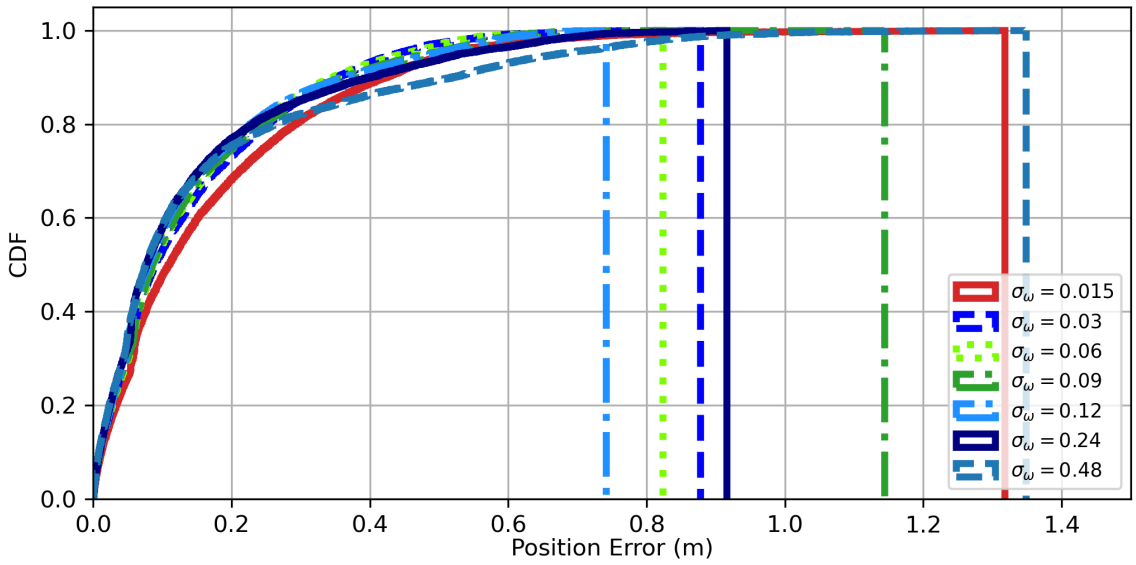

Figure 7.9. Plot showing the CDF for location estimation error when LOS tracking is used with 2 RRHs on a real-life HST track scenario for various values of σ_ω.

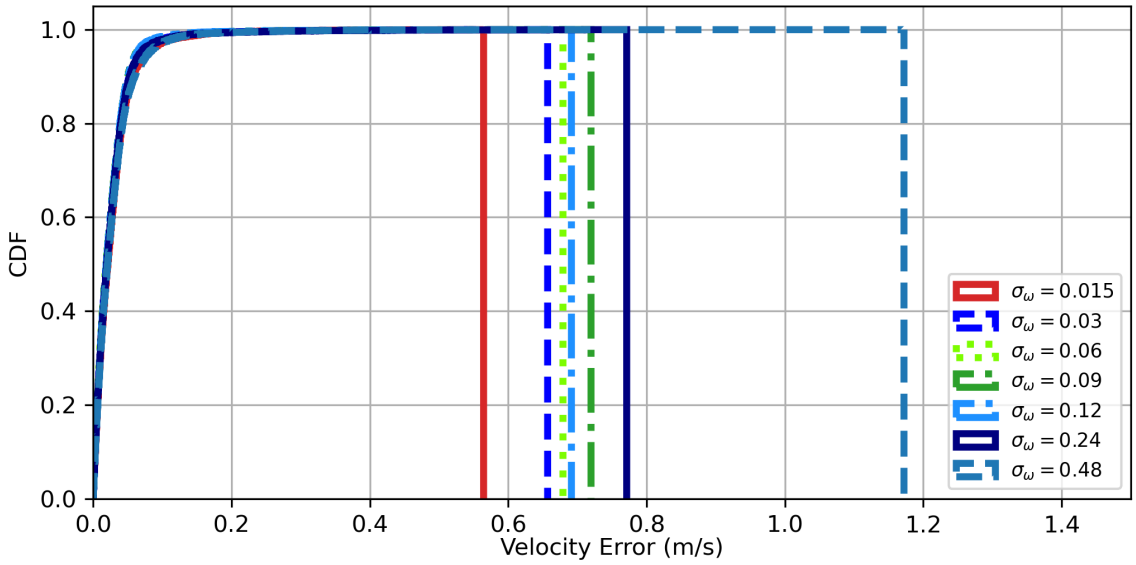

Figure 7.10. Plot showing the CDF for velocity estimation error when LOS tracking is used with 2 RRHs on a real-life HST track scenario for various values of σ_ω.

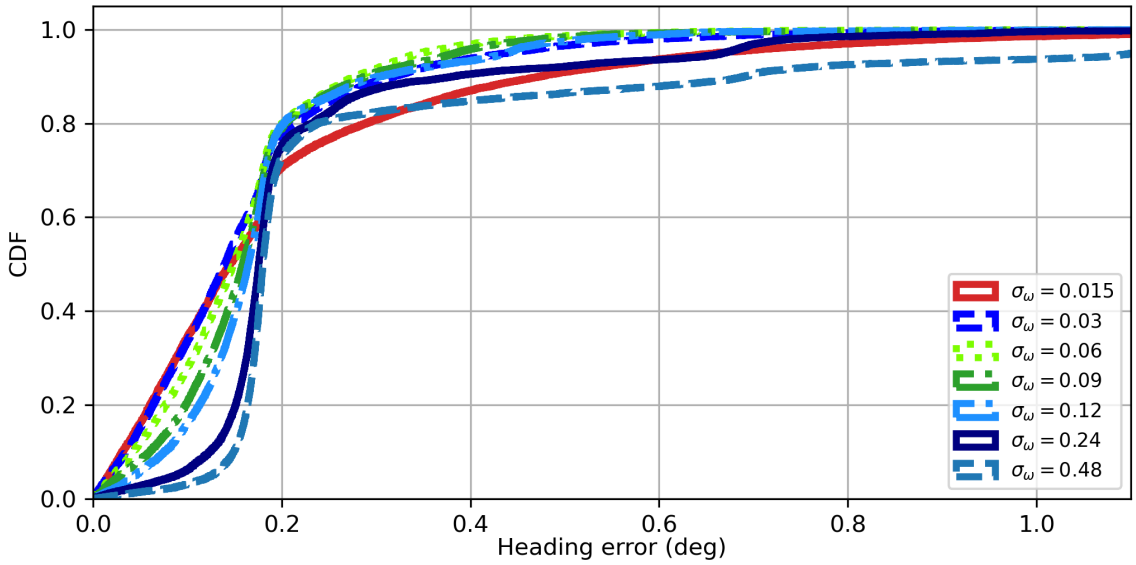

Figure 7.11. Plot showing the CDF for heading estimation error when LOS tracking is used with 2 RRHs on a real-life HST track scenario for various values of σ_ω.

Fig. 7.9 - 7.11 show the CDF for the estimation error for the train location, velocity and heading direction on a real-life HST track using 2 RRHs and various values for σ_ω. The heading estimation is primarily affected by σ_ω as σ_ω is used to model the unknown angular velocity. Similar performance with slight improvement is observed for σ_ω values between 0.03-0.12 and slight degradation for values higher than 0.12 and lower than 0.03. The velocity estimation is unaffected by varying σ_ω. The position estimation is somewhat affected by varying σ_ω. This is due to the changes in heading estimation propagating to position estimation. Thus, in general, changing σ_ω from the value determined from the maximum change in heading direction in simulation (0.03) does not provide a significant improvement in performance. However, in this case using 0.12 will lead to slightly better performance.

7.5 VARYING THE INTERVAL OF LOCALIZATION

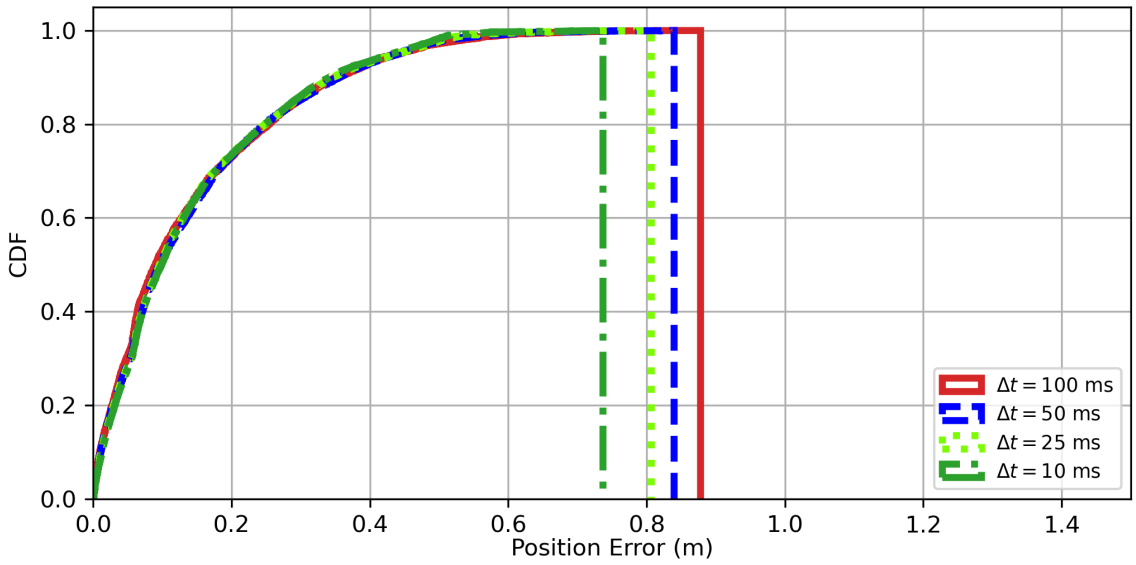

Figure 7.12. Plot showing the CDF for the position estimation error when LOS tracking is used with 2 RRHs on a real-life HST track scenario for various values of Δt.

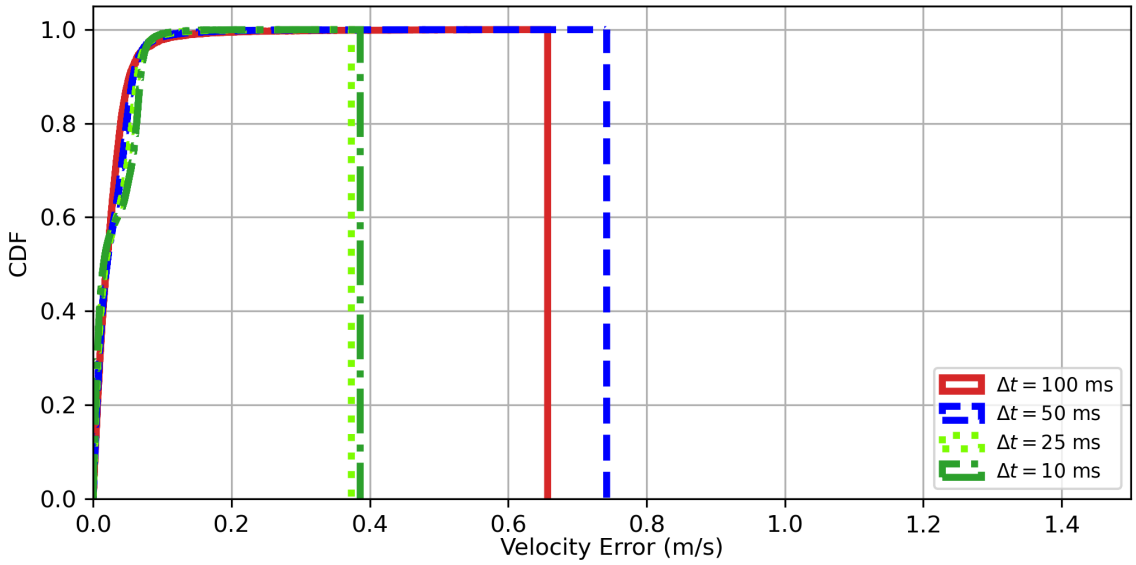

Figure 7.13. Plot showing the CDF for the velocity estimation error when LOS tracking is used with 2 RRHs on a real-life HST track scenario for various values of Δt.

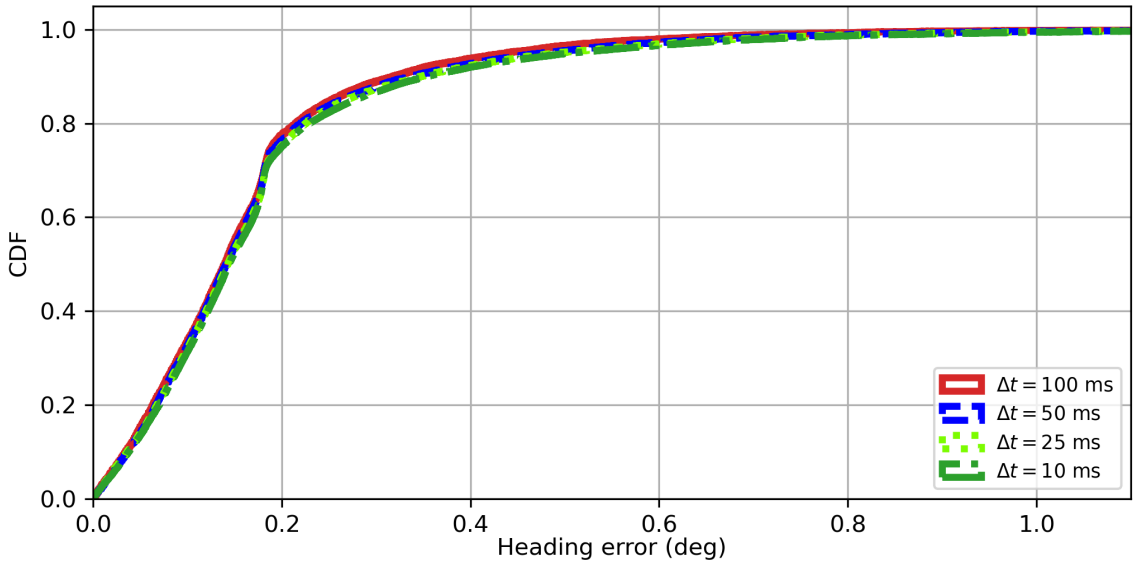

Figure 7.14. Plot showing the CDF for the heading estimation error when LOS tracking is used with 2 RRHs on a real-life HST track scenario for various values of Δt.

The time interval for localization is varied from 100 ms to 10 ms and the HST is localized using 2 RRHs on a real-life HST track. The resulting CDF of the estimation error for the HST's position, velocity and heading can be seen in Fig. 7.12 - 7.14. It can be seen that the position estimation and the heading estimation is unaffected by the change in Δt. The velocity estimation is also not significantly affected by the change in Δt, the maximum value of velocity estimation error simply decreases. This is unexpected as the state evolution function used in the EKF ($\mathbf{f}(.)$) does not fully model the motion of the train on the cubic Bezier curves used to model the real HST track. Thus, increasing Δt should lead to an improvement in estimation performance as the mismatch between $\mathbf{f}(.)$ and the kinematics of the train in simulation is minimized. This simply means that with a Δt of 100 ms $\mathbf{f}(.)$ already estimates the kinematics of the train on a real HST track well and the improvement provided by using smaller values for Δt is not significant.

7.6 VARYING THE NUMBER OF TRANSMIT ANTENNAS

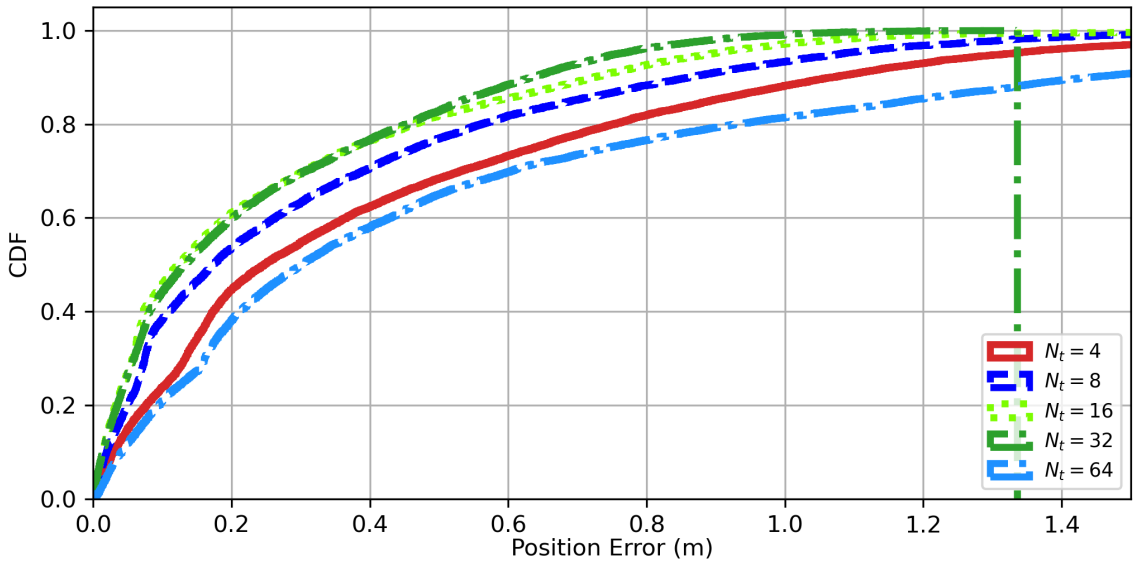

Figure 7.15. Plot showing the CDF for the position estimation error when LOS tracking is used with 2 RRHs on a real-life HST track scenario for various values of antennas used at the RRH (N_t).

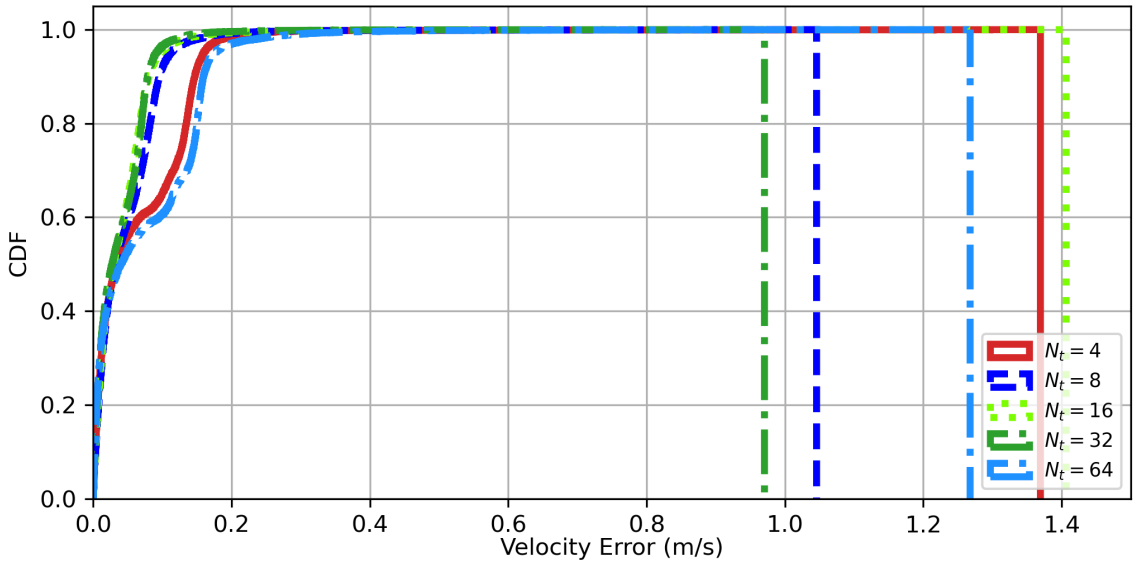

Figure 7.16. Plot showing the CDF for the velocity estimation error when LOS tracking is used with 2 RRHs on a real-life HST track scenario for various values of antennas used at the RRH (N_t).

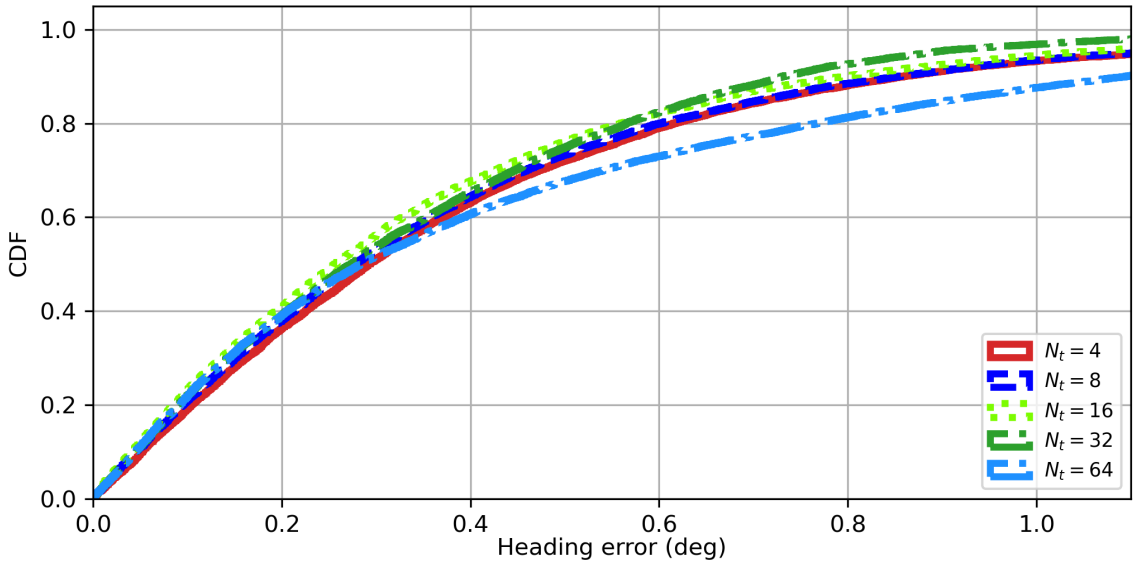

Figure 7.17. Plot showing the CDF for the heading estimation error when LOS tracking is used with 2 RRHs on a real-life HST track scenario for various values of antennas used at the RRH (N_t).

Fig. 7.15 - 7.17 show the CDF for the estimation error plots for the position, velocity and heading on the real-life HST track using 2 RRHs and various values of transmit antennas (N_t) used at the RRH. A similar trend as to what was observed in the localization error for a stationery target when varying transmit antennas in Section 3.5.1 is seen here. The position estimation is affected most significantly, whereas the orientation estimation is somewhat affected. The velocity estimation is affected due to the effect on localization estimation. The estimation accuracy improves as the number of transmit antennas used increase. However, it degrades when too many antennas are used. This is explained by the narrowing of the beam-width as discussed in Section 3.5.1. Using 16 to 32 transmit antennas is ideal, and the number of symbols used needs to be increased if any more transmit antennas are used.

7.7 VARYING THE NUMBER OF RECEIVE ANTENNAS

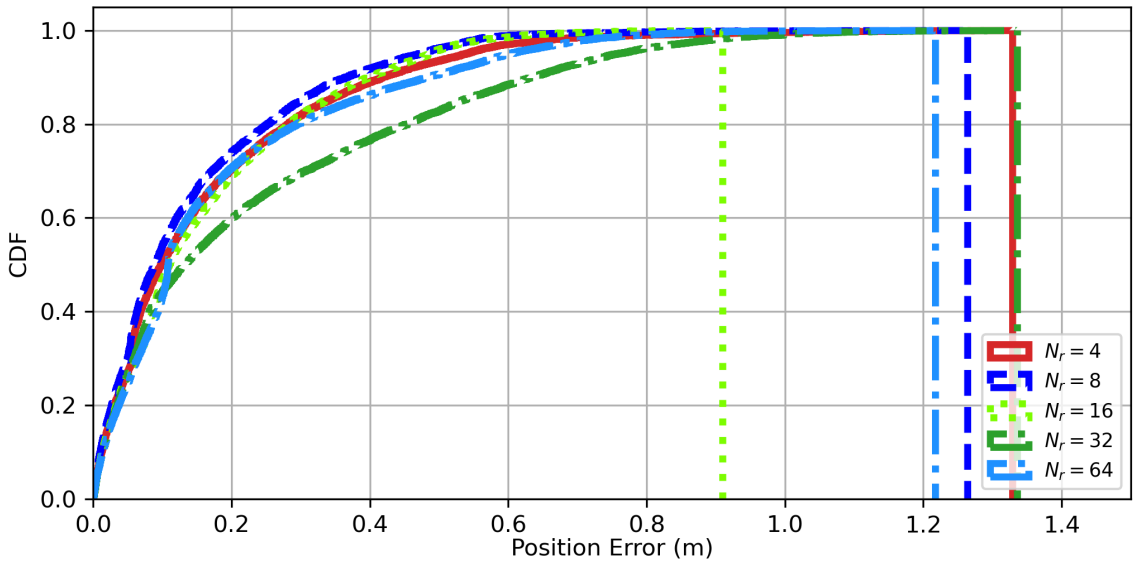

Figure 7.18. Plot showing the CDF for the position estimation error when LOS tracking is used with 2 RRHs on a real-life HST track scenario for various values of N_r.

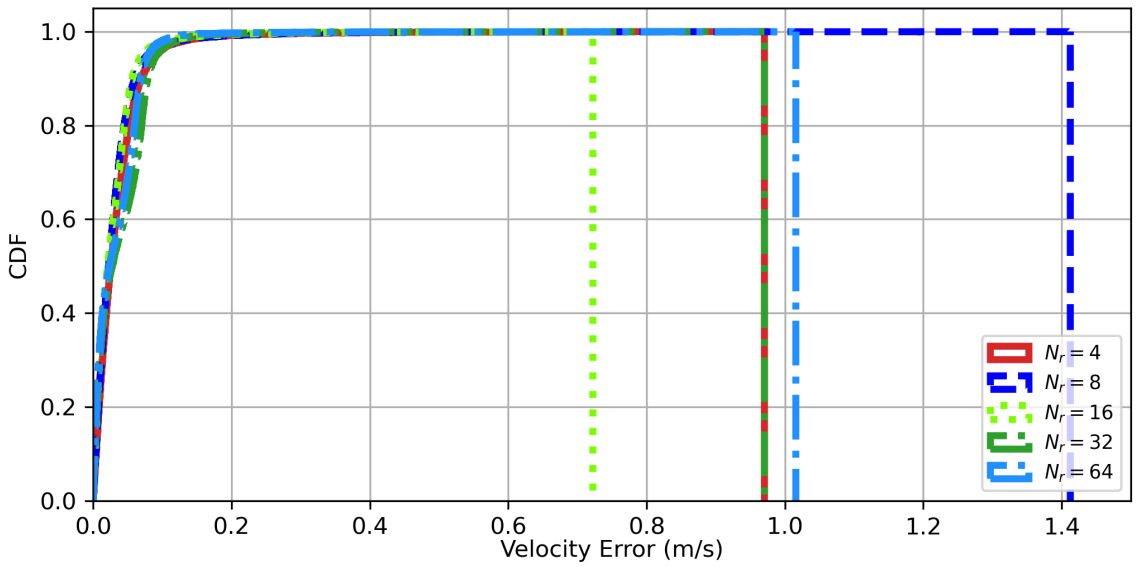

Figure 7.19. Plot showing the CDF for the velocity estimation error when LOS tracking is used with 2 RRHs on a real-life HST track scenario for various values of N_r.

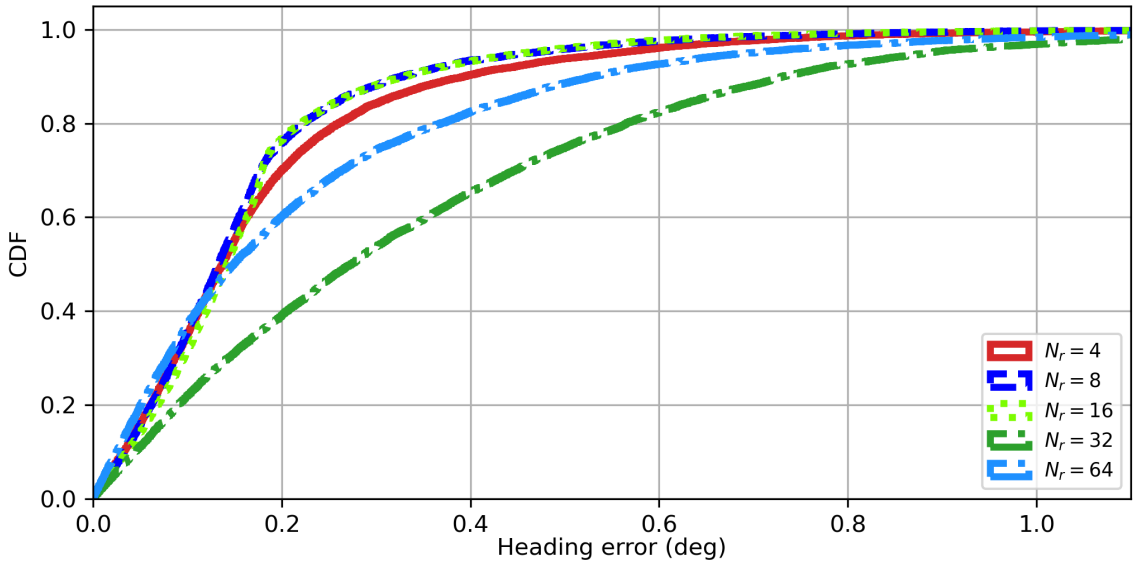

Figure 7.20. Plot showing the CDF for the heading estimation error when LOS tracking is used with 2 RRHs on a real-life HST track scenario for various values of N_r.

The estimation error for the location, velocity and heading of the HST, on the simulated real-life HST track using 2 RRHs for localization with varying number of receive antennas on the train (N_r), can be seen in Fig. 7.18 - 7.20. To no surprise, trends similar to those seen for the estimation error for a stationary target in Section 3.5.2 are observed. The velocity estimation is unaffected, the position estimation is also unaffected except for $N_r = 32$. The heading estimation is more significantly affected by varying N_r. The estimation accuracy improves as N_r increases. However, it drops significantly for $N_r = 32$, followed by improving again for $N_r = 64$. Using 4-8 antennas at the receiver is ideal and anything more does not provide any significant improvement in performance.

7.8 VARYING THE SYMBOLS USED

The estimation error when the symbols used for localization are varied can be seen in Fig. 7.21 - 7.23. As discussed in Section 3.5.3, the number of symbols used greatly affect the estimation accuracy for all parameters. The general trend is that as M increases, the estimation accuracy increases. The ideal value to use for M is 32, anything higher than 32 does not provide any significant improvement in performance.

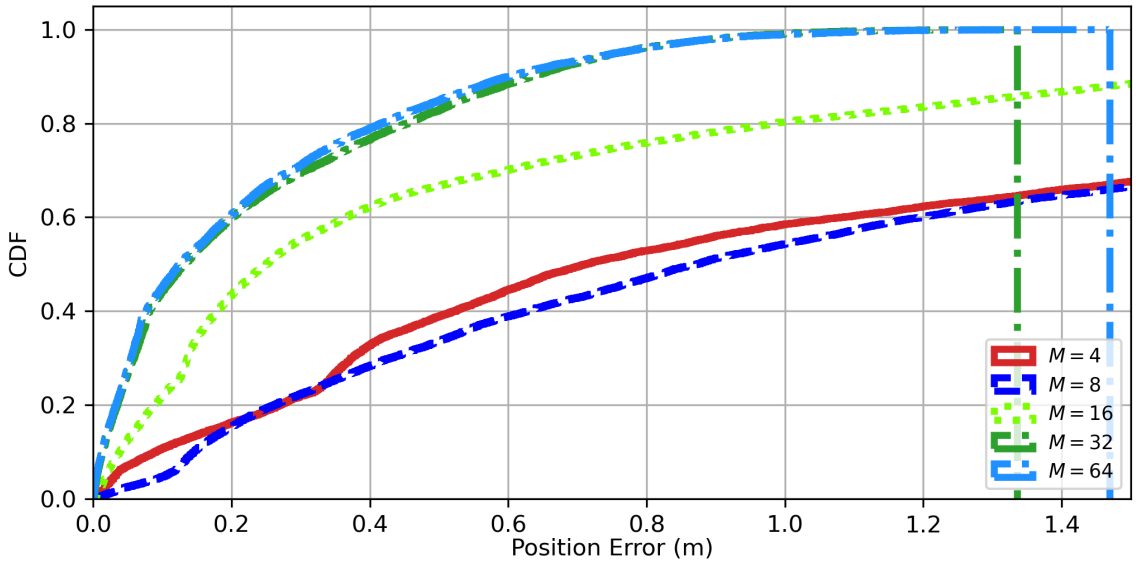

Figure 7.21. Plot showing the CDF for the position estimation error when LOS tracking is used with 2 RRHs on a real-life HST track scenario for various values of symbols used for localization (M).

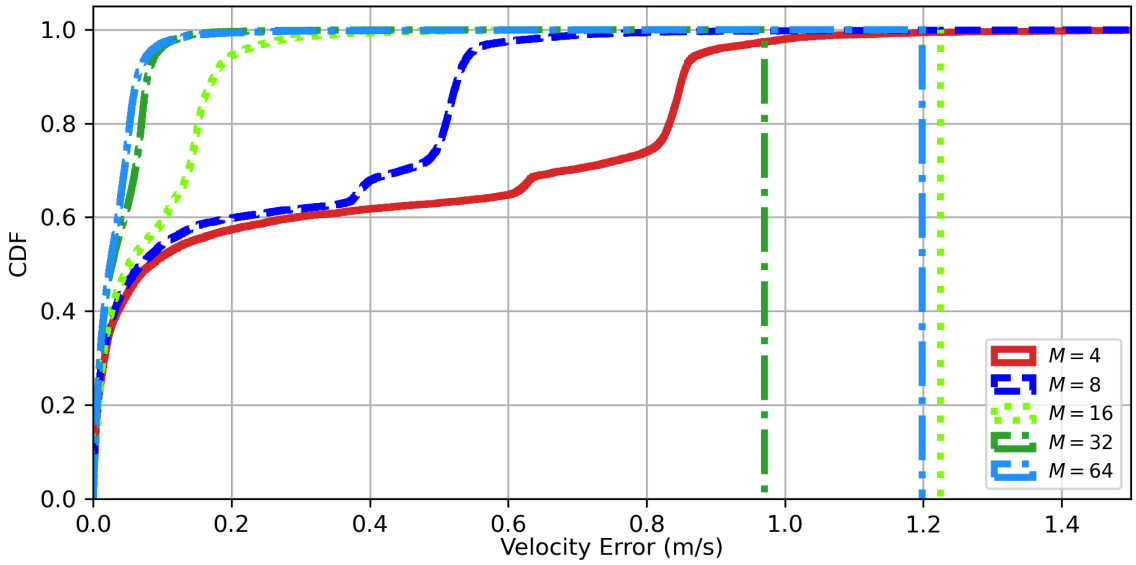

Figure 7.22. Plot showing the CDF for the velocity estimation error when LOS tracking is used with 2 RRHs on a real-life HST track scenario for various values of symbols used for localization (M).

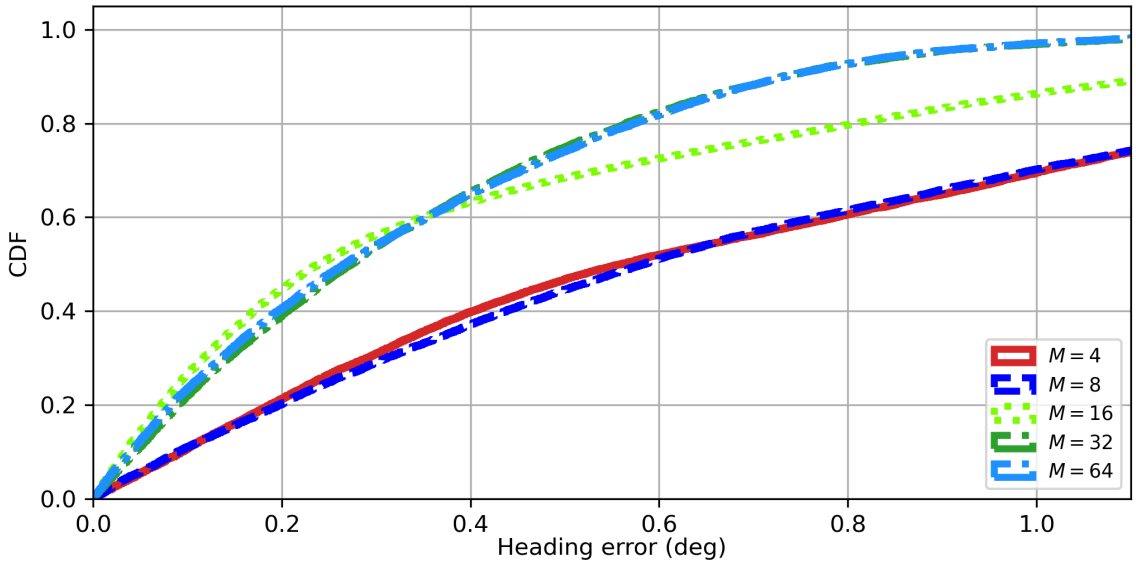

Figure 7.23. Plot showing the CDF for the heading estimation error when LOS tracking is used with 2 RRHs on a real-life HST track scenario for various values of symbols used for localization (M).

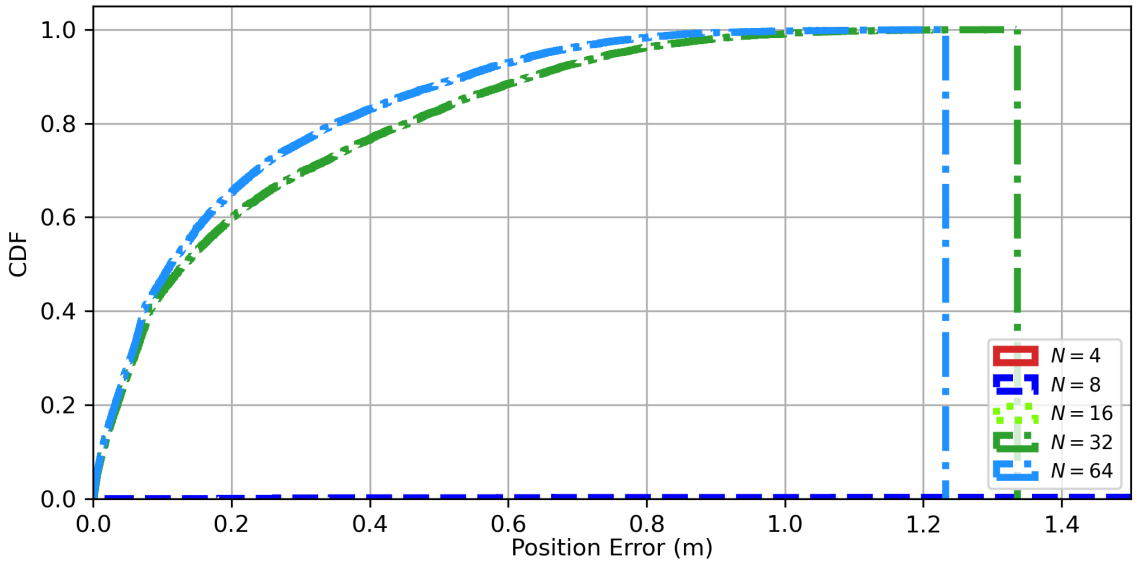

Figure 7.24. Plot showing the CDF for the position estimation error when LOS tracking is used with 2 RRHs on a real-life HST track scenario for various values of N.

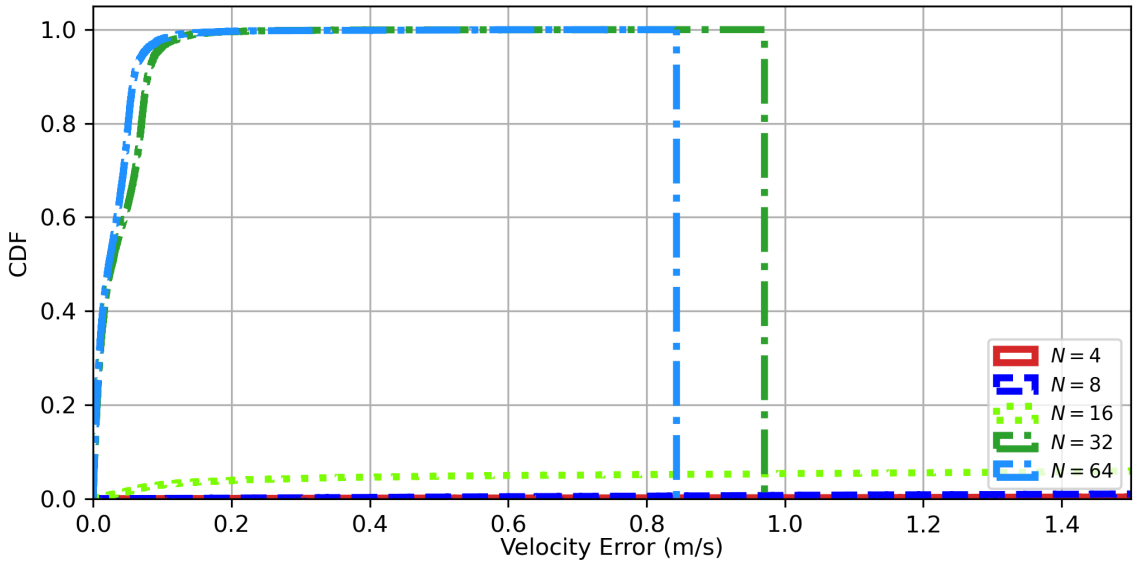

Figure 7.25. Plot showing the CDF for the velocity estimation error when LOS tracking is used with 2 RRHs on a real-life HST track scenario for various values of N.

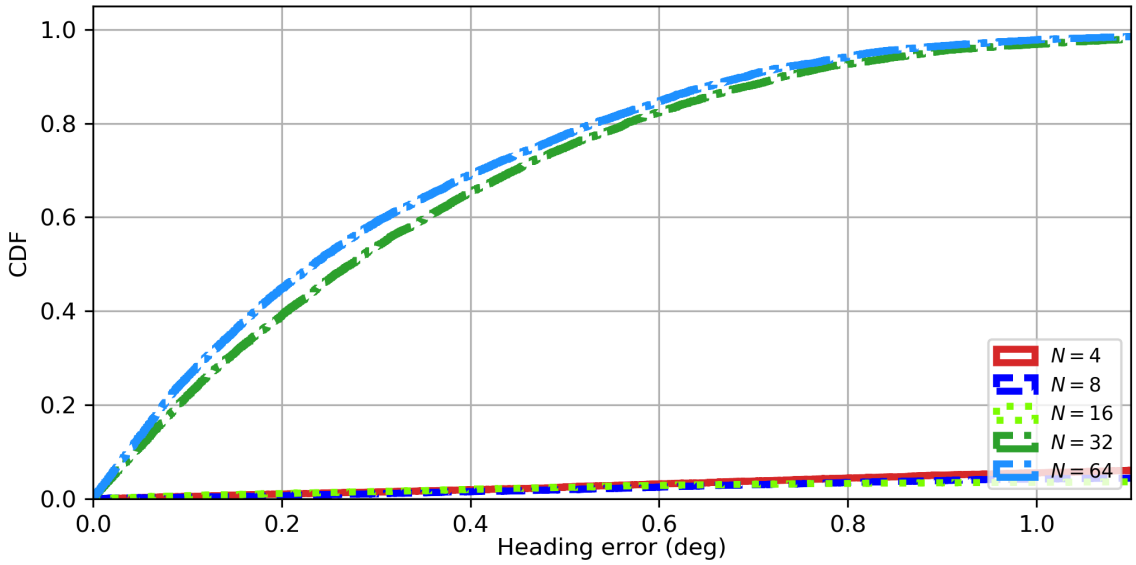

Figure 7.26. Plot showing the CDF for the heading estimation error when LOS tracking is used with 2 RRHs on a real-life HST track scenario for various values of N.

7.9 VARYING THE NUMBER OF CARRIERS USED

The accuracy achieved for position, velocity and heading estimation when different values of carriers are used for localization can be seen in Fig. 7.24 - 7.26. It is clear that the number of carriers used has the greatest influence on the estimation accuracy of all parameters, as it was seen in Section 3.5.4. Increasing the number of carriers used for localization leads to an increase in estimation accuracy for all parameters. However, the performance gain observed between $N = 32$ and $N = 64$ is very small. Thus, sufficient estimation accuracy can be achieved using just 32 carriers for localization.

7.10 MINIMUM PARAMETER VALUES

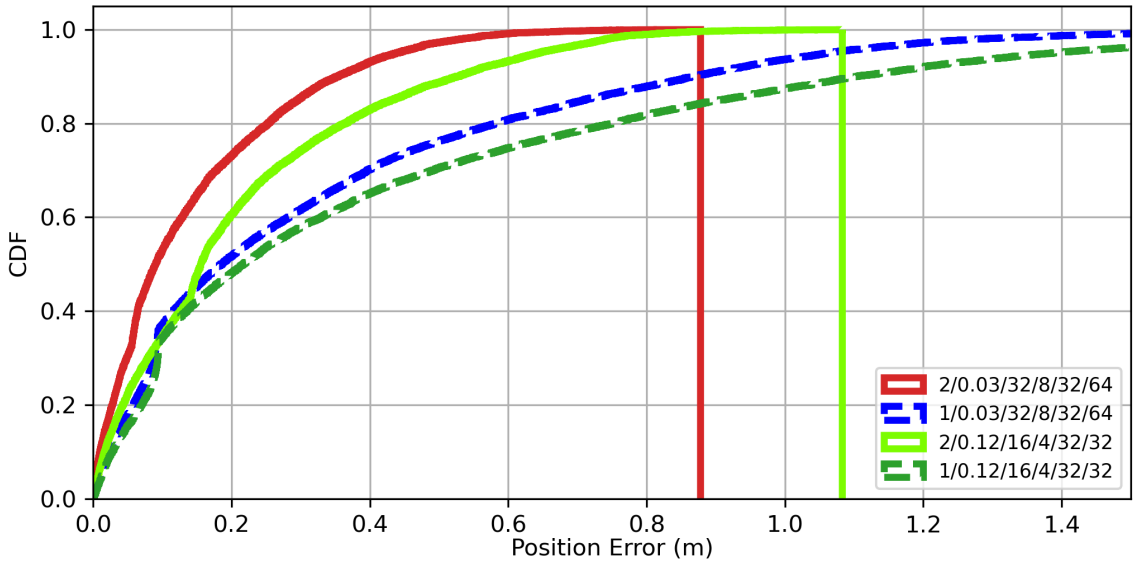

Figure 7.27. Plot showing the CDF for the position estimation error when LOS tracking is used on a real-life HST track scenario. The parameters used are listed in the plot legend as $N_{RRH}/\sigma_\omega/N_t/N_r/M/N$.

Fig. 7.27 - 7.29 show the estimation error for the LOS tracking algorithm for various parameter values on a real-life HST track. The first two plots are generated using the parameters used before, whereas the last two plots are generated using minimum parameters obtained from the simulations in the previous sections. It is clear that the estimation accuracy using smaller parameter values is lower compared to the original parameter values. However, the minimum performance requirements set by 3GPP are still met even when one RRH is used for localization. Using 2 RRHs, the location and the estimation error is less than 1 m and 1 m/s for 99.9%-100% of the simulated trajectory. Whereas for the heading estimation, the 99.9th percentile of error is 1.11°. With one RRH, the 99th percentile of estimation

error for location, velocity and heading is 2.15 m, 0.22 m/s and 1.4°. The achieved performance with one RRH is still better in comparison to the estimation accuracy achieved by TDOA based method in [5] using five RRHs.

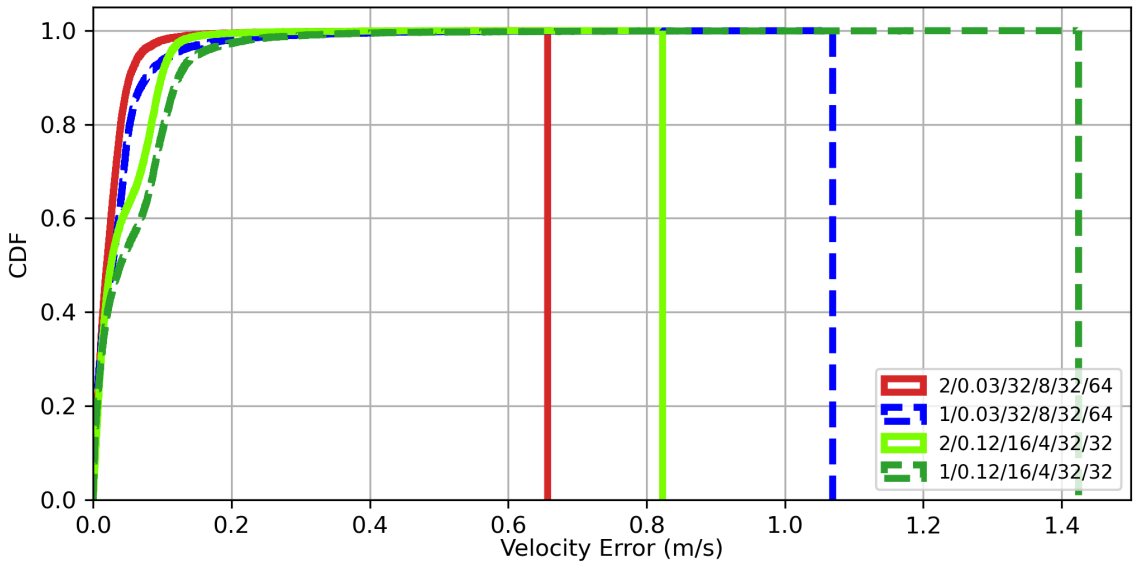

Figure 7.28. Plot showing the CDF for the velocity estimation error when LOS tracking is used on a real-life HST track scenario. The parameters used are listed in the plot legend as $N_{RRH}/\sigma_\omega/N_t/N_r/M/N$.

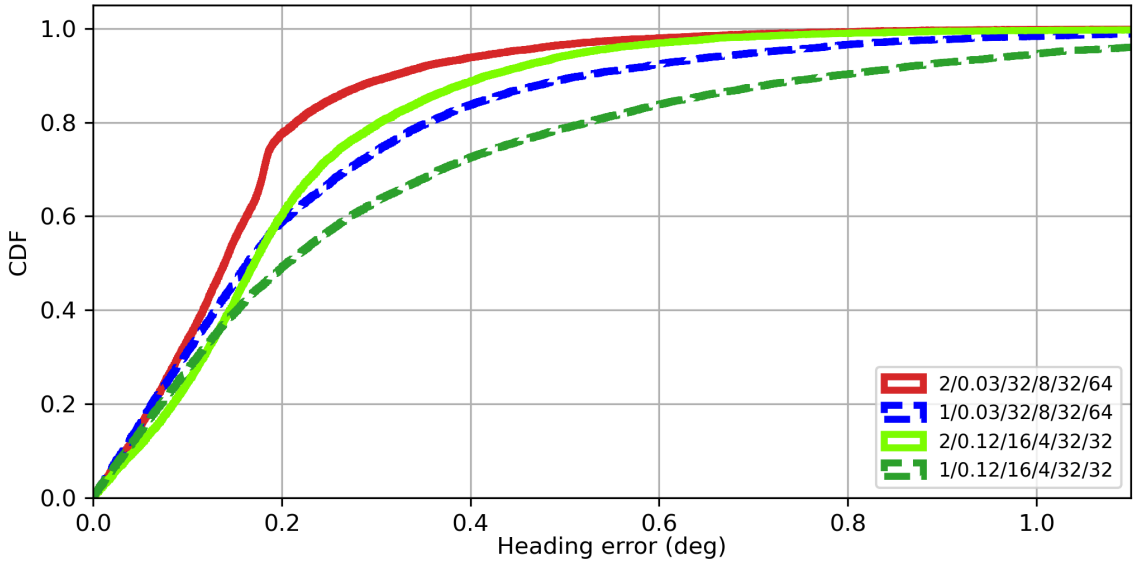

Figure 7.29. Plot showing the CDF for the heading estimation error when LOS tracking is used on a real-life HST track scenario. The parameters used are listed in the plot legend as $N_{RRH}/\sigma_\omega/N_t/N_r/M/N$.

7.11 CONCLUDING REMARKS

This chapter presents the results obtained from simulating the proposed algorithm in various different scenarios. The CDF of the estimation error for the location, velocity and heading estimation is presented and discussed for each scenario.

From the simulation results on the straight track scenario and the real-life HST track scenario, several observations are made. Firstly, using LOS tracking provides an improvement in performance in comparison to when LOS tracking is not used. On the straight track scenario, a location and velocity estimation error of less than 1 m and 1 m/s was achieved throughout the simulated trajectory using just one RRH for localization. On the real-life HST track on the other hand, a location and velocity estimation error of less than 1 m and 1 m/s was achieved throughout the simulated trajectory and sub-degree orientation estimation error was achieved for 99.9% of the trajectory using two RRHs. With one RRH the 99th percentile of estimation error for the train's location, velocity and heading was 1.46 m, 0.18 m/s and 1°. Thus, using two RRHs, the upper limit of desired estimation performance is achieved. Whereas with one RRH, the lower limit for estimation accuracy specified by the 3GPP in [65] is achieved. Furthermore, the algorithm performs better than existing TDOA based localization algorithms [2, 5] for both the straight track scenario and real-life HST track scenario using just one RRH for localization.

The process noise and the localization interval were looked at to investigate their effect on estimation accuracy. Based on the results obtained it was concluded that neither the process noise nor the interval of localization had a significant effect on the estimation performance. For σ_α and σ_ω, using the maximum change in α (3.5) and ω (0.03) generally leads to the best performance. For the current scenario, setting σ_ω to 0.12 provides slightly better performance.

The various system parameters (N_t, N_r, M and N) were also investigated to determine their effect on estimation performance. Similar trends as observed for localization of a stationery target in Section 3.5 are observed here as well. The number of carriers used and the number of symbols used have the greatest effect on estimation performance. From each of the simulations, the minimum parameter values that provide satisfactory performance are also identified.

At the end, the minimum parameter values identified in the previous simulations were simulated to see if satisfactory performance is still achieved. The results showed that the performance degrades

compared to previously used parameters. However, satisfactory performance is still achieved, as with two RRHs a position estimation and velocity estimation error of less than 1 m and 1 m/s is achieved for 99.9%-100% of the simulated trajectory, whereas with one RRH the estimation accuracy for location, velocity and heading meet the requirements set by the 3GPP in [65] for the use case of machine control and intelligent transportation. Furthermore, the achieved performance using the minimum parameter values with one RRH is still better in comparison to the estimation accuracy achieved by TDOA based method in [5] using five RRHs.

CHAPTER 8 CONCLUSION

8.1 SUMMARY

The dissertation starts with a summary of the existing literature in fields of localization and tracking of HSTs and 5G localization in Chapter 2. The state-of-the-art HST localization and tracking solutions proposed in literature are discussed first. This is followed by a discussion on the fundamentals of radio localization using telecommunications infrastructure. The various methods proposed in literature for localization using 5G infrastructure are discussed next. Furthermore, studies in which 5G localization algorithms are applied to a problem, such as tracking of HSTs, are also discussed. It is concluded that a new algorithm for localizing a HST is required and that 5G localization algorithms are ideal candidates for this.

The compressed sensing based 5G localization algorithm proposed for use in localization of HSTs is discussed in Chapter 3. The system model assumed by the localization algorithm is discussed first. The DCS-SOMP algorithm, as proposed in [6–8], for localizing a stationary MT is discussed next - with emphasis on the performance achievable by the algorithm. After this the modified version of this algorithm to include LOS tracking to allow for more reliable and accurate localization is discussed. The proposed algorithm was compared to the original algorithm to ensure that the desired improvements are achieved. It is found that with LOS tracking the algorithm can localize a stationery target more reliably. Finally, the various different system parameters were varied to determine the effect on localization performance. It is found that the number of carriers used and the number of symbols used have the most significant effect on localization performance.

Chapter 4 discusses the EKF used for tracking the train. The theory behind the EKF is discussed first, followed by the specifics of its implementation in the HST scenario.

The complete localization and tracking algorithm proposed for tracking a HST is discussed in Chapter 5. The way the localization and tracking algorithms interact with each other is discussed first. This is followed by a description of how the measurement limits for LOS tracking, beamforming and outlier detection are obtained.

In Chapter 6 the experimental setup is discussed. This consists of a discussion on the system model used in simulation, followed by a discussion on the channel model used in simulation. Finally the parameters used in different simulations are discussed.

The simulation setup described in Chapter 6 was created in Python and the results obtained from it are presented and discussed in Chapter 7. First the estimation accuracy of the proposed algorithm using LOS tracking is compared to the original DCS-SOMP algorithm for a straight track scenario and a real-life HST track scenario for various values of RRHs used for localization. It is found that with LOS tracking the algorithm performed much better compared to when LOS tracking is not used. On the straight track scenario a location and velocity estimation error of less than 1 m and 1 m/s is achieved throughout the simulated trajectory using just one RRH for localization. On the real-life HST track on the other hand, a location and velocity estimation error of less than 1 m and 1 m/s is achieved throughout the simulated trajectory and sub-degree orientation estimation error is achieved for 99.9% of the trajectory using two RRHs. With one RRH the 99th percentile of estimation error for the train's location, velocity and heading is 1.46 m, 0.18 m/s and 1° respectively. Thus, using two RRHs the upper limit of desired estimation performance is achieved, whereas with one RRH the lower limit for estimation accuracy specified by the 3GPP in [65] is achieved. Furthermore, the results also indicated that the algorithm performs better than existing TDOA based 5G localization algorithms [2, 5] for both the straight track scenario and real-life HST track scenario using just one RRH for localization.

The parameters for the EKF (σ_α, σ_ω and Δt) were varied to investigate their effect on localization performance. It is found that the σ_α, σ_ω and Δt do not significantly affect the the estimation performance and the process noise variance (σ_α and σ_ω) can be set using the maximum change in α and ω. The various system parameters (N_t, N_r, M and N) are also investigated to determine their effect on estimation performance. Similar trends as observed for localization of a stationery target in Section 3.5 are observed here. The number of carriers used and the number of symbols used have the greatest effect on estimation performance. From each of the simulations the minimum parameter values that provide satisfactory performance were also identified.

At the end the minimum parameter values identified in the previous simulations were simulated to see if satisfactory performance is still achieved. The results showed that the performance degrades compared to previously used parameters. However, satisfactory performance is still achieved, as with two RRHs a position estimation and velocity estimation error of less than 1 m and 1 m/s is achieved for 99.9%-100% of the simulated trajectory, whereas with one RRH the estimation accuracy for location, velocity and heading meet the requirements set by the 3GPP in [65] for the use case of machine control and intelligent transportation. Even using the minimum parameter values and one RRH, the achieved performance is better in comparison to existing TDOA based 5G localization algorithms from [5].

8.2 FUTURE WORK

While the research conducted here shows that the proposed algorithm is a viable solution for localization and tracking of HSTs, it can be further extended to improve estimation performance and further verify usability of the algorithm as follows,

- The proposed algorithm needs to be tested on a more realistic channel model that accurately models when the RRHs and train are in LOS and not in LOS of each other.
- The algorithm performance needs to be evaluated under more realistic synchronization scenarios that typically occur at high-speeds to ensure that the proposed algorithm is still viable.
- The proposed algorithm needs to implemented and tested on a real HST to verify the performance achievable by the algorithm in the presence of real-world hardware and software limitations.
- As the kinematics of trains are restricted by the tracks, the performance of the tracking algorithm can be improved by incorporating map data. Therefore, SLAM algorithms need to be investigated for this problem.

8.3 CONCLUDING REMARKS

A novel compressed sensing based 5G localization algorithm for the localization and tracking of HSTs is proposed in this dissertation. It is shown that this algorithm can accurately track a HST in various scenarios with various parameter values. The desired performance requirements for the algorithm are met. Furthermore, the observed performance is significantly better in comparison to existing 5G localization solutions for tracking HSTs.

REFERENCES

[1] T. Levanen, J. Talvitie, R. Wichman, V. Syrjala, M. Renfors, and M. Valkama, "Location-aware 5G communications and Doppler compensation for high-speed train networks," in *2017 European Conference on Networks and Communications (EuCNC)*, 2017, pp. 1–6.

[2] J. Talvitie, T. Levanen, M. Koivisto, T. Ihalainen, K. Pajukoski, and M. Valkama, "Positioning and Location-Aware Communications for Modern Railways with 5G New Radio," *IEEE Communications Magazine*, vol. 57, no. 9, pp. 24–30, 2019.

[3] J. Talvitie, T. Levanen, M. Koivisto, K. Pajukoski, M. Renfors, and M. Valkama, "Positioning of high-speed trains using 5G new radio synchronization signals," in *IEEE Wireless Communications and Networking Conference, WCNC*, 2018, pp. 1–6.

[4] J. Talvitie, T. Levanen, M. Koivisto, T. Ihalainen, K. Pajukoski, M. Renfors, and M. Valkama, "Positioning and Location-Based Beamforming for High Speed Trains in 5G NR Networks," in *2018 IEEE Globecom Workshops, GC Wkshps 2018 - Proceedings*, 2019.

[5] J. Talvitie, T. Levanen, M. Koivisto, and M. Valkama, "Positioning and tracking of high-speed trains with non-linear state model for 5G and beyond systems," in *Proceedings of the International Symposium on Wireless Communication Systems*, 2019, pp. 309–314.

[6] A. Shahmansoori, G. E. Garcia, G. Destino, G. Seco-Granados, and H. Wymeersch, "Position and Orientation Estimation Through Millimeter-Wave MIMO in 5G Systems," *IEEE Transactions on Wireless Communications*, vol. 17, no. 3, pp. 1822–1835, 2018.

[7] J. Talvitie, M. Valkama, G. Destino, and H. Wymeersch, "Novel Algorithms for High-Accuracy Joint Position and Orientation Estimation in 5G mmWave Systems," in *2017 IEEE Globecom Workshops, GC Wkshps 2017 - Proceedings*, 2018, pp. 1–7.

[8] J. Talvitie, M. Koivisto, T. Levanen, M. Valkama, G. Destino, and H. Wymeersch, "High-Accuracy Joint Position and Orientation Estimation in Sparse 5G mmWave Channel," in *IEEE International Conference on Communications*, 2019, pp. 9–15.

[9] 3GPP, "5G: Study on scenarios and requirements for next generation access technologies," 3GPP, Tech. Rep. TR 38.913 (14.3.0), Oct. 2017, Accessed on: Jun. 25, 2021. [Online]. Available: https://www.3gpp.org/ftp//Specs/archive/38_series/38.913/38913-e30.zip

[10] S. Bedrich and X. Gu, "GNSS-based sensor fusion for safety-critical applications in rail traffic," *Galileo and EGNOS Information Catalogue*, p. 8, 2004.

[11] W. Jiang, S. Chen, B. Cai, J. Wang, W. Shangguan, and C. Rizos, "A multi-sensor positioning method-based train localization system for low density line," *IEEE Transactions on Vehicular Technology*, vol. 67, no. 11, pp. 10 425–10 437, 2018.

[12] O. Heirich, P. Robertson, A. C. García, T. Strang, and A. Lehner, "Probabilistic localization method for trains," in *IEEE Intelligent Vehicles Symposium, Proceedings*, 2012, pp. 482–487.

[13] O. Heirich, P. Robertson, A. C. García, and T. Strang, "Bayesian train localization method extended by 3D geometric railway track observations from inertial sensors," in *15th International Conference on Information Fusion*, 2012, pp. 416–423.

[14] O. Heirich, "Bayesian Train Localization with Particle Filter, Loosely Coupled GNSS, IMU, and a Track Map," *Journal of Sensors*, vol. 2016, 2016, Art. ID 2672640.

[15] S. Hensel, C. Hasberg, and C. Stiller, "Probabilistic rail vehicle localization with eddy current sensors in topological maps," *IEEE Transactions on Intelligent Transportation Systems*, vol. 12, no. 4, pp. 1525–1536, 2011.

[16] B. Siebler, O. Heirich, and S. Sand, "Train Localization with Particle Filter and Magnetic Field Measurements," in *2018 21st International Conference on Information Fusion*. ISIF, 2018, pp. 1715–1719.

[17] M. Lauer and D. Stein, "A Train Localization Algorithm for Train Protection Systems of the Future," *IEEE Transactions on Intelligent Transportation Systems*, vol. 16, no. 2, pp. 970–979, 2015.

[18] O. Heirich, P. Robertson, and T. Strang, "RailSLAM - Localization of rail vehicles and mapping of geometric railway tracks," in *Proceedings - IEEE International Conference on Robotics and Automation*, 2013, pp. 5212–5219.

[19] C. Hasberg, S. Hensel, and C. Stiller, "Simultaneous localization and mapping for path-constrained motion," *IEEE Transactions on Intelligent Transportation Systems*, vol. 13, no. 2, pp. 541–552, 2012.

[20] T. Daoust, F. Pomerleau, and T. D. Barfoot, "Light at the end of the tunnel: High-speed lidar-based train localization in challenging underground environments," in *Proceedings - 2016 13th Conference on Computer and Robot Vision*, 2016, pp. 93–100.

[21] R. Ross, "Track and turnout detection in video-signals using probabilistic spline curves," in *IEEE Conference on Intelligent Transportation Systems, Proceedings, ITSC*, 2012, pp. 294–299.

[22] J. A. Del Peral-Rosado, R. Raulefs, J. A. López-Salcedo, and G. Seco-Granados, "Survey of Cellular Mobile Radio Localization Methods: From 1G to 5G," *IEEE Communications Surveys and Tutorials*, vol. 20, no. 2, pp. 1124–1148, 2018.

[23] A. Tahat, G. Kaddoum, S. Yousefi, S. Valaee, and F. Gagnon, "A Look at the Recent Wireless Positioning Techniques with a Focus on Algorithms for Moving Receivers," *IEEE Access*, vol. 4, pp. 6652–6680, 2016.

[24] P. Zhang, J. Lu, Y. Wang, and Q. Wang, "Cooperative localization in 5G networks: A survey," *ICT Express*, vol. 3, no. 1, pp. 27–32, 2017.

[25] C. Laoudias, A. Moreira, S. Kim, S. Lee, L. Wirola, and C. Fischione, "A survey of enabling technologies for network localization, tracking, and navigation," *IEEE Communications Surveys and Tutorials*, vol. 20, no. 4, pp. 3607–3644, 2018.

[26] A. Guerra, F. Guidi, and D. Dardari, "Position and orientation error bound for wideband massive antenna arrays," in *2015 IEEE International Conference on Communication Workshop, ICCW 2015*, 2015, pp. 853–858.

[27] ——, "Single-Anchor Localization and Orientation Performance Limits Using Massive Arrays: MIMO vs. Beamforming," *IEEE Transactions on Wireless Communications*, vol. 17, no. 8, pp. 5241–5255, 2018.

[28] Z. Abu-Shaban, X. Zhou, T. Abhayapala, G. Seco-Granados, and H. Wymeersch, "Error Bounds for Uplink and Downlink 3D Localization in 5G Millimeter Wave Systems," *IEEE Transactions on Wireless Communications*, vol. 17, no. 8, pp. 4939–4954, 2018.

[29] Z. Abu-Shaban, H. Wymeersch, T. D. Abhayapala, and G. Seco-Granados, "Single-Anchor Two-Way Localization Bounds for 5G mmWave Systems," *IEEE Transactions on Vehicular Technology*, vol. 69, no. 6, pp. 6388–6400, 2020.

[30] F. Ghaseminajm, Z. Abu-Shaban, S. S. Ikki, H. Wymeersch, and C. R. Benson, "Localization Error Bounds for 5G mmWave Systems under I/Q Imbalance," *IEEE Transactions on Vehicular Technology*, vol. 69, no. 7, pp. 7971–7975, 2020.

[31] S. Safavi, U. A. Khan, S. Kar, and J. M. Moura, "Distributed Localization: A Linear Theory," *Proceedings of the IEEE*, vol. 106, no. 7, pp. 1204–1223, 2018.

[32] H. Kim, S. W. Choi, and S. Kim, "Connectivity information-aided belief propagation for cooperative localization," *IEEE Wireless Communications Letters*, vol. 7, no. 6, pp. 1010–1013, 2018.

[33] L. Gazzah and L. Najjar, "Enhanced cooperative group localization with identification of LOS/NLOS BSs in 5G dense networks," *Ad Hoc Networks*, vol. 89, pp. 88–96, 2019.

[34] V. Savic and E. G. Larsson, "Fingerprinting-based positioning in distributed massive MIMO systems," in *2015 IEEE 82nd Vehicular Technology Conference, VTC Fall 2015 - Proceedings*, 2016, pp. 1–5.

[35] A. Decurninge, L. G. Ordóñez, P. Ferrand, H. Gaoning, L. Bojie, Z. Wei, and M. Guillaud, "CSI-based Outdoor Localization for Massive MINO: Experiments with a Learning Approach," in *Proceedings of the International Symposium on Wireless Communication Systems*, 2018, pp. 1–6.

[36] D. Wang, G. Hosangadi, P. Monogioudis, and A. Rao, "Mobile Device Localization in 5G Wireless Networks," in *2019 International Conference on Computing, Networking and Communications*, 2019, pp. 185–190.

[37] N. Garcia, H. Wymeersch, E. G. Larsson, A. M. Haimovich, and M. Coulon, "Direct localization for massive MIMO," *IEEE Transactions on Signal Processing*, vol. 65, no. 10, pp. 2475–2487, 2017.

[38] G. Liu, A. Liu, L. Lian, V. Lau, and M. J. Zhao, "Sparse Bayesian inference based direct localization for massive MIMO," in *IEEE Vehicular Technology Conference*, 2019, pp. 6–10.

[39] N. Vukmirović, M. Janjić, P. M. Djurić, and M. Erić, "Position estimation with a millimeter-wave massive MIMO system based on distributed steerable phased antenna arrays," *Eurasip Journal on Advances in Signal Processing*, vol. 2018, no. 1, pp. 1–17, 2018.

[40] N. Vukmirović, M. Erić, M. Janjić, and P. M. Djurić, "Direct wideband coherent localization by distributed antenna arrays," *Sensors (Switzerland)*, vol. 19, no. 20, p. 4582, 2019.

[41] A. Sellami, L. Nasraoui, and L. N. Atallah, "Multi-Stage Localization for Massive MIMO 5G Systems," in *IEEE Vehicular Technology Conference*, 2020, pp. 1–6.

[42] E. Y. Menta, N. Malm, R. Jantti, K. Ruttik, M. Costa, and K. Leppanen, "On the Performance of AoA-Based Localization in 5G Ultra-Dense Networks," *IEEE Access*, vol. 7, pp. 33 870–33 880, 2019.

[43] Y. S. Chen, D. J. Deng, and C. C. Teng, "Range-Based Localization Algorithm for Next Generation Wireless Networks Using Radical Centers," *IEEE Access*, vol. 4, pp. 2139–2153, 2016.

[44] K. Witrisal, P. Meissner, E. Leitinger, Y. Shen, C. Gustafson, F. Tufvesson, K. Haneda, D. Dardari, A. F. Molisch, A. Conti, and M. Z. Win, "High-accuracy localization for assisted living: 5G systems will turn multipath channels from foe to friend," *IEEE Signal Processing Magazine*, vol. 33, no. 2, pp. 59–70, 2016.

[45] A. Shahmansoori, B. Uguen, G. Destino, G. Seco-Granados, and H. Wymeersch, "Tracking Position and Orientation through Millimeter Wave Lens MIMO in 5G Systems," *IEEE Signal Processing Letters*, vol. 26, no. 8, pp. 1222–1226, 2019.

[46] M. Koivisto, M. Costa, J. Werner, K. Heiska, J. Talvitie, K. Leppanen, V. Koivunen, and M. Valkama, "Joint Device Positioning and Clock Synchronization in 5G Ultra-Dense Networks," *IEEE Transactions on Wireless Communications*, vol. 16, no. 5, pp. 2866–2881, 2017.

[47] P. Kela, M. Costa, J. Turkka, M. Koivisto, J. Werner, A. Hakkarainen, M. Valkama, R. Jäntti, and K. Leppänen, "Location based beamforming in 5G ultra-dense networks," in *IEEE Vehicular Technology Conference*, 2016, pp. 1–6.

[48] E. Rastorgueva-Foi, M. Costa, M. Koivisto, K. Leppänen, and M. Valkama, "Localization and Tracking in mmWave Radio Networks using Beam-Based DoD Measurements," in *ICL-GNSS 2018 - 2018 8th International Conference on Localization and GNSS: Seamless Indoor-Outdoor Localization, Proceedings*, 2018, pp. 26–28.

[49] E. Rastorgueva-Foi, M. Costa, M. Koivisto, J. Talvitie, K. Leppaneny, and M. Valkama, "Beam-based Device Positioning in mmWave 5G Systems under Orientation Uncertainties," in *Conference Record - Asilomar Conference on Signals, Systems and Computers*, 2019, pp. 3–7.

[50] R. Mendrzik, H. Wymeersch, and G. Bauch, "Joint Localization and Mapping Through Millimeter Wave MIMO in 5G Systems," in *2018 IEEE Global Communications Conference, GLOBECOM 2018 - Proceedings*, 2018, pp. 1–6.

[51] R. Mendrzik, F. Meyer, G. Bauch, and M. Win, "Localization, Mapping, and Synchronization in 5G Millimeter Wave Massive MIMO Systems," in *IEEE Workshop on Signal Processing Advances in Wireless Communications, SPAWC*, 2019, pp. 1–6.

[52] B. Zhou, A. Liu, and V. Lau, "Successive Localization and Beamforming in 5G mmWave MIMO Communication Systems," *IEEE Transactions on Signal Processing*, vol. 67, no. 6, pp. 1620–1635, 2019.

[53] J. H. Brady and A. M. Sayeed, "Wideband communication with high-dimensional arrays: New results and transceiver architectures," in *2015 IEEE International Conference on Communication Workshop (ICCW)*, 2015, pp. 1042–1047.

[54] J. Yang, B. Ai, K. Guan, D. He, X. Lin, B. Hui, J. Kim, and A. Hrovat, "A geometry-based stochastic channel model for the millimeter-wave band in a 3GPP high-speed train scenario," *IEEE Transactions on Vehicular Technology*, vol. 67, no. 5, pp. 3853–3865, 2018.

[55] M. F. Duarte, S. Sarvotham, D. Baron, M. B. Wakin, and R. G. Baraniuk, "Distributed compressed sensing of jointly sparse signals," in *Conference Record - Asilomar Conference on Signals, Systems and Computers*, 2005, pp. 1537–1541.

[56] J. Saloranta and G. Destino, "On the utilization of MIMO-OFDM channel sparsity for accurate positioning," in *2016 24th European Signal Processing Conference (EUSIPCO)*, 2016, pp. 748–752.

[57] M. Arulampalam, S. Maskell, N. Gordon, and T. Clapp, "A tutorial on particle filters for online nonlinear/non-Gaussian Bayesian tracking," *IEEE Transactions on Signal Processing*, vol. 50, no. 2, pp. 174–188, 2002.

[58] M. Roth, G. Hendeby, and F. Gustafsson, "EKF/UKF maneuvering target tracking using coordinated turn models with polar/Cartesian velocity," in *17th International Conference on Information Fusion (FUSION)*, 2014, pp. 1–8.

[59] OpenStreetMap contributors, "Planet dump retrieved from https://planet.osm.org ," https://www.openstreetmap.org , 2017.

[60] J. Godoy, A. Artuñedo, and J. Villagra, "Self-Generated OSM-Based Driving Corridors," *IEEE Access*, vol. 7, pp. 20 113–20 125, 2019.

[61] Y. Liu, C. X. Wang, J. Huang, J. Sun, and W. Zhang, "Novel 3-D Nonstationary MmWave Massive MIMO Channel Models for 5G High-Speed Train Wireless Communications," *IEEE Transactions on Vehicular Technology*, vol. 68, no. 3, pp. 2077–2086, 2019.

[62] S. Wu, C. X. Wang, E. H. M. Aggoune, M. M. Alwakeel, and X. You, "A General 3-D Non-Stationary 5G Wireless Channel Model," *IEEE Transactions on Communications*, vol. 66, no. 7, pp. 3065–3078, 2018.

[63] 3GPP, "Technical Specification Group Radio Access Network, Study on channel model for frequency spectrum above 6 GHz (Release 14)," 3GPP, Tech. Rep. TR 38.901 (14.3.0), Jan. 2018, Accessed on: Jun. 29, 2021. [Online]. Available: https://www.3gpp.org/ftp//Specs/archive/38_series/38.901/38901-e30.zip

[64] M. R. Akdeniz, Y. Liu, M. K. Samimi, S. Sun, S. Rangan, T. S. Rappaport, and E. Erkip, "Millimeter wave channel modeling and cellular capacity evaluation," *IEEE Journal on Selected Areas in Communications*, vol. 32, no. 6, pp. 1164–1179, 2014.

[65] 3GPP, "Study on positioning use cases (Release 16)," 3GPP, Tech. Rep. TR 22.872 (16.1.0), Sep. 2018, Accessed on: Jun. 28, 2021. [Online]. Available: https://www.3gpp.org/ftp//Specs/archive/22_series/22.872/22872-g10.zip

ADDENDUM A CONTROL POINT GENERATION FOR BEZIER CURVES

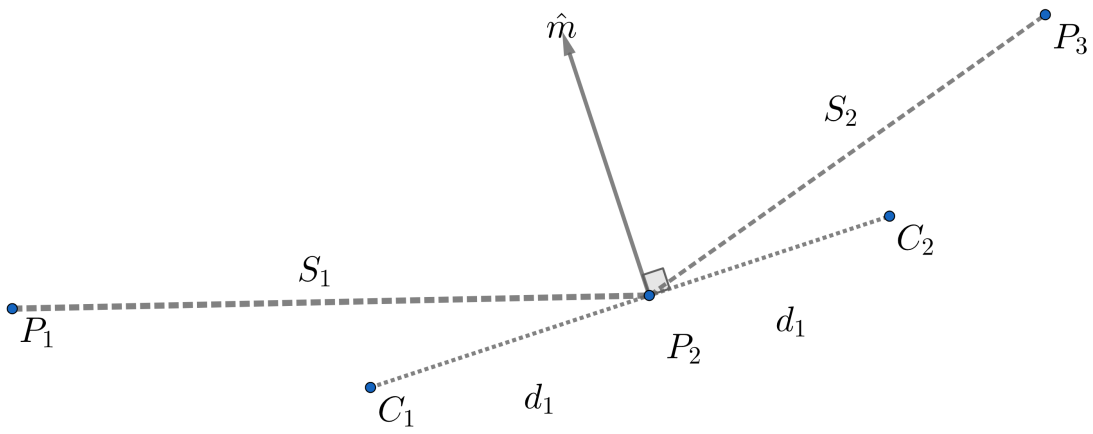

Figure A.1. Diagram illustrating how control point for the Bezier curve are obtained from map points. Based on the algorithm from [60].

A cubic Bezier curve requires 4 control points where the first and the last control point are the start and the end point of the curve while the other two control points determine the shape of the curve. Thus, for each segment of the map between points P_1 and P_2 the first and the last control points are P_1 and P_2. The method for obtaining the intermediate control points is based on the process provided in [60] as shown in Fig. A.1. The control points are generated at every intersection of two sections whereby the angle bisector $\hat{m}$ of the convex angle of the intersection is firstly generated. The control points C_1 for the previous segment and C_2 for the next segment of the intersection are placed on the line perpendicular to $\hat{m}$ at distance d_1 as shown is Fig. A.1. The distance d_1 is calculated as follows,

$$d_1 = \frac{\min(S_1, S_2)}{3} \tag{A.1}$$

where S_1 and S_2 are the length of the segment before and after the intersection respectively. The first point on the first segment and the last point on the last segment are placed on the segment at a distance equal to one-third of the length of the segment.